Electrochemical Behavior of Lithium Cobalt Oxide in Aqueous Electrolytes

A Dissertation

Presented to
The Academic Faculty

By

Anirudh Ramanujapuram

In Partial Fulfillment
of the Requirements for the Degree
Doctor of Philosophy in the
School of Materials Science and Engineering

Georgia Institute of Technology
May, 2018

Electrochemical Behavior of Lithium Cobalt Oxide in Aqueous Electrolytes

Approved by:

Dr. Gleb Yushin, Advisor
School of Materials Science
and Engineering
Georgia Institute of Technology

Dr. Faisal Alamgir
School of Materials Science
and Engineering
Georgia Institute of Technology

Dr. Preet Singh
School of Materials Science
and Engineering
Georgia Institute of Technology

Dr. Marta Hatzell
School of Mechanical Engineering
Georgia Institute of Technology

Dr. Matthew McDowell
School of Mechanical Engineering
Georgia Institute of Technology

Date Approved: May 7, 2018

Dedicated to Sharadha, Mom and Dad

Acknowledgements

It took a whole half decade of my life to complete this PhD, and I believe the time was completely worth it. There was so much to learn and so many challenges to face, but the whole process was an enlightening experience. Several people have helped me sail through this endeavor: a PhD is never a one-man show. I'd like to thank all of them who aided me in successfully earning this degree.

First and most importantly my advisor, Prof. Gleb Yushin, who has been a constant source of encouragement and guidance through all my difficult times. I don't remember a meeting with him that didn't inspire me to work harder. He has always constantly nudged me to push my limits, both in terms of learnings newer analysis techniques and trying newer ideas that I wouldn't have thought possible. I appreciate all his inputs, they helped shape me as a better researcher and as a stronger individual. Gleb was also a constant source of support when I struggled through personal difficulties. He also provided me a lot of advice on career choices and matters outside academics that were important for me in making life choices.

My wife Sharadha, I cannot imagine completing my PhD without her constant support. She has sacrificed so much, both personally and professionally, so I could thrive and call myself a doctor someday. She moved countries, changed professions and took a step back so I can finish my degree. I wouldn't have been able to come this far without her.

My parents, my brother and sister-in law, who constantly egged me on when I felt I should just give up. They have been there to lend me an ear when I needed to cry and to cheer me on through all my struggles. Thank you, Mom Dad, Sunny and Meghi, you have been

a constant source of guidance and support all my life. I couldn't have done this without you.

Several people in my lab have been of immense help in shaping my ideas through the years at my PhD. I'd especially like to mention Daniel Gordon for all his help and support in my initial years of grad school. Thank you, Dan, for teaching me so much about electrochemistry and experiment planning. I'd also like to thank Dr. Naoki Nitta, Dr. Alexandre Magasinski, Dr. James Benson and Dr. Feixiang Wu for all their guidance on several projects and for helping me move forward whenever I faced difficult roadblocks. And of-course all my other lab mates – Enbo Zhao, Chenchen Hu, Dong Chan Lee, Dr. Kostiantyn Turcheniuk, Xinran Wang, Yiran Xiao, Billy Johnson, Zefei Sun, Wenbin Fu, Doyoub Kim, Ah-Yong Song, Qiao Huang and others – who made grad life so much fun and bearable.

I'd also like to thank my undergrads - Brian Ward, Emily Kaukol, Ramon Sosa, Keith Coffman and Daniel Urli – who have worked tirelessly with me through different years of my PhD degree. Their help was invaluable for setting up several experiments and testing different cells. I appreciate all their inputs and hard work.

Three people I'd like to especially mention are Dr. Luis Estevez, Mrs. Renuka Pai and Prof. Vinod Kallur. The have been my source of inspiration to pursue my PhD degree. In so many ways, they sparked in me, an interest in science that made me pursue this degree. In some way, I owe this degree to them.

My friends – Karthik, Manik, Sathe, Jinsi, Sihag, Murgu, Umesh, Prasoon, Harsha, GV, Harshath, Dan, Kostia, Sacha, Nox, Francesco, Sagarika, Elham, Arianna and Sniff – who

were there through all the hard times and all the good times. There are so many memories I shared with them that I will cherish all my life.

Finally, my group of friends back home – Addy, Teri, Suhas, Gri, Jha, Venki, Wind, DT, Tarun, Nikhil and all the HBH – you have all been an important part of my PhD without being there in person. I have always remembered cherished all the good times we shared. You guys always have my back and it's an awesome feeling knowing you guys are always there for me.

Table of Contents

List of Figures

List of Tables

List of Abbreviations

ALIB – Aqueous Lithium Ion Battery

C-rate – Charge rate

CE – Counter Electrode

CV – Cyclic Voltammetry

EIS – Electro-chemical Impedance Spectroscopy

LCO – Lithium Cobalt Oxide

LFP – Lithium Iron Phosphate

LIB – Lithium Ion Battery

LiCl – Lithium Chloride

$LiNO_3$ – Lithium Nitrate

Li_2SO_4 – Lithium Sulfate

PVDF – Polyvinylidene fluoride

RT – Room Temperature

SEI – Solid Electrolyte Interface

SEM – Scanning Electron Microscopy

TEM – Transmission Electron Microscopy

WE – Working Electrode

XPS – X-ray Photo-electron Spectroscopy

XRD – X-ray Diffraction

Abstract

Lithium-ion (Li-ion) batteries are the most popular energy devices for almost all electronics today. From cell-phones and laptops, to advanced uses in automotive and aircraft applications, lithium-ion batteries have slowly taken over the market. Unfortunately, today's lithium-ion batteries are also highly unsafe. They rely heavily on organic solvents for electrolytes in the battery. These organic solvents are inherently flammable in nature and have caused several fires reported in batteries over the past few years.

In this research, I aimed to investigate changes in the electrochemical behavior of electrodes if we replace flammable organic solvents with a safer alternative such as water. Water-based batteries may offer greatly improved safety and lower cost (from lower raw material cost to reduced manufacturing costs). In addition, water-based electrolytes may exhibit dramatically higher ionic mobility for Li ions and thus can be potentially used for faster charging batteries or batteries with thicker electrodes, which are easier and cheaper to construct.

Lithium cobalt oxide (LCO) has long been proven to be an excellent material for cathodes in conventional organic electrolytes. It has shown high volumetric capacity and good stability in non-aqueous environments of commercial Li-ion batteries. Unfortunately, the flammability of organic electrolytes in combination with a propensity for batteries constructed with LCO to experience thermal runaway creates safety concerns. Due to extensive knowledge accumulated on LCO and its structural similarity with many other common cathode materials, LCO may serve as a model material for studying electrochemical interactions of layered lithium transition metal oxides with aqueous

electrolytes. While LCO had previously been demonstrated to cycle for 20-100 times in aqueous environments, the causes of its degradation had not been investigated in detail. Our studies demonstrated that in certain aqueous electrolytes LCO cathodes could cycle with a remarkable stability showing only 13% fading after over 1,500 cycles. Post mortem analysis of the electrodes was conducted to understand the effect of cycling and the causes of degradation. Electrolyte composition was found to have a dramatic impact on the electrochemical performance and stability of LCO in aqueous environments.

The temperature range for aqueous electrolytes at sub-zero temperatures was also investigated in detail. We showed that Li-ion batteries with aqueous electrolytes can be excellent candidates for battery applications at low temperatures. In contrast to a common misconception, aqueous Li-ion batteries can operate at several tens of degrees below the freezing point of water when high concentration electrolyte solutions are utilized. By leveraging the colligative properties of water, I demonstrated that aqueous electrolytes can function much below the freezing point of water down to -40^{o}C. The performance of water-based electrolyte systems with three low-cost inorganic salts ($LiNO_3$, Li_2SO_4, and LiCl) was extensively studied to understand the rate-limiting step in battery performance at sub-zero temperatures. It was found that the charge transfer resistance is the largest contributor to impedance at low temperatures, until the complete solidification of the aqueous electrolytes takes place. In sharp contrast, it was found that common organic electrolytes do not support any cycling below -20^{o}C. The contributions from the various resistances that affect low temperature cycling from the perspective of the electrode as well as the electrolyte were investigated in detail.

Chapter 1: Introduction

1.1. Introduction to lithium-ion batteries

Lithium-ion (Li-ion) batteries (LIBs) have become an indispensable part of our lives today. They power most of the portable electronic devices we use. And this rapidly growing industry is estimated to have a projected growth to a $50 billion market by 2020, per several sources[1,2]. The main reason for the popularity of the Li-ion technology is the high energy density and low weight of these batteries. These batteries thus take up less space, weigh less and can deliver high power that make them so attractive for these applications[1]. Li, being the lightest metal, packs in more energy per unit mass than any other element, thereby providing the highest energy per unit mass for a battery technology. LIBs work through what is known as the rocking-chair mechanism. Li ions travel back and forth between the electrode during the charging and discharging processes as shown in the Figure 1 below.

Typically, LIBs use a transition metal cathode such as lithium cobalt oxide (LCO), lithium manganese oxide (LMO), lithium iron phosphate (LFP), Titanium sulfide (TiS_2)[3–6]. Graphite is the most commonly used anode material[7,8] although, sometimes transition metal oxides and sulfides anode such as titanium dioxide (TiO_2)[9], lithium titanate ($Li_4Ti_5O_{12}$)[7] and molybdenum sulfide (Mo_6S_8)[8] have also been used. These metal oxides and ceramics act as host structures that can accept a Li-ion from solution. During charging or discharging, the Li-ions shuttles back and forth between the cathode and anode and alternately intercalate/de-intercalate from the host material.

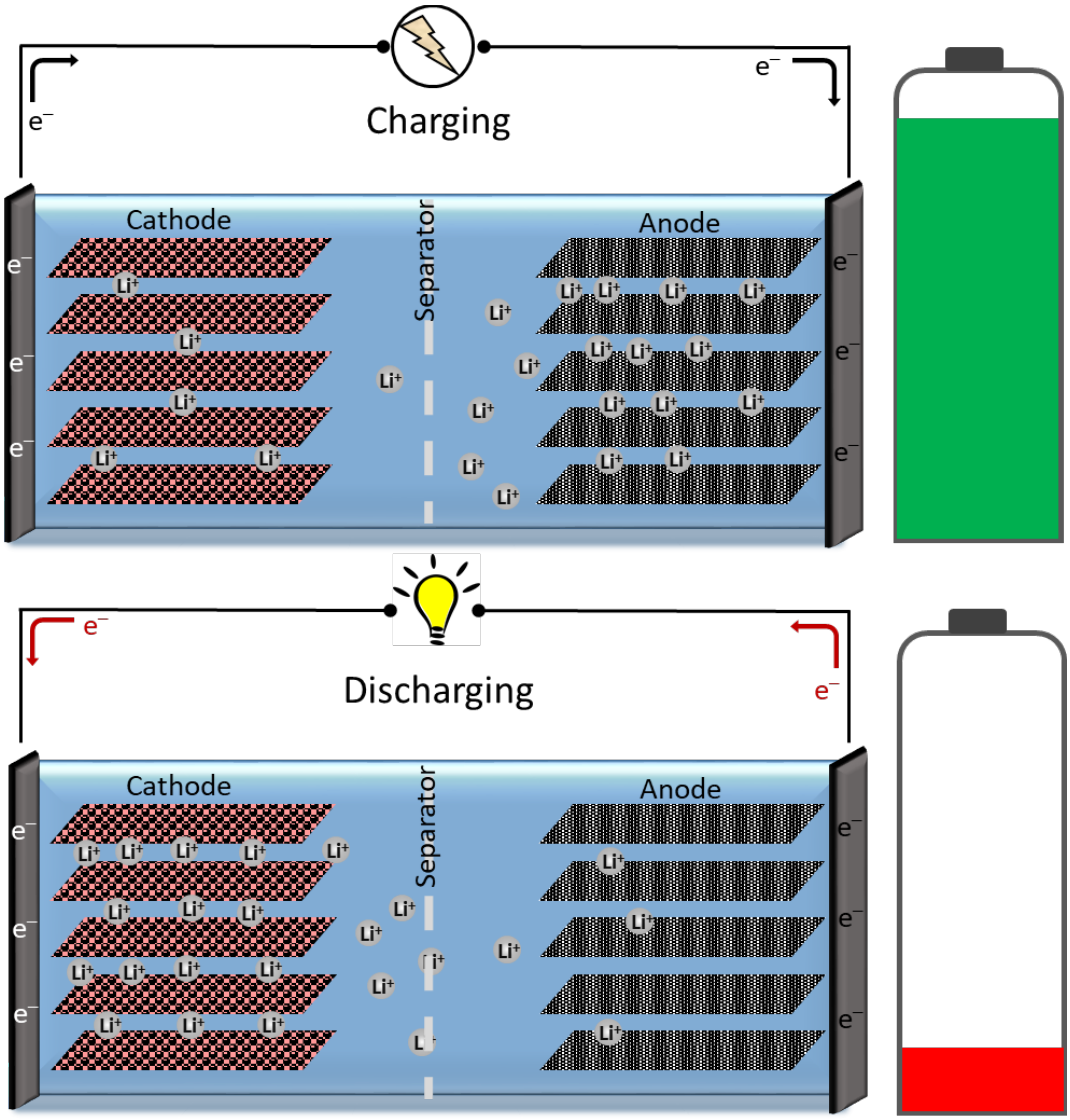

Figure 1: Schematic of the working of a typical lithium-ion battery

The electrolyte acts as an ionic conductor and an electronic insulator. It helps transport the lithium ions from one electrode to the other during cycling. The electrolyte in today's batteries is typically an organic solvent (or a mixture of organic solvents) with a lithium salt dissolved. Typical electrolyte solvents used are a combination of organic carbonates such as ethylene and propylene carbonates. Electrolyte salts can include $LiPF_6$, $LiClO_4$, LiTFSI

and several others. The salts along with the electrolyte solvents are typically chosen to create a stable solid electrolyte interphase on the surface.

Minor decomposition of organic electrolytes at the surfaces of anodes and cathodes typically leads to the formation of stable solid surface layers known as solid–electrolyte interphases (SEIs)[10]. The SEI plays an important role in improving its stability. It typically forms on the surface of the anode material as a decomposition product of the electrolyte and electrolyte salt. This decomposition results in the formation of an ionically conductive layer that helps stabilize the performance and improve the long-term cycling of the cell.

To date, non-aqueous electrolytes have been the electrolytes of choice for LIBs[11] because of their high stability and a large potential range, which enables LIB operation at voltages of up to around 4.4 V. These solvents, however, are inherently flammable in nature and are the main cause of fires reported in LIBs over the past few years. Added to that, some cathode materials such as LCO have a propensity to decompose in an exothermic reaction that releases oxygen. In combination with the highly flammable organic electrolytes, non-aqueous batteries thus create a significant safety risk[12].

As a result, safety measures often require overbuilding battery management systems (battery packs) with inactive materials, which increase the weight, volume and cost of the energy storage by up to 75% in the case of cell applications in large battery packs, such as electric vehicles[13]. Considering this, LIBs with water-based electrolytes provide a safer alternative. These batteries function like the conventional LIB but have much better safety characteristics.

In this thesis, we aim to investigate changes in the electrochemical behavior of common LIB electrodes (as well as the key mechanisms responsible for such changes) upon replacement of the organic solvents in contemporary batteries with water-based electrolytes. There are several advantages to using water as the electrolyte in LIBs. These batteries may become safer and more environmentally friendly and may cost less. Cost advantages arise from reduced raw material costs as well as reduced manufacturing costs since aqueous batteries can be manufactured in open air (vs. special dry rooms that need to be created for non-aqueous electrolyte batteries).

Water-based electrolytes commonly exhibit dramatically higher ionic conductivities for Li^+ ions (~10^2-10^3 mS/cm for aqueous vs. 10-14 mS/cm for organic electrolytes)[14–16] thus enabling the construction of batteries that can be charged faster or enabling the use of thicker electrodes. These properties make them ideal for several technologies such as in electric vehicles and grid-storage systems.

At the same time, there are also several challenges to using aqueous electrolytes in LIBs. In comparison to organic electrolytes that are stable at high voltages, water electrolyzes at a much lower potential difference, with a thermodynamically stable window of approximately 1.23 V when not considering the impact of a dissolved salt. Thus, it was believed that constructing a LIB with an aqueous electrolyte should require choosing a cathode and an anode of only moderately high and low electrode potentials, respectively, limiting the battery to a lower voltage (and thus lower energy density).

It was not until the mid-1990s that W. Li et al. published one of the first papers on LIBs in aqueous electrolytes[17]. Although the battery operated at a relatively low voltage of approximately 1.5 V (average) and showed a moderate cycle life (lasting approximately

25 cycles), their important research proved that it was possible to make secondary LIBs with aqueous electrolyte solutions.

In order to improve safety, environmental friendliness, and rate capability of LIBs, a renewed interest in gaining better understanding of the behavior of LIB materials in aqueous electrolytes has recently emerged[18–20]. Several methodologies may be utilized for increasing cell voltage, such as exploring over-potentials for oxygen evolution on the cathode and hydrogen evolution on the anode, utilizing a combination of solid and aqueous electrolytes[21], and, as most recently shown, forming an SEI[22–25]. A variety of commercial cathode materials used in today's commercial LIBs ($LiFePO_4$ (LFP), LCO, $LiNi_xCo_yMn_zO_2$ (NMC), $LiMnO_2$ (LMO), *etc.*) have been preliminarily studied in combination with aqueous electrolytes[26–28]. However, in contact with aqueous electrolytes, such materials typically exhibit poor electrochemical performance and short cycle life. While a detailed understanding of the electrode and aqueous LIB (ALIB) cell degradation phenomena is still mostly lacking, several factors have recently been proposed to impact cell stability, such as electrolyte pH and dissolved oxygen content[29], dissolution of the active material, intercalation of H^+ ions into the active material alongside Li^+ ions, and reactions between the active material and dissolved O_2 and H_2O[20].

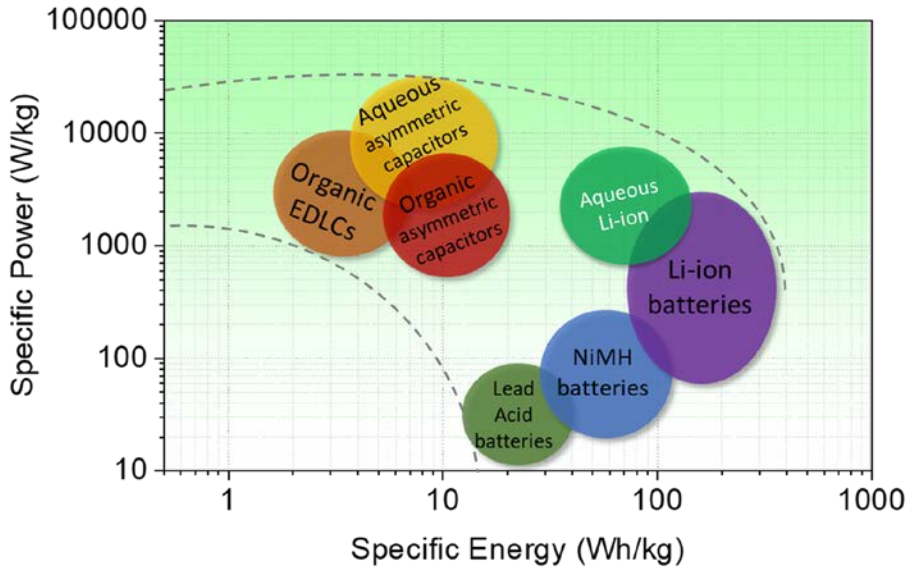

Figure 2: Ragone plot comparing the approximate energy and power density of aqueous LIBs compared to other energy storage technologies[30] (Reprinted from WIREs Energy Environ. 2014, 3, 424-473, Wentian Gu and Gleb Yushin, 'Review of nanostructured carbon materials for electrochemical capacitor applications: advantages and limitations of activated carbon, carbide-derived carbon, zeolite-templated carbon, carbon aerogels, carbon nanotubes, onion-like carbon, and graphene', with permission from John Wiley and Sons)

Figure 2 shows a typical Ragone plot for different battery systems that are used today or are being researched upon. Based on the inherently high ionic conductivity of aqueous electrolytes and the lower potential that can be sustained by this system, it could be predicted that ALIBs would deliver higher power densities yet lower energy densities than organic LIBs as delineated in the graph above.

1.2. Theoretical background

ALIBs may offer several advantages over LIBs based on conventional organic electrolytes. Aqueous electrolytes are non-flammable, safe, and inexpensive compared to organic electrolytes. ALIBs also allow for open-air manufacturing and are more environmentally friendly.

Despite all these inherent advantages, aqueous batteries have several shortcomings that need to be overcome for larger scale adoption. One of the key limitations is the lower electrochemical stability window for water. Thermodynamically, water decomposes at about 1.23 V, which is much narrower than the large voltage of operation of 3.7-4.2 V of non-aqueous LIBs.

This issue of thermodynamic stability can be illustrated with a simple molecular orbital diagram as shown below (adapted from Park. et al.[31]). Figure 3 shows the HOMO and LUMO for water as well as the cathode and anode materials for a LIB.

Let us consider a typical LIB anode, such as lithiated graphite (which is a graphite anode in a charged state). In this case, the electrons would flow from the graphite to the OH^- ions rather than to the cathode, thereby causing an explosive reaction. There would thus be the formation of hydrogen gas and LiOH.

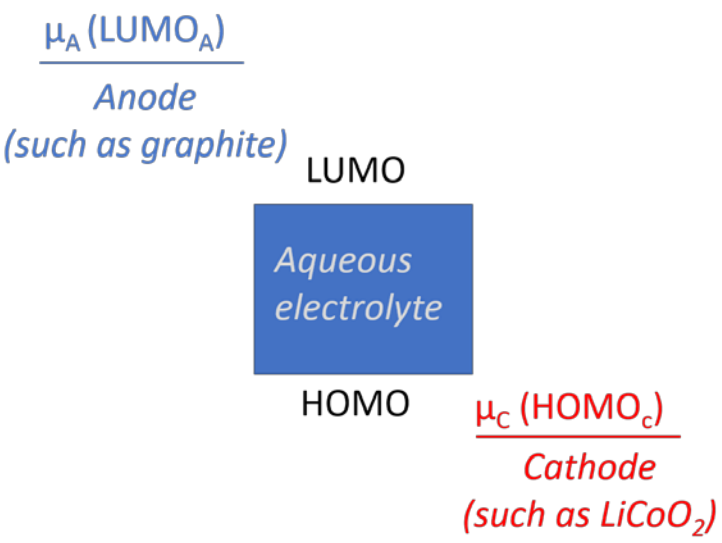

Figure 3: HUMO and LUMO depiction of an aqueous system when paired with traditional lithium-ion electrode materials

From a more practical standpoint of an ALIB, electrode materials are chosen so they are within or just outside of the stability window of water. In the simple cases, these would be $LiFePO_4$[13,32], $LiCoO_2$[23,33–35] and $LiMn_2O_4$ cathodes[28,36] and vanadium oxides (VO_x) [17,37,38]titanium phosphates ($LiTi_2[PO_4]_3$)[39–41] and TiP_2O_7[42,43], etc. Typical electrode materials used in aqueous electrolytes are shown in Figure 4 below.

As can be seen from Figure 4, some of these materials can work since they do not necessarily react with or cause water to decompose. However, in order for aqueous electrolytes to compete with organic electrolytes in terms of energy density, it is important that the stability of these electrolytes is expanded to well beyond 1.23 V.

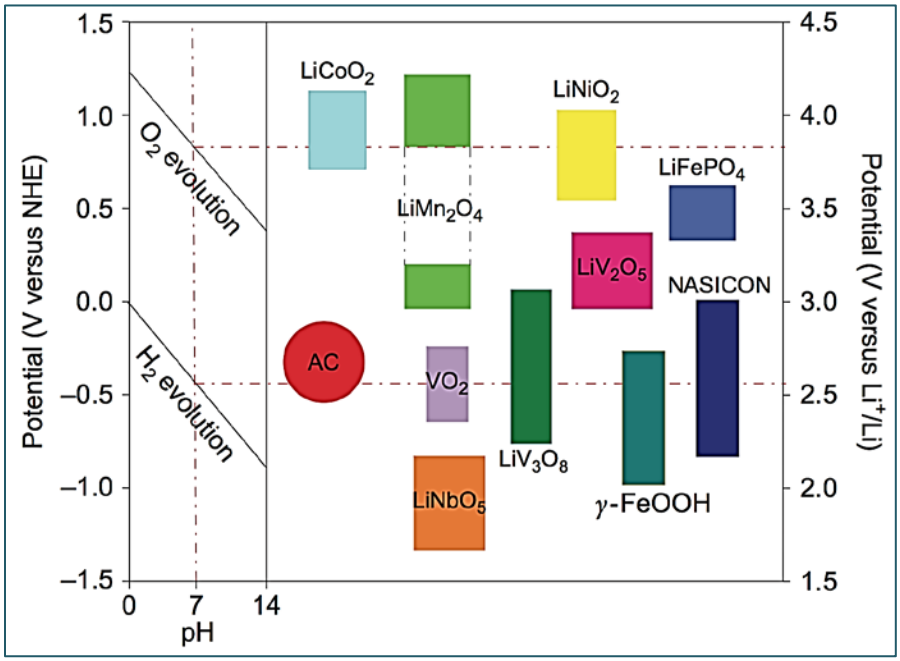

Figure 4: Typical lithium-ion cathode and anode materials that are compatible with aqueous electrolytes from the standpoint of water stability. The stability window for water (Pourbaix diagram) is also incorporated in the left side of the figure[29] (Reproduced with permission from Springer Nature)

Several aqueous battery technologies in the past have successfully operated at significantly higher voltages than what is thermodynamically feasible. The mercury oxide battery operates at 1.35 V[44], the alkaline cell operates at 1.5 V[45] and the lead acid battery (car battery) at 2.1 V[46,47] This phenomenon can be explained using the concept of overpotential. Overpotential is defined as the minimum polarization at which a particular reaction occurs at an appreciable rate on a specified electrode, or at which, with a small increase in voltage, there is a marked increase in current density[48]. It explains the difference between the thermodynamic and the actual potential of a reaction.

Aqueous electrolytes can be promising candidates for safer and lower cost lithium-ion batteries. However, the narrow electrochemical stability window for water is a large limiting factor for high energy density batteries. Thermodynamically, water decomposes at 1.23 V to form hydrogen and oxygen. The exact potential for the cathodic and anodic reactions is then pH dependent as is dictated by the Nernst equation:

$$E_{rxn} = E^{o} - \frac{RT}{zF} \ln \left[\frac{conc.\,of\ reactants}{conc.\,of\ products} \right]$$

where, E_{rxn} = thermodynamic potential of the reaction,

E^{o} = thermodynamic potential of reaction under standard conditions (Room temperature with an activity of 1 for the reacting species),

R = universal gas constant,

T = temperature in K,

z = no. of electrons involved in the reaction,

F = Faraday's constant

Thus, by varying the pH of the solution, the hydrogen and oxygen evolution potentials can be shifted around, although the overall potential window would be the same. Hence the thermodynamic potentials for H_2 and O_2 evolution would be 0.0 V and 1.23 V at pH = 0, but it would shift to -0.41 V and +0.82 V at a pH of 7.

But there are several other factors that influence the kinetics of this reaction such as the surface energy of the electrode surface, the adsorption coefficient, etc. These kinetic

factors can have an enormous influence on the overall potential of the reaction and can thus be used to expand the overall stability window for water.

The kinetics of an electrochemical reaction is determined by the Bulter-Volmer equation:

$$i = i_o \left[exp\left(\frac{\alpha_a zF}{RT}(E - E_{eq}\right) - exp\left(\frac{\alpha_c zF}{RT}(E - E_{eq}\right)\right]$$

where, i = electrode current density (A/m^2),

i_o = exchange current density (A/m^2),

E = electrode potential,

E_{eq} = equilibrium potential or thermodynamic potential (defined above as E_{rxn}),

α_a and α_c = anodic and cathodic charge transfer coefficients.

The term E - E_{eq}, sometimes denoted by η, is called the overpotential of the reaction. It defines the deviation of the potential from the equilibrium or thermodynamic potential of the reaction. The overpotential is mainly a kinetic phenomenon and is vastly influenced by the electrode surface and other kinetic factors. Chief contributors to the kinetics of the reaction are exchange current density and activation energy.

Several researchers in the past have used the concept of overpotential to create Lithium-ion battery systems that are higher than 1.23 V. The first paper on ALIBs appeared in 1995 when Dahn et al.[17] reported a rechargeable 1.5 V battery using $LiMn_2O_4$ and VO_2. Although this battery has low capacity and cycle life, it demonstrated that lithium-ion batteries can be cycled using water-based electrolytes.

Since then, several researchers have studied the performance of a variety of intercalation type materials in aqueous electrolytes[18,26,28]. In 2015, Liumin Suo et al.[22] used the highly concentrated water in salt electrolyte to demonstrate that the stability window for water can be expanded as high as 3 V using a saturated LiTFSI. Soon after, they demonstrated a 2.1 V battery using a highly concentrated water-in-bisalt electrolyte that contained 21m of LiTFSI and 7m of LiTOf in water[24]. Several groups have thereafter also shown that the use of concentrated electrolytes with LiTFSI allows for the formation of an SEI due to the creation of a new type of solvation shell where the water is encapsulated inside a sphere of the ions[23,25].

The cost of such an electrolyte system though is a large hurdle. These organic salts are very expensive and at such high concentrations they could become the largest cost to the overall battery assembly. This would automatically reduce the commercial viability of the aqueous system, taking away one of the main draws of low-cost for water-based systems.

Recently, a newer paper by Yang et al.[25] showed that it is possible to create a 4 V battery using an artificial SEI created using a polymer coating on the anode. This is the highest voltage demonstrated for an aqueous electrolyte. This concept was also used by Wang et al.[21] to make a coated Li-metal anode to demonstrate 1,000s of cycles of stable capacity for LMO in aqueous electrolytes.

Of course, the concept of an artificial SEI is a well understood phenomenon in aqueous systems. Several Li-air batteries in the past have shown that it is possible to cycle Li-metal in aqueous systems using a polymer coating with a glass ceramic coating[49–51]. These systems show that several low voltage materials (that would normally react vigorously with water) can be cycled in aqueous systems using an artificial SEI.

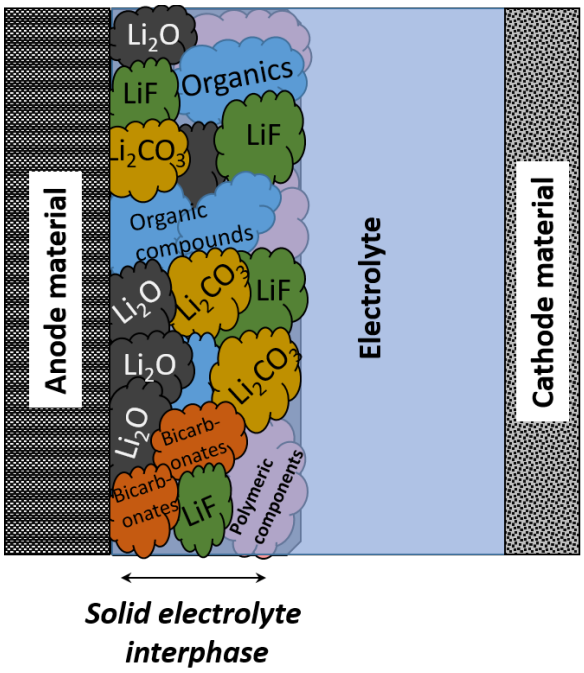

Figure 5: Schematic of an SEI showing the various components that could be present. A good SEI should provide high ionic conductivity and also high electronic resistance

An SEI is defined as a protective layer formed on the negative electrode material of the battery. Its formation is linked to the decomposition of the electrolyte on the electrode surface during the charging process[52–54]. It is typically an electrically insulating and ionically conductive material. In the case of LIBs (with both organic and aqueous electrolytes), these coatings allow Li-ions to diffuse through them. But since they are electrically insulating, such interfaces cause a potential drop in the material that prevents the electrolyte from decomposing further[55]. A schematic of a typical SEI is shown in Figure 5.

Thus, by creating an ionically conductive and electronically insulating layer, it would be possible to create an aqueous system with much higher voltages than the stability of water.

With increasing interest in the aqueous research from both the academic and industrial spheres (Aquion Energy was a start-up that aimed to commercialize an aqueous sodium ion battery and had received a total funding of $182.3M[56]), ALIBs are an interesting new technology that could rival organic batteries one day.

Aqueous electrolytes still come with their own set of challenges, on both the cathode and anode side of the battery. The largest challenge of course is that of overpotential discussed so far. But several others that have been overcome in organic electrolytes using additives still pose a strong challenge for water-based systems. A large problem to be addressed is corrosion of current collectors, especially at the positive terminal of the battery. Take for example, the case of $LiCoO_2$. Lithium cobalt oxide intercalates/de-intercalates Li^+ ions at 0.93 V vs. SHE in a 1M solution of Li^+ ions (pH=7). At such high potentials, most metals would corrode, oxidize or react with aqueous systems. This can be explained in terms of the Pourbaix diagram[57] as seen in Figure 6 below for aluminum (a common current collector for organic LIB cathodes).

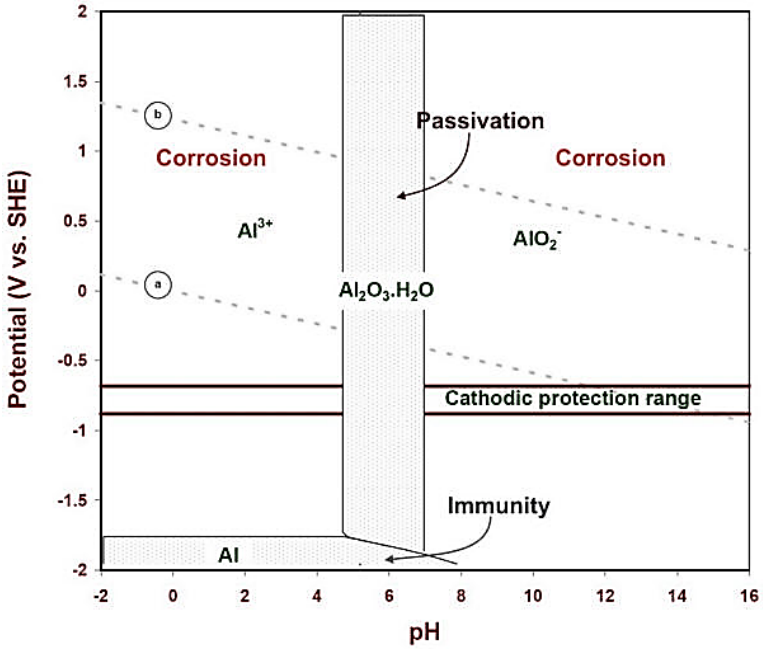

Figure 6: Pourbaix diagram for Al showing regions of corrosion and passivation[57]

Of course, corrosion should occur in organic solutions as well, but in most organic electrolytes this problem is overcome using fluorides in the electrolyte. At higher potentials, the Al current collector forms a passivating layer consisting of oxides and hydroxides on the surface of the current collector[58–61]. This passivating layer prevents the further dissolution of the metal allowing for stable performance of the cathode at high potentials.

Consider the linear sweep voltammetry (LSV) for three metals – aluminum (Al), stainless steel (SS) and titanium (Ti) in aqueous solution as shown in Figure 7 below (see Chapter 2 section on cyclic voltammetry for more information on linear sweep voltammetry). The LSV was conducted at 0.3 mVps in1M $LiNO_3$. A large corrosion current is seen in the case of SS and Al foils whereas there is only a capacitive charging current of micro-amps seen

in the case of the titanium metal. The passivating oxide layer formed on the Ti metal surface prevents further corrosion, which does not occur in the case of SS.

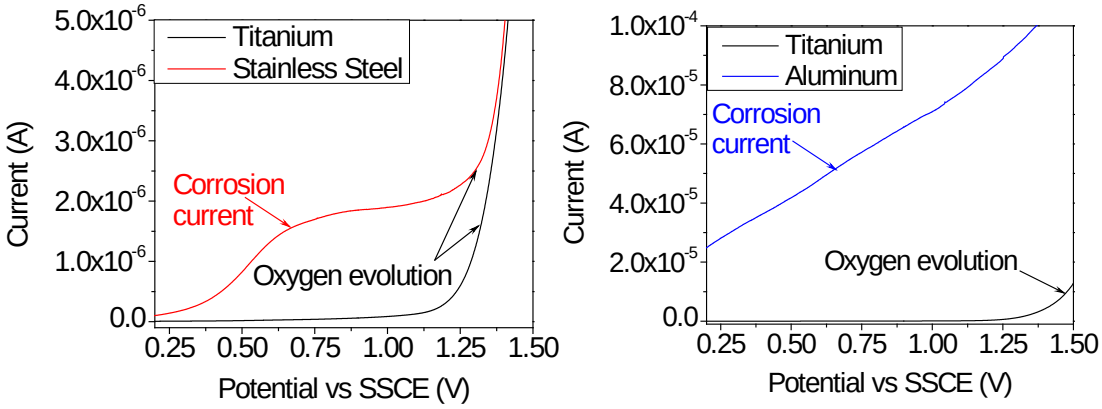

Figure 7: Comparisons of linear sweeps for different metals showing a large corrosion current for the current collectors in 1M $LiNO_3$. Titanium metal is resistant to this corrosion and only evolves oxygen at high potentials

The effects of corrosion of the current collector can pose a huge problem to the stability of the cathode performance in aqueous batteries. This is clearly illustrated in the cycling behavior of lithium-cobalt oxide cycled in 1M $LiNO_3$ as shown in Figure 8 below.

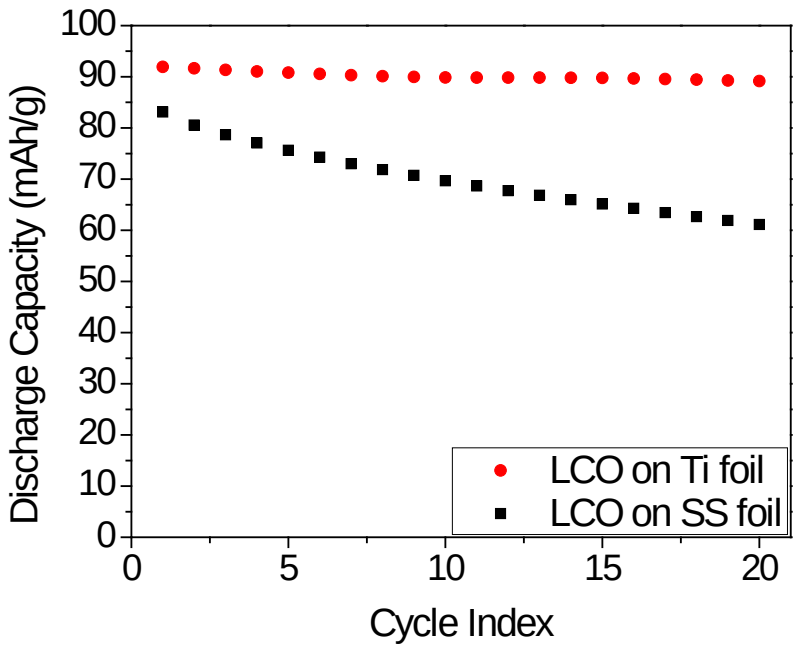

Figure 8: Discharge Capacity for lithium cobalt oxide cast on SS and Ti current collectors. The corrosion of the SS causes a large drop in capacity over even as small as 20 cycles

The figure above shows the performance of LCO (a relatively high voltage cathode material) cast on stainless steel (SS) and titanium (Ti) foils cycled at 1C-rate in 1M $LiNO_3$. Performance of LCO on Al current collectors is not shown since Al-metal corrodes and dissolves completely in water before any capacity can be achieved. In the case of the SS foil, there is some capacity seen initially. But there is a large drop in performance even over the first few cycles. The SS undergoes corrosion current creating a resistive layer of $Fe_xO_y.nH_2O$ (rust) on the metal (current collector turns brown after cycling). This causes an electric short circuit of the cathode material from the current collector that leads to a loss of performance in the LCO (the electrode peels off completely from the metal foil). In our initial experiments, we attributed this bad performance to the LCO material itself.

However, upon changing the current collector to Ti metal, a dramatic improvement in performance is seen. Ti metal, interestingly, forms a passivating layer of titanium dioxide on its surface. This thin layer allows for electron conduction to the cathode but prevents further corrosion of the current collector.

The challenges with the negative terminal of the battery are vastly different. At lower potentials, the metallic current collector is mostly stable, but hydrogen evolution becomes a very strong challenge. The hydrogen or hydronium ions in water have a very high exchange current density on most surfaces. This makes it harder to control hydrogen evolution and hence reduces the overall voltage of the battery.

Metal	I_o ***(A/cm^2)***
Pb, Hg	10^{-13}
Zn	10^{-11}
Sn, Al	10^{-10}
Ti	10^{-9}
Ni, Ag, Cu	10^{-7}
Fe, Au	10^{-6}
Pd, Rh	10^{-4}
Pt	10^{-2}

Table 1: Exchange current density for hydrogen on different metal surfaces (adapted from NPTEL[62] J.O'M.Bockris et al.[63] and J. K. Nørskov et al.[64]

As can be seen in the Table 1, most metals have a high exchange current density of H_2 implying hydrogen evolution occurs rapidly at potentials below the equilibrium value. At the same time, overpotential is also a feature of surface area. The larger the surface area, the larger the overall current generated. Consider the simple case of hydrogen evolution

on titanium metal cut to three different surface areas as shown in Figure 9 below. Three different flags of titanium were cut out with areas of 1 cm^2, 9 cm^2, and 25 cm^2. A linear sweep was run on these flags to lower potentials to observe the potential at which hydrogen evolution occurs. As can be seen from the graphs, at the same current (take for example, 300 μA), the overpotential seems larger in the case of the 1 cm^2 flag than for a 25 cm^2 flag. Since the H_2 evolution is considered a side/undesired reaction for Lithium ion batteries, larger surface areas for the electrode contributes to higher currents from the H_2 evolution which in turn could reduce the Coulombic efficiency for the anode. This could become a larger issue while dealing with materials with high surface area such as the carbon additive in electrodes. Carbon in the form of pure black or conductive carbon black is added to most electrodes to improve their conductivity. Their surface area is typically around 80-100 m^2/g. So the addition of carbon could increase the surface area and cause larger evolution of hydrogen on electrode surfaces other than the active material. This also adds a level of complexity to aqueous systems in terms of preventive side reactions.

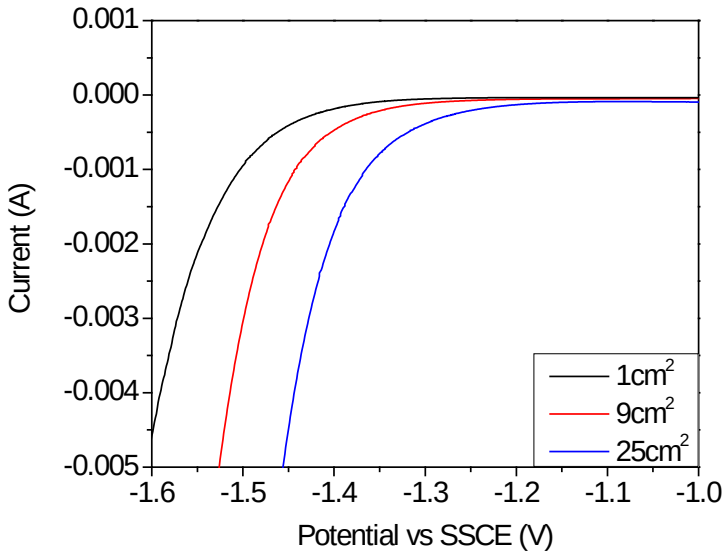

Figure 9: Hydrogen evolution on plain titanium metal cut to various sizes for different surface areas in contact with the electrolyte

Lastly, there are the challenges of electrode material dissolution. Several materials that can conventionally be used with organic electrolytes cannot be used in the case of aqueous electrolytes, even though their electrochemical potential of operation is well within the range of water stability. A classic example would be the sulfur system. Sulfur can have a reaction potential in the range of -0.6 to -1.0 V vs. SHE[65] (depending on the polysulfide formed). This could be well with the range of overpotential for hydrogen evolution in certain electrolytes.

Although sulfur by itself is insoluble in water, upon reacting with Li-ions, it forms soluble polysulfides and ultimately Li_2S which dissolves and reacts with water. This was very clearly seen in our initial few experiments where there was the evolution of H_2S gas and the electrode dissolved over time into the electrolyte (although the sulfur by itself did not).

Despite these challenges, there are several materials that can successfully be cycled in aqueous electrolytes. There is increasing interest in this field from both academia and industry, to make aqueous chemistry a strong contender for the conventional Li-ion battery. In this thesis, we will delve into the performance of lithium cobalt oxide, a traditional cathode material used in batteries for portable electronics. The causes of degradation of LCO in aqueous environments will be investigated.

Another important consideration for any battery is its performance at different temperatures, especially at sub-zero levels. When considering an aqueous system, it is usually assumed that water-based electrolytes would freeze at temperatures below 0^{o}C. But several applications could require batteries to function in colder conditions[66,67]. Several researchers in the past have extensively studied the performance of organic LIBs at temperatures of -10^{o}C to -40^{o}C[68–76]. These papers usually report the discharge capacities for cells and show that organic LIBs can retain about 12% of their room temperature capacity down to -40^{o}C. But no similar study has been conducted on aqueous electrolytes to understand their performance at lower temperatures.

It is well known that using the colligative properties of solutions[77–79], it is possible to depress the freezing point of dilute aqueous solutions to a few degrees below 0^{o}C. Expanding on this principle, it should then be possible to decrease the freezing point of water to several tens of degrees when concentrated salt solutions are used. This should allow aqueous electrolytes to perform in very cold conditions that could rival the performance of organic electrolytes. This effect and the consequent performance of aqueous electrolytes at sub-zero levels has also been extensively investigated in this thesis.

Chapter 2: Characterization

2.1. Introduction

The characterization techniques used can be categorized into two main methods based on the property of the material studied:

1. Electrochemical techniques
2. Materials characterization techniques

Materials characterization can be further classified into surface characterization techniques such as X-ray Photo-electron Spectroscopy, Transmission Electron Microscopy and Scanning Electron Microscopy and bulk characterization techniques such as X-Ray Diffraction, Fourier Transform Infrared Spectroscopy among others. In this section, we will look at these individual techniques in greater detail and establish the main principle of operation and understand the kind of data the technique provides.

2.2. Electrochemical characterization

Electrochemical characterization, in a very broad sense, is used to understand the current and voltage responses of an electrode material. Using a combination of different direct and alternating currents and voltages, one can understand the thermodynamics and kinetics of an electrochemical system and the key properties of that material in a given environment. The main techniques covered in this section include cyclic voltammetry, linear sweep voltammetry, constant current experiments along with differential capacity analysis, and electrochemical impedance spectroscopy.

2.2.1. Cyclic Voltammetry

Cyclic Voltammetry or CV as it is popularly known, is an electrochemical technique used to understand the thermodynamic potential and kinetics of an electrochemical reaction[80–83]. It is one of the fundamental techniques used by the electrochemist to study the current response to an applied potential; and hence the performance characteristics of an electrode/ electrolyte. It is considered a potentio-dynamic technique, where the electrode is scanned at the desired scan rate (usually denoted in millivolts per second or mVps) back and forth between two potentials (known as the switching potentials). The current response to this change in potential is recorded and plotted to reveal the peaks that contain useful information about the reaction rates and potentials.

In a typical CV experiment, three electrodes are used: a working electrode (WE), a counter electrode (CE) and a reference electrode (RE). The working electrode is usually comprised of the active material along with some additives. It is the main electrode under study, whose current response is being investigated. This working electrode is paired against a reference electrode, which ideally, is an electrode whose potential does not change throughout the CV scan. This electrode typically has a high impedance so that minimal current flows through it as the experiment progresses. Finally, the counter electrode is used as a current sink, to receive the charges and ions from the working electrode and complete the electrical circuit. A schematic for a CV setup is shown in Figure 10 below.

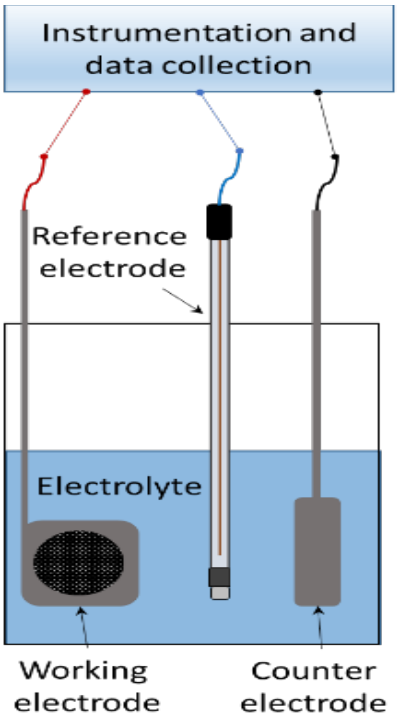

Figure 10: Schematic of a typical three electrode setup for cyclic voltammetry

In such an experiment, the voltage is measured between the working electrode and the reference electrode whereas the current response is recoded between the working and counter electrodes.

A typical CV is shown in Figure 11. Figure 11(a) shows the change in the potential applied and the implied scan rate for the experiment. Figure 11(b) shows the current response to that applied potential. Two main peaks A & B are seen in this scan, which correspond to the oxidation and reduction potentials for the electro-active material in the working electrode. In this specific case, it corresponds to the de-intercalation/removal of Li-ions (peak A) and the intercalation/insertion of Li-ions (peak B) into LCO[34]. The potential

(voltage) measured is versus a standard silver/silver chloride electrode (which maintains a fixed potential of 0.22 V throughout the experiment).

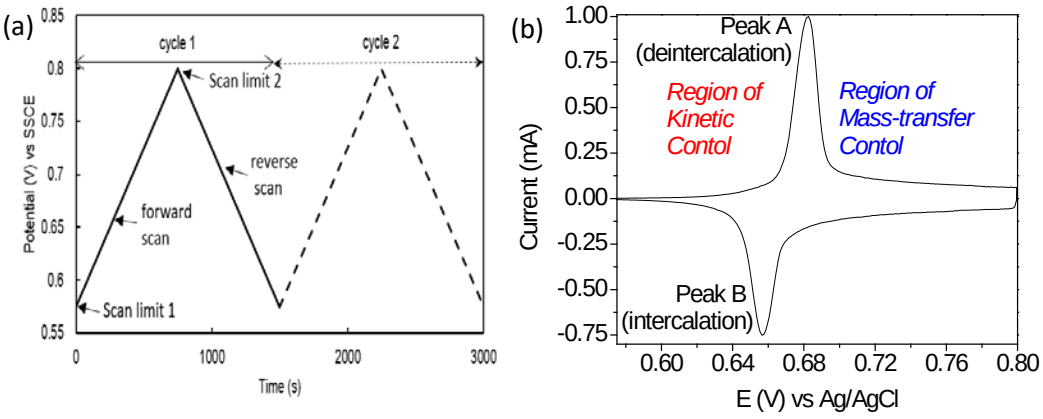

Figure 11: (a) Typical triangular excitation signal for cyclic voltammetry with switching potential at 575 mV and 800 mV vs. SSCE (adapted from Kissinger et al.[80]), (b) a cyclic voltammogram shown for LCO in an aqueous solution of sat Li_2SO_4, depicting the different regions of kinetic and mass-control.

There are two main regions in a CV. These are termed the region of kinetic control and the region of mass control. Kinetic control of the reaction occurs where there are enough ions around the electrode (in the Helmholtz layer) to allow for the reaction to occur. Analysis of this region can provide information about the rate of the reaction and the diffusion coefficient of the electrode species. As the scan proceeds in the forward direction, the increasing voltage (or decreasing for the reverse scan) provides a higher driving force for the reaction, which increases the magnitude of current till it peaks at a maximum.

As the reaction progresses, more ions in the electrolyte are consumed so that their availability in the vicinity of the electrode decreases. Ions would now have to travel from the bulk of the electrolyte to the double layer region before they can react at the electrode. This region (which corresponds to the decrease in the current after the peak in the CV graph above) is termed the region of mass control and can be used to calculate the diffusion coefficient of ions in the electrolyte. Depending on whether diffusion through the electrode particles or diffusion through the electrolyte is slower, the reaction would be termed kinetically controlled or mass transfer controlled.

The most important information gleaned from a CV is the thermodynamic potential of the reaction. Typically for a reversible reaction, the average potential between the oxidation and reduction processes is considered the thermodynamic potential of the reaction. An important aspect is the reversibility of the process. A reaction can be completely reversible, pseudo-reversible or irreversible depending on whether the opposite peak (here, Peak B) exists, has the same area as the forward peak, or is completely non-existent [for more information refer to Bard and Faulkner[84], p. 226-259].

A CV also provides a lot of information about the kinetics of that electrochemical process. By analyzing the shape of the curve, the skewness, full width half maximum (FWHM), etc., it is possible to avail several parameters about the process such as the diffusion constant, beta coefficient, etc. The separation between the peaks accounts for the polarization in the reaction, which could relate to the particle size of material in the electrode, the impedance in the electrolyte, etc.

A subset of cyclic voltammetry is linear sweep voltammetry (LSV). In a typical LSV, the dynamic voltage scan is conducted only in a single direction without a reverse sweep. This

allows the researcher to glean data on a single (mostly irreversible) reaction in one direction. It is mainly used to study adsorption of species onto materials[85–87], corrosion of metals[88–91] and other irreversible reactions[92].

2.2.2. Electrochemical Impedance Spectroscopy

Electrochemical Impedance Spectroscopy (EIS), also called Impedance Spectroscopy is an electrical technique used to study and understand the impedance response of the system to a variable frequency a.c. current. The impedance thus measured can give us quantitative values of the various resistors and capacitors that make up the electrochemical cell[93–96].

In a typical EIS measurement for a cell, a small a.c. potential (with a typical rms value 2-100mV) is applied at varying frequencies (typically between 0.1Hz to 10MHz). At each frequency, the impedance response is measured by taking the ratio of the voltage to current.

$$Z = \frac{V\ sin(\omega t)}{I\ \sin(\omega t + \varphi)}$$

where, V = applied a.c. potential

I = current response to the applied potential

ω = radial frequency = 2πf

φ = phase shift for current response

This impedance data can be used in two ways:

1. The impedance (both real, imaginary and impedance modulus) or its theta values can be plotted as function of the applied frequency with Bode plots, OR
2. The value of imaginary impedance (Z_{Im}) can be plotted vs. its real value (Z_{Re}) to obtain a Nyquist plot.

Both types of plots can provide valuable information about the resistances and capacities that exist within the cell[97–99]. The Nyquist plots are used extensively in electrochemical research to understand changes in material properties as well as to study the formation of interfaces such as the SEI during cell cycling[100–104].

Let us consider the simplest case of an electrode dipped in an electrolyte. This interaction of the solid and liquid creates a Helmholtz double layer at their interface. This re-distribution of charges creates a capacitive element in the battery. Similarly, the electrode materials and electrolytes in the battery add resistance elements.

Three main impedance elements exist in this system - the resistance of the electrolyte, the capacitance at the electrode-electrolyte interface and the resistance of the electrode. In this case, the electrode resistance is considered to be in parallel with the double layer capacitance of the interface. The electrolyte resistance is in series with this parallel RC circuit as shown below in Figure 12. These elements show up at different frequencies on a Nyquist plot and can thus be calculated from the different sections of the graph.

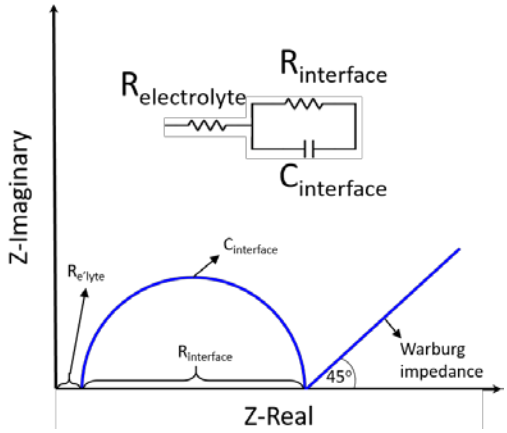

Figure 12: Typical Nyquist plot for a simple electrode-electrolyte interface

In this simplest case, the electrolyte resistance shows up as the X-intercept (or Z-real) on the curve at high frequencies. The RC element from the electrode and double layer show up as a semicircle at mid frequencies. The diameter of the semicircle measures the resistance of the electrode and the topmost point of the semicircle can be used to measure the capacitance (using the formula for a parallel RC time constant $\omega\tau=1$, where $\tau=RC$. The value of ω can be obtained from the Bode plots as the peak that appears in the Z_{Im} vs. log(f) plot).

The final part of the Nyquist curve is a straight line at 45°. This line corresponds to the Warburg impedance and is a measure of the diffusion of ions through the electrolyte[98,105]. The diffusion coefficient of the electrolyte can be measured from this line using the formula.

Electrodes can also get covered with a solid electrolyte interface during cycling, which also creates new capacitive and resistive elements in the cell. A battery can thus be said to consist of a series of capacitive and resistive elements whose impedance values are

given through EIS. EIS is thus an important technique used to understand the change in the resistances and capacitances in the material which can give us a more detailed picture of the different interfaces that exist in the electrochemical cell.

2.3. Materials characterization techniques

Surface characterization techniques typically examine the top 2-20nm of the material. They are strongly dependent on the depth of penetration of the incident interacting rays with the material and typically provide information only about the top few layers of atoms. Several techniques were used in this thesis including XPS, SEM and TEM. These techniques are especially important for battery research since most electrochemical processes occur at the surface or interface. Therefore, any changes that occur in the material would be most prominently be detected using these techniques as will be seen in the proceeding chapters.

2.3.1. X-ray Photo-electron Spectroscopy

X-ray Photo-electron Spectroscopy or XPS is a spectroscopic technique used to study the material composition as well as the precise oxidation state of the elements present in the material [106–110]. Also known as ESCA (Electron Spectroscopy for Chemical Analysis), it is a surface analysis technique that can typically provide information about the top 2-10nm of the sample[110,111].

XPS is concerned with estimating the binding energy (BE) of the core-electrons that are emitted when bombarded with a monochromatic X-ray beam. As the name suggests, the

technique uses an X-ray beam of sufficient energy to ionize the material and eject electrons from its core shells. The electrons that are “photo-emitted” are then analyzed for their exact energy and number to determine the species present in the material as well as their oxidation states.

The most fundamental concept to be understood in XPS is the Binding Energy. In the simplest sense, BE is the energy with which the nucleus holds on to an electron in a particular shell. Mathematically it is the difference between the energy of an electron in a particular shell and the energy of the Fermi level of that atom or ion.

In XPS, the energy of the incident photon is much higher than the binding energy of core-shell electrons. The excess energy of the photon provides kinetic energy to the ejected electron which is recorded at the detector. By analyzing this kinetic energy, the binding energy can be back calculated from the equation:

$$E_{hv} = E_{BE} + E_{\varphi} + E_{KE} \quad [1]$$

where, E_{hv} = Energy of the incident photon/ X-ray beam,

E_{BE} = Binding Energy,

E_{φ} = work function of the material,

E_{KE} = Kinetic Energy of the ejected electron

The work function of a material is the difference between the energy of the electron at the Fermi level and at vacuum (when it is completely free from the influence of the nucleus)[111]. These different energies are shown in Figure 13 below.

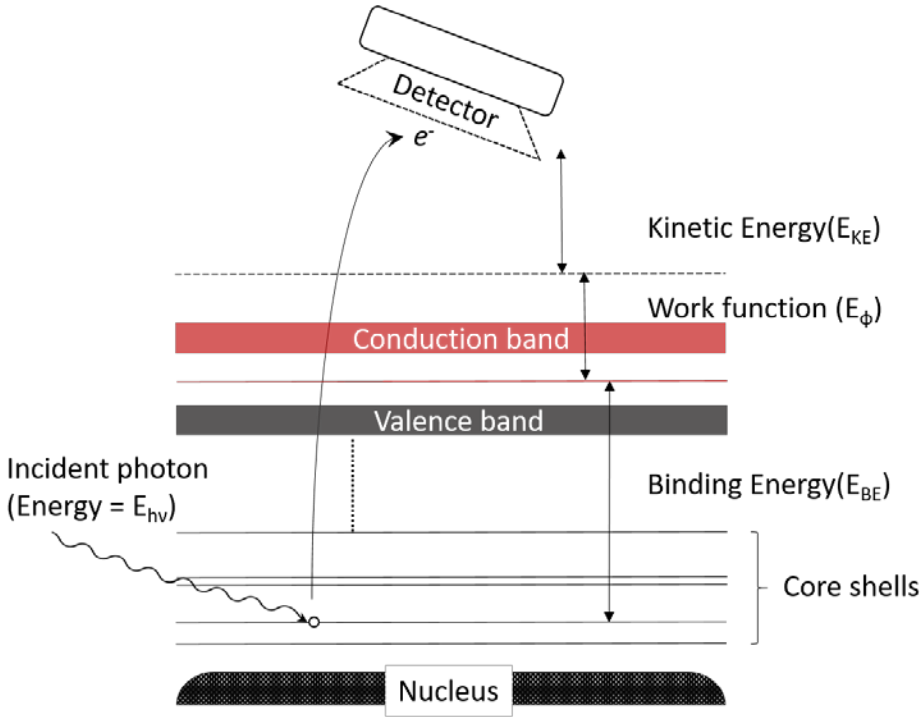

Figure 13: Schematic of XPS showing the different energies

The value of E_{φ} of the material is usually standardized or equated to that of the instrument and thus becomes a known constant for the material. The binding energy can then be easily calculated for the given material.

The binding energy value for an electron depends on upon several factors, such as the element and the orbital from which the electron is emitted. It also strongly depends on the chemical environment of the atom from which the electron was emitted. This implies that when the same atom has a different chemical state or is surrounded by different atoms, the binding energy for the electron in the same orbital would also slightly change. This phenomenon, known as the 'chemical shift', makes XPS a powerful technique in analyzing the changes in the material environment for a specific atom before and after any process.

Shifts as small as 0.05 eV could be detected if the X-ray source is of a single frequency and a highly sensitive detector is used.

By the same analogy, XPS is able to detect a change in the oxidation state of the material. An element in different oxidation states would have different binding energies for its core electrons that can be detected and analyzed using this technique.

Typically for XPS, an Al K-α or an Mg K-α X-ray source is used. These X-rays provide a photon energy of 1486.6 eV and 1253.6 eV respectively. The material, typically a solid, is placed under a very high vacuum of 10^{-7} to 10^{-9} torr. The material should be at least moderately conductive and electrically connected to the instrument so that the sample and the spectrometer have a similar Fermi level. Typically a hemi-spherical detector with a grid bias is used to selectively analyze electrons of a particular energy[112].

2.3.2. Scanning Electron Microscopy

Scanning Electron Microscopy or SEM is an imaging technique that utilizes an electron source to form images[113,114]. It is used extensively in materials science to obtain information about the surface and topography of materials down to 1 nm for well-prepared samples[115,116]. Scanning electron microscopes use the particle nature of electrons to provide high resolution images. The resolution of an image can be expressed by the Abbe's equation[117] given below

$$d = \frac{0.612 * \lambda}{n \sin \alpha}$$

where, d = resolution of the image

λ = wavelength of imaging radiation

n = index of refraction of medium between point source and lens, relative to free space

α = half the angle of the cone of light from specimen plane accepted by the objective (half aperture angle in radians. $n*\sin\alpha$ is also referred to as the numerical aperture)

Thus, by reducing the wavelength/ increasing the frequency of the wave, it is possible to increase the resolution. In a typical SEM, the electrons emitted from an electron gun are accelerated through electric fields to high energies. These high energy electrons provide the lower wavelength electromagnetic waves, which can be used to achieve high resolutions. In the best-case scenarios, a magnification of nearly 100,000x can be achieved with an SEM.

For SEM operation, the electrons emitted from an electron gun are accelerated using an electric field of 0.1-30 kV. They are then passed through a series of magnetic lenses that focus the beam to a single point as shown below in Figure 14. The electrons that are reflected/ emitted from the sample are then collected by a detector. By rastering the electrons through the sample grid, a 3D image of the sample is formed.

The images formed in an SEM are mainly from two sources of electrons. The first are the secondary electrons, which are electrons emitted due to sample excitation. These electrons form as a result of the ionization of the sample by the incident primary electron source. Most SEMs image using secondary electrons to attain a high depth perception of the sample.

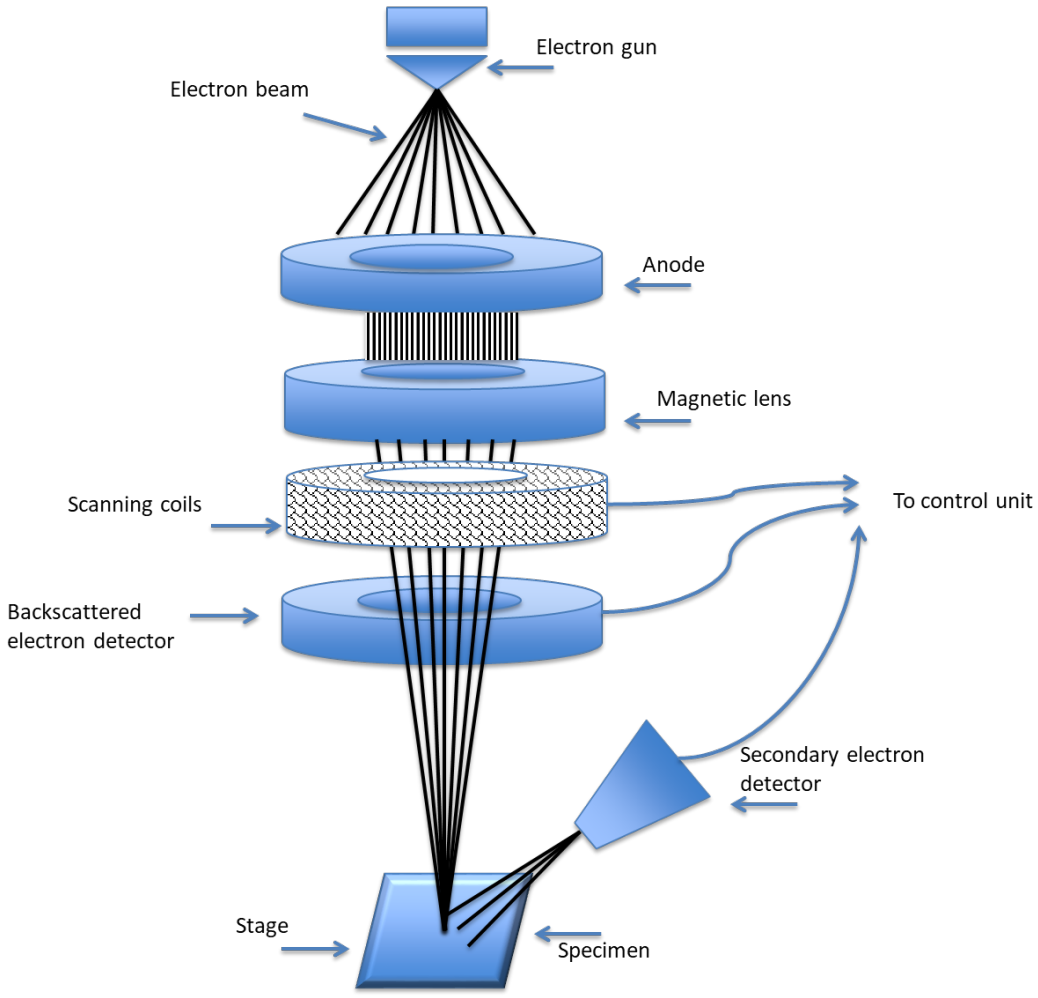

Figure 14: Schematic of a scanning electron microscope showing the various magnetic lenses and other components

The second source of the image is the back-scattered electrons, which are electrons that are reflected back from the sample. These are the primary electrons that bounce back from the sample and move towards the detector. Back-scattered electrons are mainly used to differentiate elements of different atomic weights in samples, since the intensity of reflection depends strongly on the atomic mass of the element.

SEM is mainly used as an imaging technique to study the surface morphology and the topography of the material. But based on the magnification level, it could also be used to grain boundaries and other bulk features in the material. It can also be used to obtain cross-sectional images of samples based on the direction of sample imaging[118]. In all these cases though, it is still only imaging the surface of the given specimen which is why it is considered a surface characterization technique.

2.3.3. Transmission Electron Microscopy

Transmission Electron Microscopy or TEM is another important imaging technique that uses an electron beam as the illumination source[119–121]. This technique is similar to SEM in that it uses the interaction of electrons with matter to provide high resolution images of samples. The key difference lies in the mode of interaction of the electron with the material. As the name suggests, TEM utilizes the electrons that are transmitted through thin samples to create an image. These electrons that pass through the material constitute the unscattered electrons. TEM therefore utilizes the wave-nature of electrons to create high-resolution images of matter that can be resolved to as high as 0.2nm.

A schematic of the TEM operation is shown in Figure 15 below. The method of operation of TEM is like that of the SEM. Electrons emitted from a gun source are accelerated and focused using and electric fields and magnetic lenses. Typical accelerating voltages for TEM operation are between 80-300 kV. These high energy electron sources are then bombarded onto the sample. The samples are prepared extremely thin (in the order of nm), so that most of the electrons pass through them. These “transmitted” electrons are

detected using a phosphorous screen or a camera which is used to obtain a 2D image of the sample. In the best scenarios, the magnification can be as high as 500,000x.

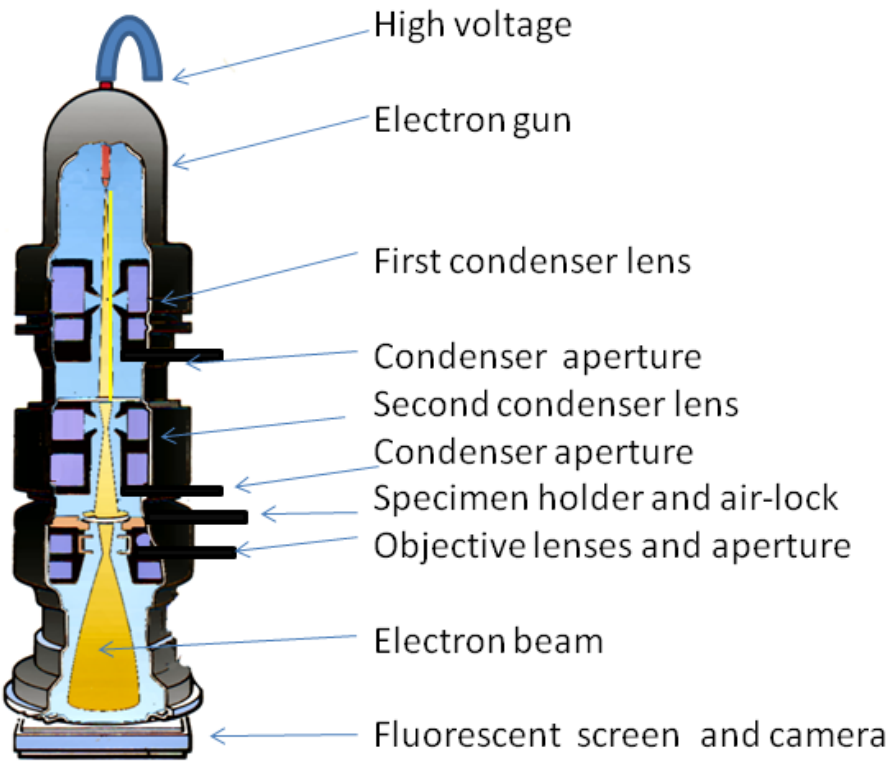

Figure 15: Schematic of a transmission electron microscope showing the electron gun, magnetic lenses, flourescent screen and other parts[122]

TEM is used to observe several important aspects of the sample such as the grain boundaries[123,124], formation of surface films[125,126], crystal planes and lattice imaging[127,128], etc. TEM can also be used to study diffraction patterns in the sample and thus receive important information about the crystal structure of the material being studied.

There are two important modes of operation of TEM: bright field and dark field imaging[119]. Bright field imaging is the more common mode that uses the direct beam from the source

that is perpendicular to the sample. But in some cases, a diffracted beam can also be used, mainly to study different grains and phase regions in a crystalline material. This mode is called dark field imaging and is used extensively in crystallographic and metallurgical studies.

Lastly, TEM can also be used to obtain elemental information about the sample using energy dispersive X-ray spectroscopy (EDX) as well as the Electron Energy Loss Spectroscopy (EELS)[129]. In both these techniques, the incident electron beam causes an ionization of the sample or interacts with the sample causing a loss in the incident electron energy that can be useful in identifying the elements present in the sample.

2.3.4. X-Ray Diffraction

X-Ray Diffraction, commonly known as XRD is a popular bulk characterization technique used to understand different aspects of the crystal structure of a material[130–135]. It is a very prevalent technique used by materials scientists to identify the crystallinity, composition and point groups of samples as well as for phase identification in multi-phase materials. It can also be used to determine the size of the crystallite using the full width half maximum (FWHM) of the XRD peaks[136–139], as well as the composition of composite samples containing more than one crystalline species.

XRD is a non-destructive technique that works on the elastic scattering of X-rays by the crystal planes in a material. It is considered a bulk characterization technique since the depth penetration and the interaction volume for X-rays with the sample is of the order of a few tens of microns. This provides averaged information over several thousands of layers of atoms present in the material.

The principle of XRD is usually expressed in the form of Bragg's law[140] that gives the angles of coherent scattering for an X-ray. It can be represented mathematically as:

$$2dsin\theta = n\lambda$$

where, d = inter-planar spacing between crystal planes (which can be calculated using the Miller indices (hkl) for the crystal structure as $d = \sqrt{h^2 + k^2 + l^2}$

θ = angle of incidence of the X-ray (measured as the angle between the X-ray and the crystal plane)

n = a positive integer

λ = wavelength of the incident X-ray

In a typical XRD experiment, an X-ray beam illuminates the sample and is diffracted by the crystal planes in the material in different directions. Based on the constructive or destructive interferences of these diffracted X-rays, peaks are produced at particular angles which are picked up by a detector. By varying the angle of incidence for the X-rays, peaks are produced at different positions which can help identify the different crystal planes and their d-spacing. A study of these peak positions, their relative intensities and FWHM can reveal important information about the crystal type, composition and its size. The peak position is specific to the type of material and thus can be used as a fingerprint for the material. By comparing the angle of the peak formation with standard reference data available on several databases, one can accurately identify the crystal structure of the sample under examination.

Consider the schematic of a typical diffraction process shown in Figure 16(a) below. X-rays are incident on a sample and get diffracted by the lattice planes in the crystal. Two

parallel X-rays incident on the sample at an angle θ are diffracted by the crystal lattice. These X-rays exiting the sample undergo constructive interference due to which their intensity is increased. (X-rays can be incident on the lattice planes at several different angles, but only at this particular θ angle do they interfere constructively. At other angles near θ, the interference is only partially constructive or even destructive). These X-rays, which are now at a 2θ angle with respect to the source, are then picked up by the detector at a higher intensity than the background signal. Thus, by knowing the angle made by the source and detector (2θ), one can determine the inter-planar distance of a particular set of planes in the crystal lattice. By varying the incident angle through a range of values, the researcher can obtain an X-ray diffractogram for the sample, which can be used to identify various crystal parameters. A typical diffractogram for lithium cobalt oxide powder is shown in Figure 16 (b).

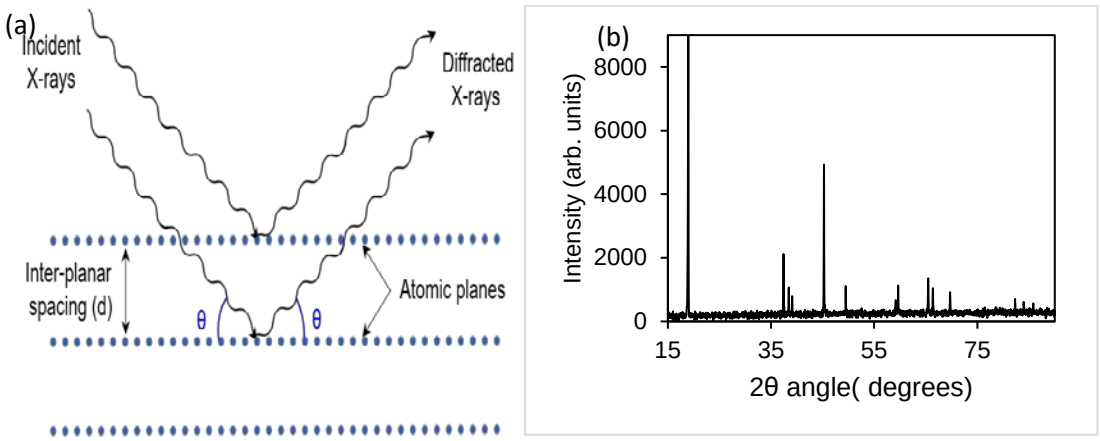

Figure 16: (a) Schematic of Bragg's diffraction on cryal planes (b) Typical XRD pattern obtained for lithium cobalt oxide powder

XRD is therefore a simple and powerful technique used as one of the primary characterization methods for crystalline materials. The ease of using the instrument and

the speed of data collection make it a popular technique that can identify several important sample features at the nano-scale.

Chapter 3: Electrochemical performance of LCO cathode in aqueous environments

3.1. Degradation and stabilization of lithium cobalt oxide in aqueous electrolytes

3.2. Abstract

We report herein the exceptional cycle stability of LCO in aqueous electrolytes of high lithium salt concentrations. We demonstrate retention of up to 87% of the initial discharge capacity after 1,500 cycles at a 1C charge–discharge rate. We also demonstrate that LCO, when in contact with each of the aqueous electrolytes tested, exhibits a high electrode potential and a large initial discharge capacity, similar to that of LCO electrochemically cycled in conventional organic electrolytes. More importantly, our systematic studies and post-mortem analyses of LCO cells reveal that the primary mechanism of LCO degradation in aqueous electrolytes is the formation of a resistive layer of cobalt(II) oxide on the particles' surfaces. We show that higher electrolyte molarity and certain salt compositions may significantly reduce the layer thickness and dramatically improve LCO stability. These findings constitute a substantial step towards development of gravimetrically and volumetrically energy dense aqueous lithium ion batteries.

3.3. Broader context

LIBs with aqueous electrolytes are significantly safer, more environmentally benign and potentially cheaper than traditional LIBs comprising organic electrolytes. Higher ionic mobilities for the Li+ ions in aqueous electrolyte solutions give more power and allow

significantly faster charging of aqueous batteries. Such characteristics are highly desired for growing energy storage applications, including energy storage for electric vehicles and electrical grids increasingly reliant upon intermittent clean and renewable sources of energy. LCO remains the dominant cathode material in commercial LIBs used in electronic devices. It has been known to degrade in aqueous environments, but the origins of such a degradation remain unclear. In this chapter, we uncover the key degradation mechanisms of LCO in aqueous electrolytes. More importantly, we reveal an opportunity to dramatically enhance its electrochemical stability by tuning the composition and increasing the concentration of low-cost lithium salts in aqueous electrolytes. The demonstrated 87% capacity retention in LCO after over 1,500 charging and discharging cycles is unprecedented. The obtained results will contribute to the progress in the broad field of aqueous metal-ion batteries.

3.4. Introduction

John Goodenough et al. pioneered the use of lithium cobalt oxide (LCO) as a unique lithium ion battery (LIB) cathode material[141]. Following Goodenough's work, LCO was commercially produced and successfully utilized in a majority of LIBs by multiple companies. Widespread use of LCO is owed in part to its high volumetric capacity (1,363 mAh cm^{-3}), high discharge potential (approx. 3.93 V vs. Li/Li^{+}), and long cycle life[141,142]. Low thermal stability and faster degradation at higher currents remain downsides for the use of LCO in today's commercial LIBs[142]. The propensity for LCO to decompose in an exothermic reaction that releases oxygen, in combination with highly flammable organic electrolytes, adds a significant safety risk to the use of LCO-based LIBs[12]. As a result, safety measures often require overbuilding battery management systems (battery

packs) with inactive materials, which increase the weight, volume and cost of the energy storage by up to 75% in case of cell applications in large batteries, such as electric vehicles[13].

A variety of commercial cathode materials used in today's commercial LIBs ($LiFePO_4$ (LFP), LCO, $LiNi_xCo_yMn_zO_2$ (NMC), $LiMnO_2$ (LMO), etc.) have been preliminarily studied in combination with aqueous electrolytes[26–28,143]. However, in contact with aqueous electrolytes, such materials typically exhibit poor electrochemical performance and short cycle life. While a detailed understanding of the electrode and ALIB cell degradation phenomena is still mostly lacking, several factors have recently been proposed to impact cell stability, such as electrolyte pH and dissolved oxygen content[29], dissolution of the active material, intercalation of H^+ ions into the active material alongside Li^+ ions, and reactions between the active material and dissolved O_2 and H_2O[20]. In our recent studies on the electrochemical cycling of LFP cathodes in aqueous solutions we identified that side reactions occurring between LFP particles and water molecules induce surface dissolution and electrochemical separation of active particles. More importantly, we discovered that increasing the concentration of the lithium salt in the aqueous electrolyte leads to significant reduction of the dissolution reactions and leads to improvements in cycle stability[13]. Inspired by such findings, we investigated the electrochemical behavior of higher voltage LCO in low-cost Li_2SO_4 or $LiNO_3$-based aqueous electrolytes.

Similar to our previous study, we found that higher salt concentration leads to increased cathode stability. However, in contrast to our prior work, the degradation mechanisms in LCO were found to be markedly different than that in LFP. Instead of electrical separation of active particles, LCO electrodes develop an ionically isolative surface layer, which high concentration electrolytes may prevent building. While some of the electrochemical

properties of LCO have been previously investigated[27,33,35,144], the comprehensive studies of the mechanisms of LCO degradation as well as the impact of salt concentration and composition have not been reported, and ultra-long cycle stability of LCO in aqueous electrolytes has not been achieved before.

3.5. Experimental section

Electrode Preparation: Commercial lithium cobalt oxide (99.8%, Sigma Aldrich, USA) was mixed with pure black conductive additive (Superior Graphite, USA) and polyvinylidene difluoride (HSV 900, Kynar, France) binder in the ratio 70:15:15. This mixture was stirred along with N-methyl pyrrolidone (Sigma-Aldrich, USA) for 24 hours on a magnetic stirrer. The slurry was then cast onto a titanium foil (99.6%, GalliumSource LLC, USA) of 0.0125mm thickness. These electrodes were dried at 70^{o}C for 12 hours. Circular electrodes were then cut out from these foils. Working electrodes (WE) of 7/16" ø counter electrodes (CE) of 7/8" ø were used. The working electrode was also thinner (0.003") than the counter electrode (0.008") so that the mass of the CE was at least five times larger than that of the WE.

Electrochemical testing: For charge discharge studies, the WE and CE were spot-welded onto titanium flags (Trinity Brand Industries, USA) and sandwiched between two Teflon blocks using a glass fiber separator (GF/B grade Whatman Glass microfiber). The assembly was immersed in 100ml of the aqueous electrolyte. The electrolytes were prepared by dissolving either lithium nitrate (99%, Alfa Aesar) or lithium sulfate (98%, Sigma-Aldrich) in 100ml of distilled water. Different concentrations of electrolytes (1M, 5M

and 9M for $LiNO_3$ and 0.5M, 1M and 3M for Li_2SO_4) were prepared to study the effect of salt concentration on the stability of LCO.

Constant current charge-discharge experiments were performed using a 25% delithated counter electrode which also served as the reference electrode in the setup (the counter electrode was delithiated separately by 25% of its total capacity by mass, using a constant current and a titanium foil counter electrode). The WE was cycled between +0.15 V to -0.2 V vs. the CE. These tests were conducted using an Arbin Testing System (Arbin Instruments, USA). For cycling voltammetry, an Ag/AgCl electrode (3M NaCl) was used as the reference electrode and a 25% delithiated LCO electrode was used as the counter electrode. CV data was collected at a scan rate of 0.05 mVps using a Gamry Reference 600 Potentiostat. EIS measurements were also taken after cycling LCO in different electrolytes using the Gamry Potentiostat. The impedance measurements were taken between 10MHz to 0.05Hz.

***Post cycling electrode characterization*:** After cycling, the working electrodes were washed with distilled water and dried in ambient temperature. These were then characterized to analyze for changes in structure and composition. SEM images were taken using the LEO 1530 thermally assisted field emission SEM with EDS. A 4 kV accelerating voltage was used for sample imaging. TEM images were collected using the Technai G2 F30 Transmission Electron Microscope operated between 100-300 kV. For XRD, the cycled electrodes were mounted flat onto the sample holder of a X'Pert Pro Alpha-1 instrument. A Cu K-α source was used at an accelerating voltage of 45 kV and a current of 40mA. XPS data was collected using a Thermo K-Alpha XPS spectrometer with an Al K-α source. The pass energy was kept at 200 eV for survey scans and 50 eV for detailed scans.

3.6. Results and discussion

Figure 17 shows the cyclic voltammograms (CVs) for LCO in aqueous electrolytes of $LiNO_3$ and Li_2SO_4 salts of varying molarities (1M, 5M and 9M/saturated $LiNO_3$ solution, and 0.5M, 1M and 3M/saturated Li_2SO_4 solution). These CVs show a de-lithiation peak at approximately 3.94 V vs. Li/Li^+ for LCO. A corresponding re-lithiation peak appears at approximately 3.92 V vs. Li/Li^+. These potentials correspond to a Li^+ ion concentration of 1M in either of the electrolytes. With increasing molarities of electrolytes, there is a corresponding increase in the redox potential of these peaks in accordance with the Nernst equation. These results confirm that our cell construction is robust and LCO is active in aqueous electrolytes.

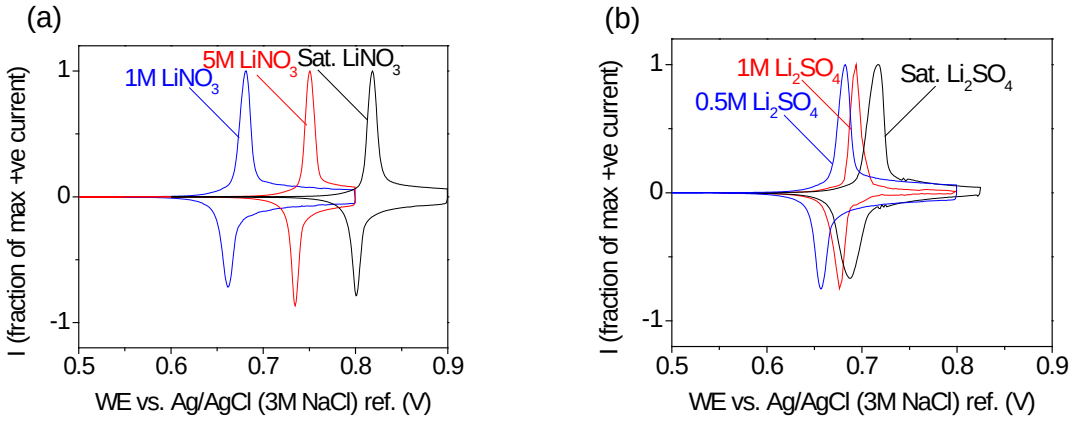

Figure 17: Cyclic voltammograms for LCO in different electrolytes: (a) lithium nitrate and (b) lithium sulfate of different molarities. All CVs were conducted at a scan rate of 0.05 mVps and all potentials are with reference to a Ag/AgCl electrode using 3M NaCl (0.21 V vs. SHE)

To understand the charge-discharge (C-D) behavior of LCO in aqueous electrolytes, electrochemical cells were assembled with electrolytes of varying molarities of $LiNO_3$ and Li_2SO_4 salts, as used in the CV experiments. In order to minimize the impact of the counter electrode (CE) on cell performance, both the working electrode (WE) and CE were constructed with LCO as the active material. The CE was constructed to exhibit a larger capacity loading and was partially delithiated to allow Li^+ cycling between the two electrodes (without partially removing Li^+ from the CE, the CE would have no storage capacity for Li^+ when Li^+ is extracted from the WE). A constant current corresponding to a 1C rate of C-D was applied between the WE and CE, with the potential of the WE versus the CE limited to between +0.15 V to -0.2 V (Figure 18).

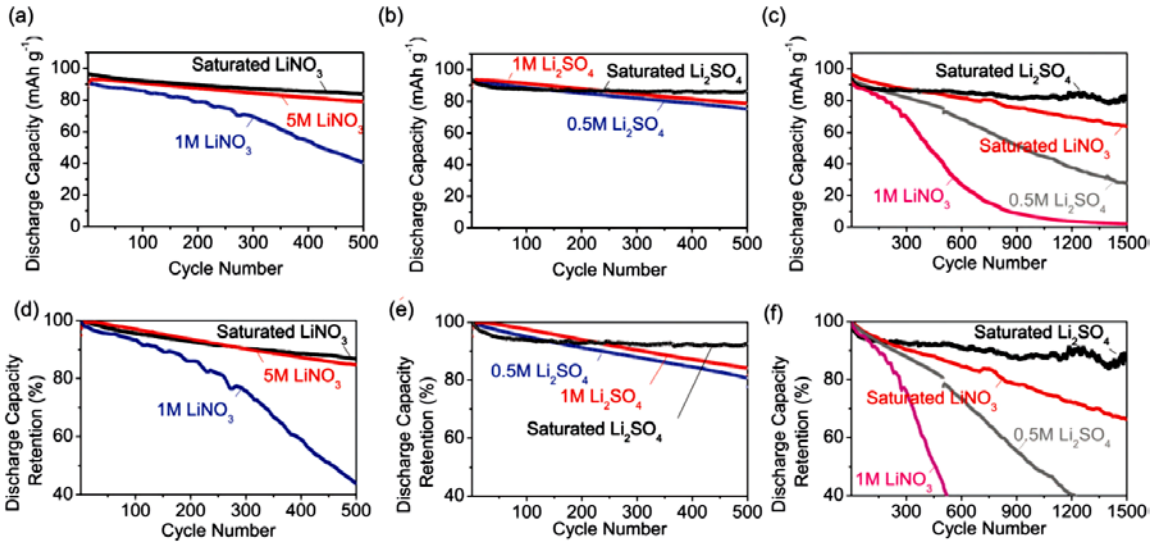

Figure 18: Charge-discharge plots for LCO in aqueous solutions of (a) lithium nitrate and (b) lithium sulfates of different molarities. The corresponding capacity retention for LCO in different electrolytes as a percent of the maximum is shown in (d) and (e). (c) & (f) Comparison of charge-discharge and capacity retention for longer times in lowest concentration and saturated electrolytes. All cells were cycled at 1C rate.

Lithium nitrate and lithium sulfate were chosen as candidate salts of lithium due to their low cost, which could help reduce the overall price of the electrolyte. And although this section primarily focuses on the performance of LCO in these two salts, other electrolytes were also tested. These included lithium chloride, lithium acetate and lithium benzoate. Performance with lithium chloride is report in the next section of this thesis. But LCO showed no performance in lithium acetate and lithium benzoate salts, possibly due to some sort of electrolyte decomposition at the high voltage of operation of the cathode. This effect was not investigated further.

A higher concentration of the lithium salt substantially increased the capacity retention for LCO. Interestingly, LCO exhibited more stable cycling in the Li_2SO_4 solution than in the $LiNO_3$ solution, which is clearly seen in the case of saturated electrolytes or when comparing the capacity retention for lower concentration - 0.5 M Li_2SO_4 solution and 1M $LiNO_3$ solution - in which the Li^+ concentrations were equal (Figure 18. c, f). Based on the previous findings made by our group while studying LFP cathodes, improvement in discharge capacity retention with higher lithium salt concentration is likely connected to a reduction in the water activity and water-induced undesirable side reactions (to be further discussed), and a corresponding increase in the lithium activity. As a result, LCO maintained a remarkably large part of its capacity (≈87%) after 1,500 cycles in concentrated Li_2SO_4 electrolyte, which is high even for commercial quality LIBs with organic electrolyte.

Figure 19 shows changes in the corresponding voltage-capacity plots for the electrochemical cells. We see an increase in the polarization of these cells with cycling, evident from the broadening or separation of the charging and discharging curves with cycling. With the exception of the saturated $LiNO_3$ electrolyte, this polarization is more

prominent for electrochemical cells which degrade faster (such as those constructed with 1M $LiNO_3$ electrolyte) than for electrochemical cells that degrade slower (such as those assembled with saturated Li_2SO_4 electrolyte). Higher polarization of the cell with saturated $LiNO_3$ electrolyte (even when compared to the 5M $LiNO_3$ electrolyte cell, compare Figure 19. b & c) is likely related to the observed (visible by eye) recrystallization of $LiNO_3$ into larger crystals in the electrolyte upon slow water evaporation (our cells were sealed but were not perfectly hermetical). Such crystals may block electrolyte access, inducing undesirable polarization growth. In contrast, saturated Li_2SO_4 electrolyte does not exhibit this behavior – it tends to precipitate salt crystals at the bottom of the cell due to lower solubility in water and lower solvation energy. As a result, the corresponding cell polarization remains small even after 1,500 cycles (Figure 19. f).

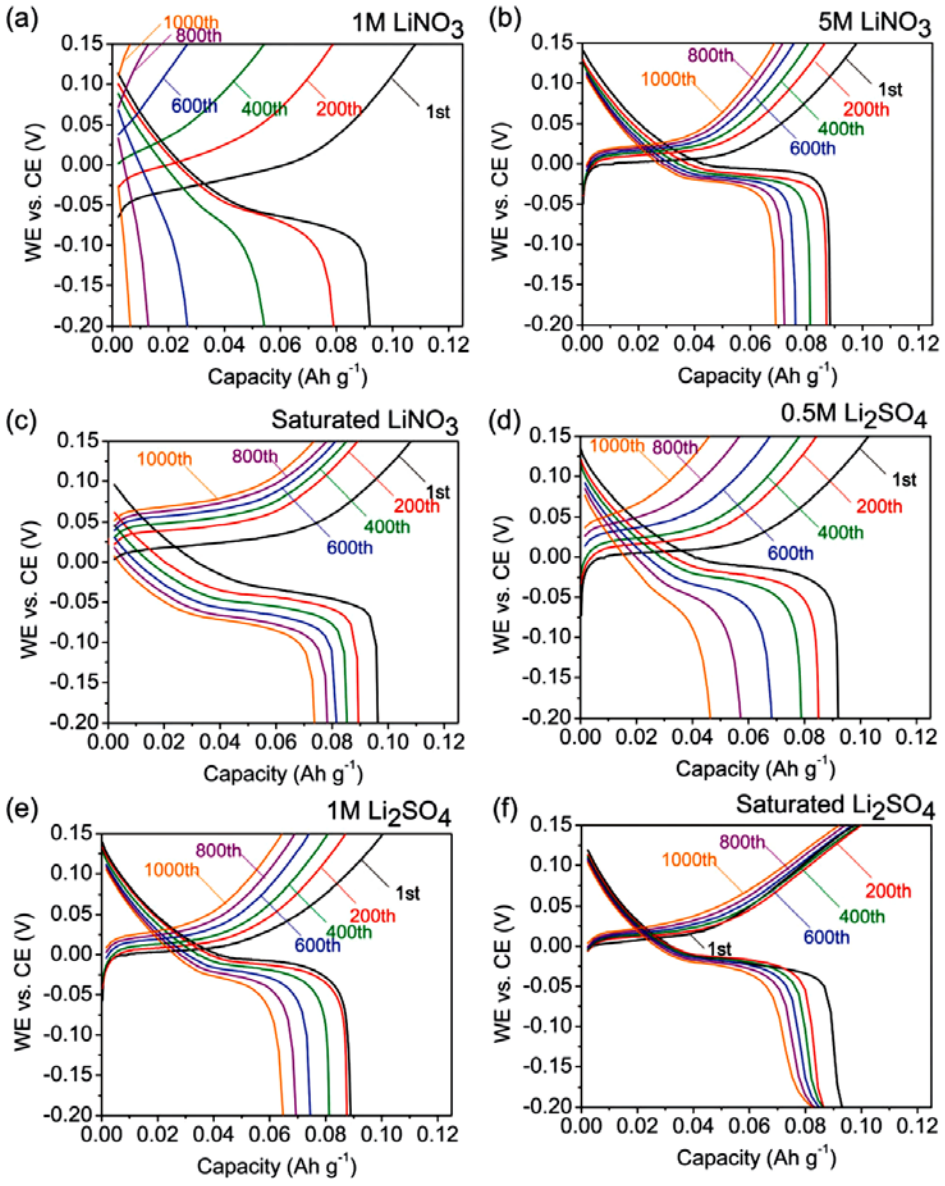

Figure 19: Voltage–capacity plots for LCO after cycling in different electrolytes. Larger degradation increased the polarization of the electrodes.

Electrochemical impedance spectroscopy (EIS) was performed on the cycled electrodes at regular intervals to gain additional insights into the nature of the degradation of performance (Figure 20). Figure 20 (a) and (b) show changes in EIS in the worst (1M $LiNO_3$) and the best (saturated Li_2SO_4) performing cells. EIS measurements were taken

after 1, 30, 100, 250, 500 and 1,500 cycles. We see an increase in the overall cell resistance (Z-real) with cycling. We also see a direct correlation between cell capacity fading and cell resistance increase after 500 cycles in all the electrolytes (Fig. 4 c, d). Higher resistance corresponds to a higher degree of degradation, consistent with trends in polarization observed in the C-D tests (Fig. 3).

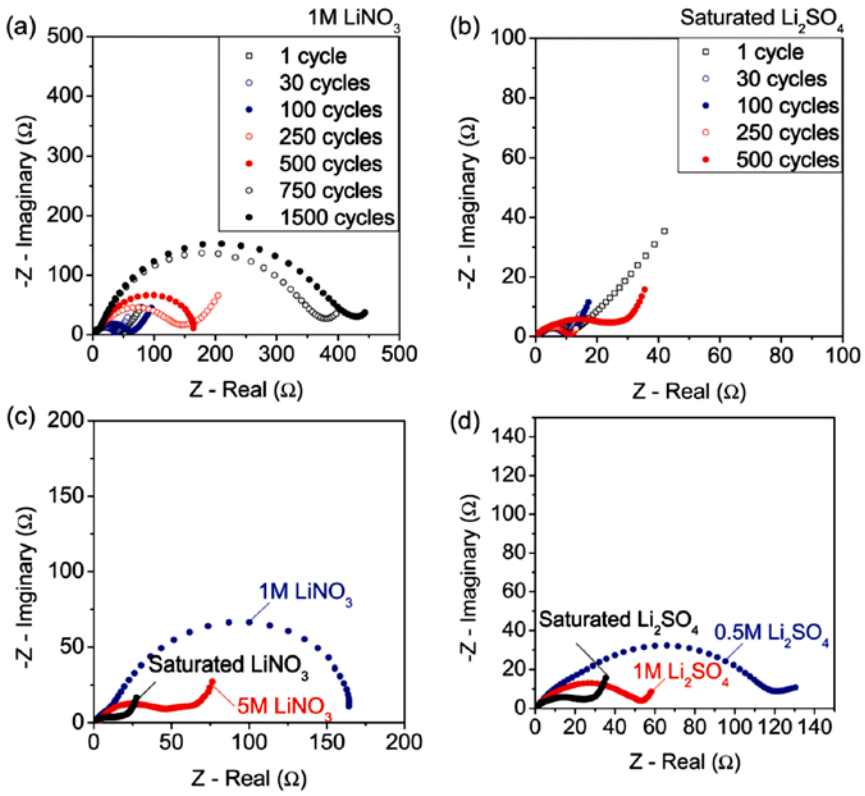

Figure 20: EIS measurements for LCO in (a) 1M $LiNO_3$, (b) saturated Li_2SO_4 after different number of cycles, (c) and (d) EIS comparison for LCO after500 cycles in different molarities of lithium nitrate and lithium sulfate.

To identify the changes to the LCO electrodes during cycling we conducted extensive post-mortem analysis using a broad range of surface-sensitive and bulk material characterization techniques. For microstructural imaging at the nanoscale, LCO particles

were examined using high resolution TEM (HRTEM) (Figure 21). The surfaces of LCO were imaged after cycling electrodes in 1M $LiNO_3$ solution (for which there was the largest loss of discharge capacity and greatest rise in impedance) for 500 and 1,500 cycles (Figure 21 b, c). The surfaces of uncycled LCO were also imaged as a reference (Figure 21 a). Uncycled LCO powder showed the lack of any surface films and the extension of crystal planes all the way to the particle surfaces (Figure 21 a). On cycling, however, an amorphous layer forms on the surface (no crystal planes were visible). This amorphous surface film increases in thickness with longer cycling (from 5-6 nm in thickness after 500 cycles to 8-10 nm in thickness after 1,500 cycles in 1M $LiNO_3$). Noticeably thinner surface layers were observed on LCO cycled in the electrolytes that were more stable (e.g., in the case of 0.5M Li_2SO_4 the thickness was 2-3nm after 500 cycles). In some LCO areas in the 0.5M Li_2SO_4 electrolyte, crystal planes extended all the way up to the surface, although there was a noticeable change in the crystal plane spacing (as seen in Figure 21 d), suggesting a phase change on the surface layer after 500 cycles. This effect was noticed to lower extents in cells cycled in 1M and saturated Li_2SO_4 electrolytes where the performance was much more stable. HRTEM image analysis was also conducted to reveal the crystal structure of the layers formed at the surface of the LCO grains after cycling. Figure 21 f shows an example of the nanocrystals formed on the surface of the LCO sample cycled in 0.5M Li_2SO_4 for 500 cycles. The measured d-spacing values of such nanocrystals match closely with the 2.46 Å spacing of the (111) planes in CoO, while that of the bulk grain match closely with the 4.68 Å spacing of the (003) planes in LCO (Table 2). The surface chemistry was investigated further with XPS.

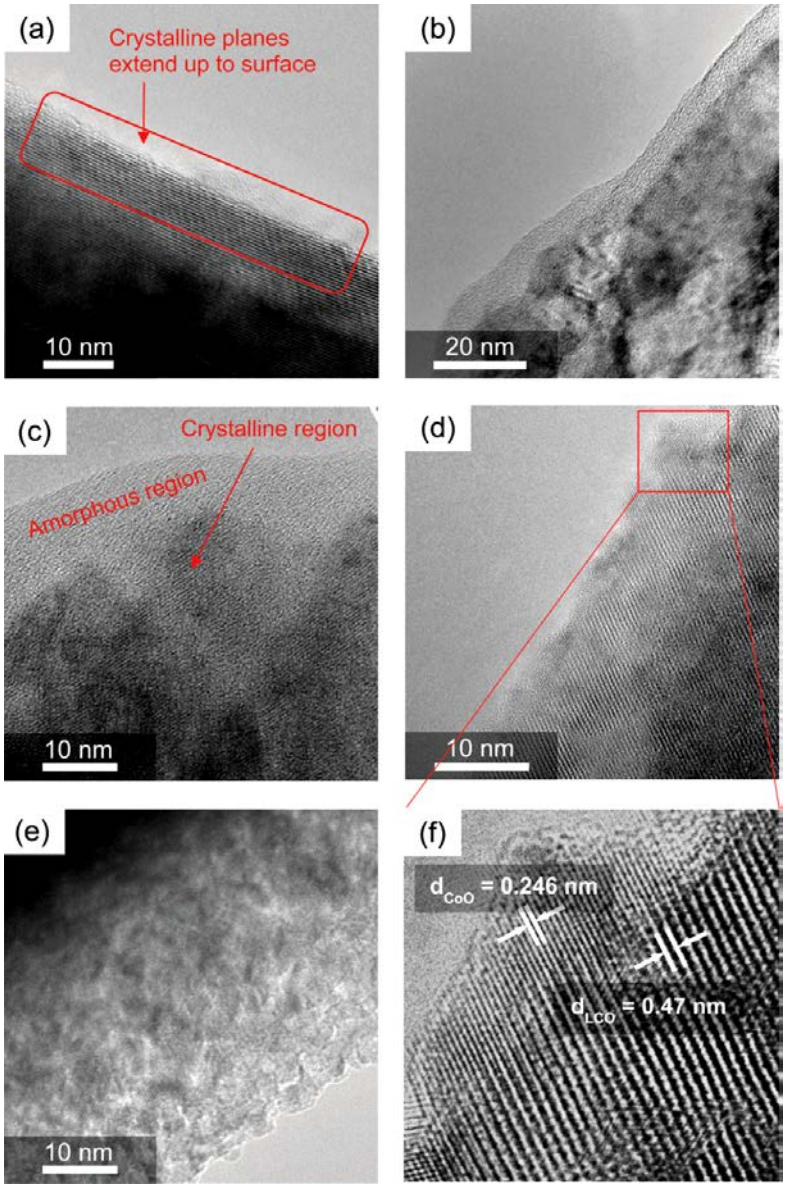

Figure 21:TEM images of (a) uncycled LCO particle, (b) and (c) LCO cycled in 1 M $LiNO_3$ for 500 and 1,500 cycles respectively, (d) and (e) LCO cycled in 0.5 M Li_2SO_4 for 500 and 1,500 cycles respectively (f) enlarged image of electrode.

h	*k*	*l*	*d*
0	0	3	4.683
1	0	1	2.401
0	0	6	2.341
0	1	2	2.303

(a) Lithium cobalt oxide: Layered structure, a= 2.815Å, c = 14.05Å

h	*k*	*l*	*d*
1	1	1	2.46
2	0	0	2.13
3	1	1	1.284
2	2	2	1.23

(b) Cobalt (II) oxide: Rock-salt structure, a = 4.2615Å

Table 2: Crystal structure and d-spacing parameters for LCO and Co(II)O. The values shown in red are denoted in the TEM images.

XPS was conducted on electrodes to investigate the composition of the surface layers detected by TEM. Electrodes cycled in the different electrolytes of varying concentrations were analyzed for changes in surface composition, oxidation state of cobalt, and the stoichiometric ratio of O:Co. A reference sample of pure LCO was also analyzed using the same parameters. Samples were analyzed using a survey scan to measure the ratio of O:Co on the surface. The peak area under the curve for the Co 2p peak and the O 1s peak of the survey scan (same pass energy) were used to measure the atomic ratio of cobalt and oxygen atoms on the surface (Figure 22).

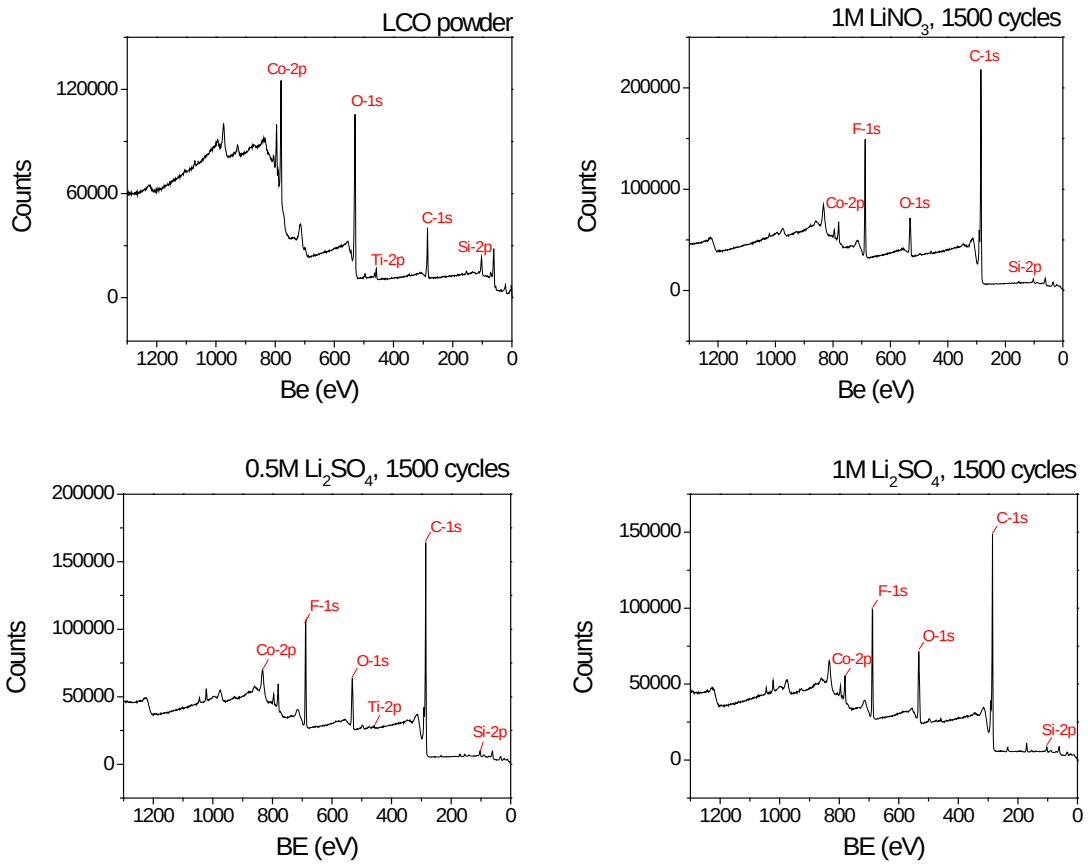

Figure 22: Detailed XPS scans for (a) Uncycled LCO powder, (b), (c), (d) LCO cycled in 1M $LiNO_3$, 0.5M Li_2SO_4 and 1M Li_2SO_4 respectively.

A detailed scan for oxygen 1s revealed the different types of oxygen bonds present on the surface of the particles (Figure 23). Two types of oxygen 1s bonds were observed – one with a peak at approximately 529 eV binding energy, corresponding to the O-Co bond. The other was at approximately 532 eV binding energy that corresponded to the organic C-O bond from adventitious carbon adsorbed on the surface or carbon additives with functional groups on the surface. Curve fitting was carried out using a linear background fit with the proprietary software from Thermo K-Alpha. Using the fit, the fraction of the O-1s peak that corresponded to the O-Co bond was calculated as the fraction of the total

area under the O-1s curve. This fraction was then multiplied with the atomic percentage obtained from the survey scan to obtain the actual contribution of oxygen to the O-Co bond. The ratio of O:Co was then calculated.

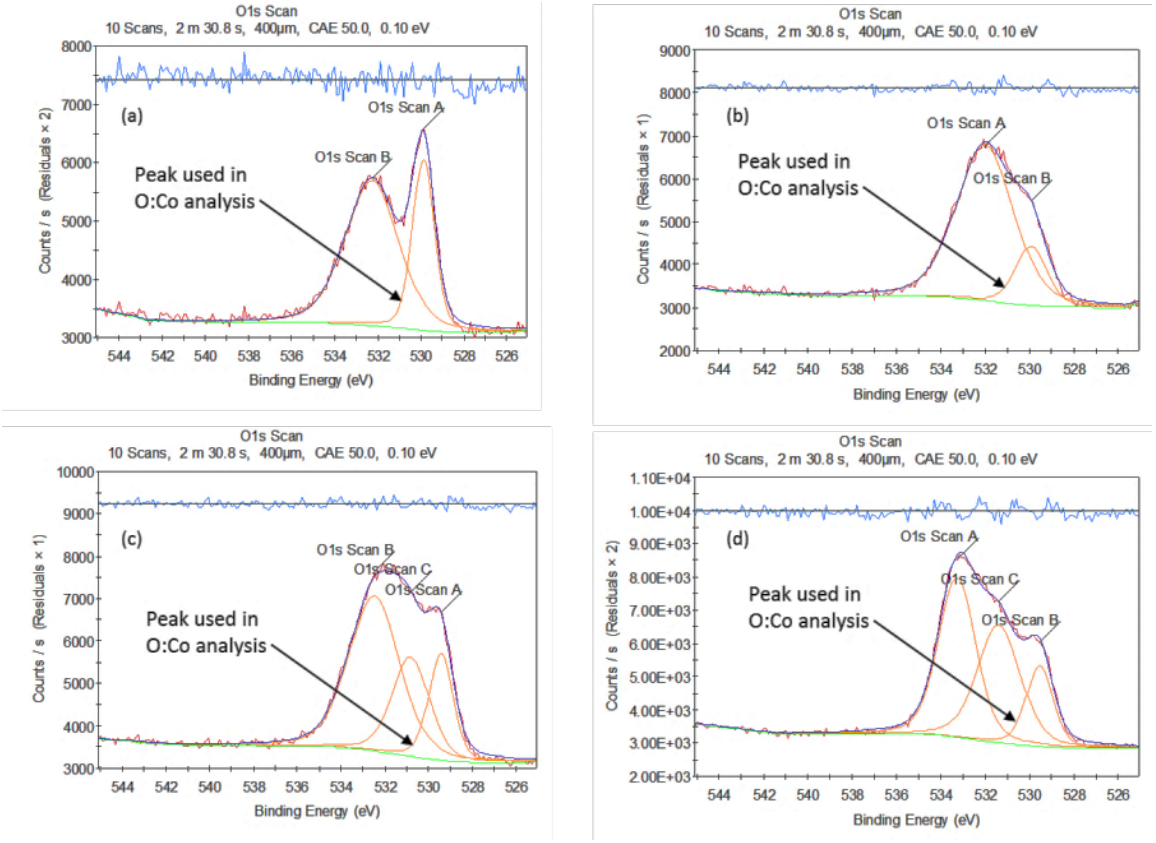

Figure 23: XPS spectra for O-1s peaks in (a) pure LCO and electrodes cycled in different (b) 1M $LiNO_3$, (c) 0.5M Li_2SO_4 and (d) 1M Li_2SO_4 for 1,500 cycles.

As expected, the O:Co ratio was approximately 2:1 for a pure LCO sample. However, with cycling, this ratio sequentially decreased and approached 1.5:1 (as shown in Figure 24). This implies that the surface of the LCO is being reduced over time so that the Co (+III) ions in LCO are slowly converting to the Co (+II) ions with cycling. In other words, the surface composition of $LiCo(III)O_2$ (O:Co=2:1) slowly changed to Co(II)O. This effect was

more pronounced in cells that had degraded more (compare, for example, 1M $LiNO_3$ versus 1M Li_2SO_4, Figure 6). Similar trends were observed in both types of electrolytes ($LiNO_3$ and Li_2SO_4) suggesting that the phenomenon of Li_2O leaching from the surface leading to the formation of cobalt (II) oxide surface layer (Figure 5), that correlates to the capacity fading (Figs. 2-3) and resistance growth (Fig. 4) in LCO, is somewhat universal (at least for studied aqueous electrolytes) and only differs in magnitude - depending on the electrolyte composition and salt concentration.

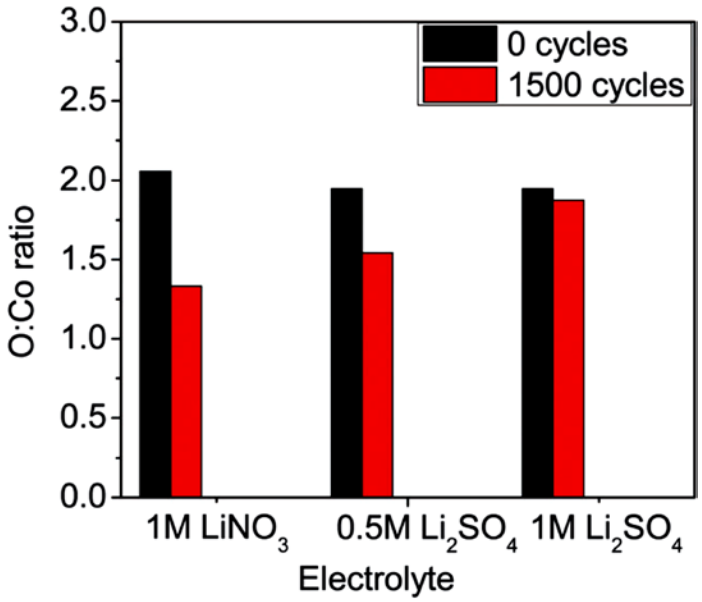

Figure 24: O:Co ratio in LCO samples after cycling as obtained from XPS. The data shows a general trend of higher O:Co ratio for less degraded samples, indicating that the formation of Co(II) oxide on surface causes loss in capacity.

Detailed scans on the Co 2p peak were also analyzed for all samples (Figure 25). It must be mentioned that the binding energy values for all the samples were found to be consistently at ~284.86 eV for the C-C 1s peak (from adventitious carbon) and at ~688.29

eV for the F-1s peak (from PVDF binder), which provided an internal calibration standard for all the samples. The 2p3/2 peak for Co in pure LCO was used as the reference peak and chemical shift in the cycled samples was studied. We noticed that a peak shift occurred towards lower binding energies (BE) in all samples. A shift towards lower binding energies implies that it is easier to extract an electron from the Co ion. This indicates that the Co ions in the surface layer have a lower oxidation state than originally in LCO, providing additional evidence for the reduction of Co (+III) ions to Co (+II) state. We also observed that the shift towards lower binding energies was higher with greater degradation of the electrodes. For example, LCO cycled for 1,500 cycles in either 1M $LiNO_3$ or 0.5M Li_2SO_4 showed a slightly larger shift than LCO cycled for 500 cycles in these electrolytes. On similar lines, it was also observed that the chemical shift after 500 cycles in more concentrated electrolytes (1M Li_2SO_4, lower degradation) was lesser than in less concentrated electrolytes (1M $LiNO_3$), which is in agreement with the charge-discharge tests (Figure 18). Figure 25 summarizes these findings and shows the peak values for BE of the Co 2p 3/2 peak plotted as a function of the percentage degradation in the electrodes.The larger degree of reduction of Co (+III) ions to Co (+II) state (thickness of the cobalt oxide layer on the LCO surface) correlates well with the larger degradation of the electrodes.

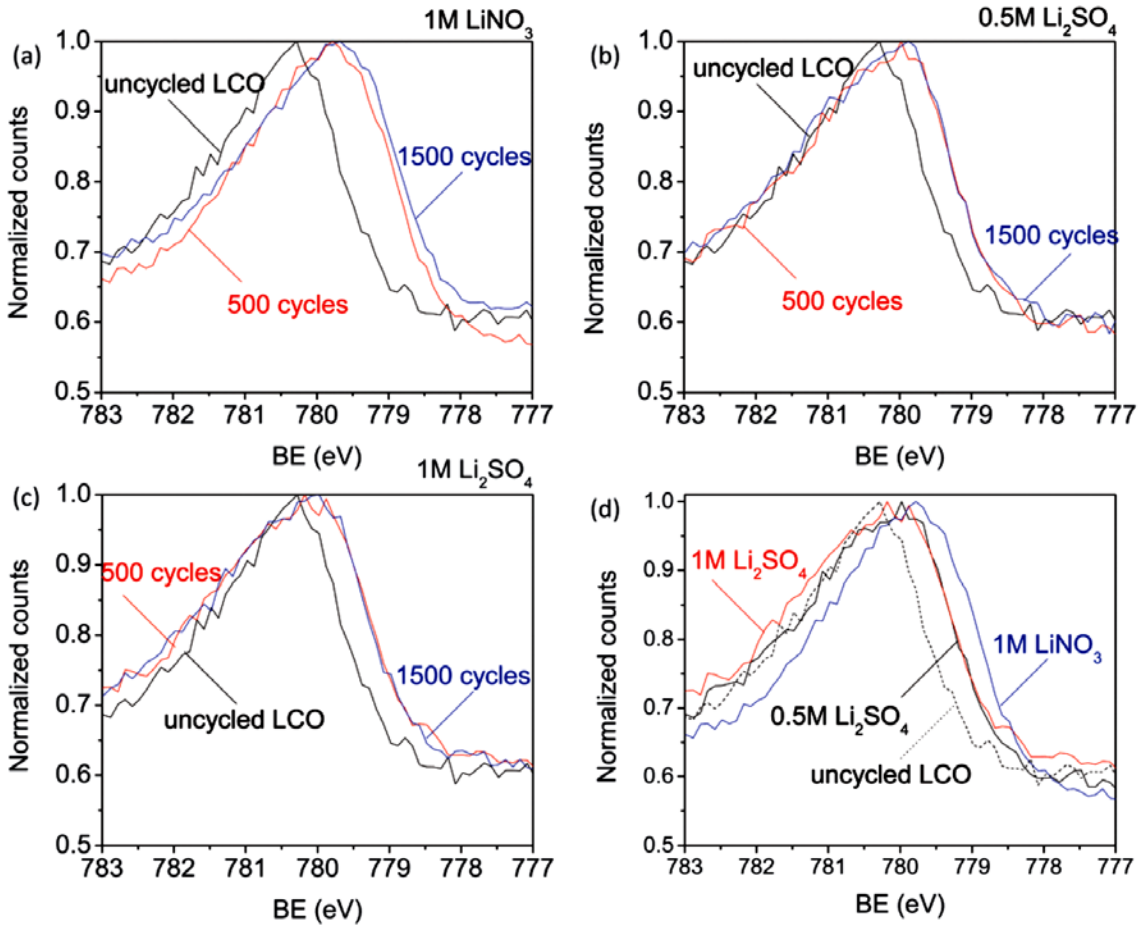

Figure 25: Change in Co 2p peak to lower BE with cycling in (a) 1M $LiNO_3$ (b) 0.5M Li_2SO_4 (c) 1M Li_2SO_4 (implying change from Co(III) state in LiCoO2 to Co(II) state in CoO). (d) Comparison of relative change in Co-2p oxidation state in electrolytes after 500 cycles.

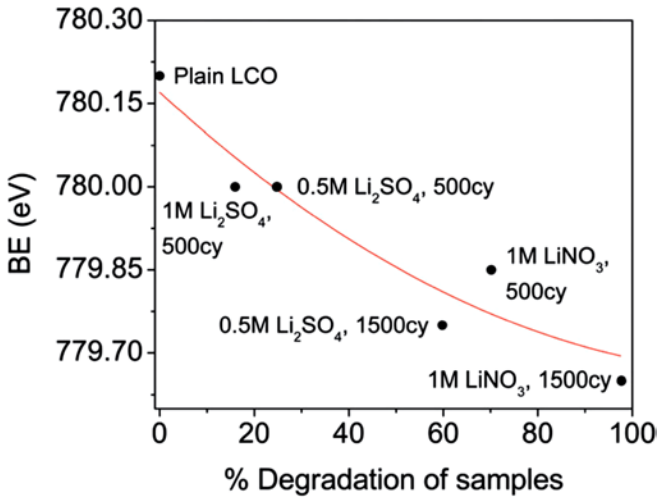

Figure 26: Change in the binding energy of Co in LCO as a function of degradation with cycling. With higher degradation, the values tend towards lower BE, indicating a change to the Co (II) oxidation state.

XRD analyses were performed on selected LCO samples. Figure 27 shows the XRD spectra for LCO electrodes cycled in 1M $LiNO_3$ electrolyte for different numbers of cycles. The XRD spectra reveal that the LCO crystal structure is still present, with no new crystalline phases appearing, even after cycling for 1,500 cycles. This provided additional evidence to support the understanding that the loss of LCO capacity was predominantly a surface phenomenon and no significant changes in the bulk of LCO took place.

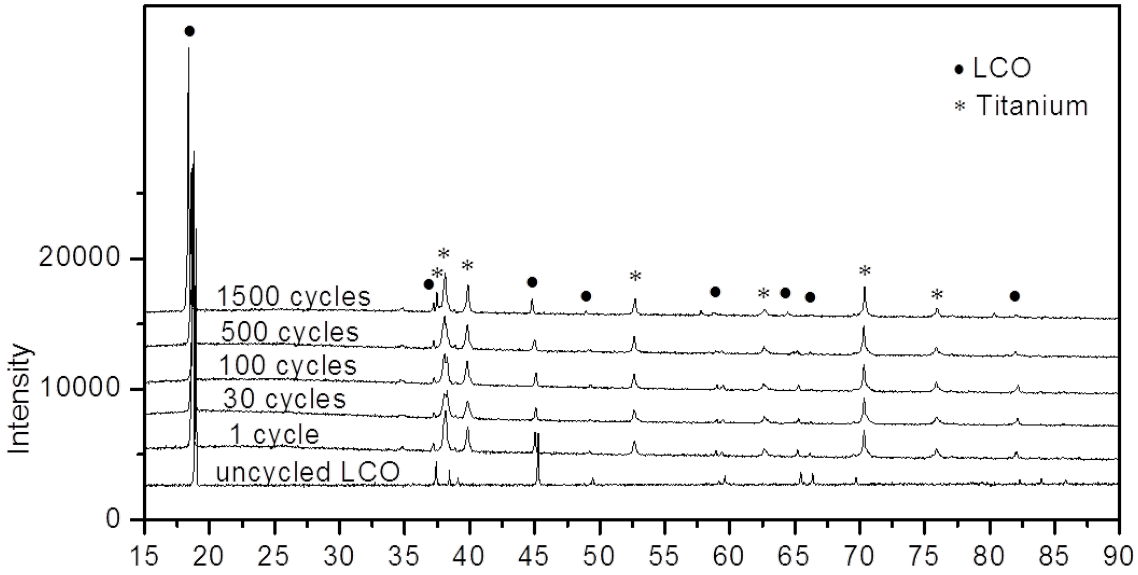

Figure 27: XRD patterns for LCO cycled in 1M $LiNO_3$. Most of the peaks match up even after cycling for 1,500 cycles showing no change in bulk composition. The shift in the (003) peak at 18.5^o can be attributed to a change in d-spacing with increased delithiation of the electrodes.

SEM images provided further evidence that there was no apparent change in the LCO particle morphology after cycling (Figure 28). No cracks or noticeable surface roughening could be observed. This insight further supports the lack of significant chemical and structural changes in the bulk of the LCO particles during cycling.

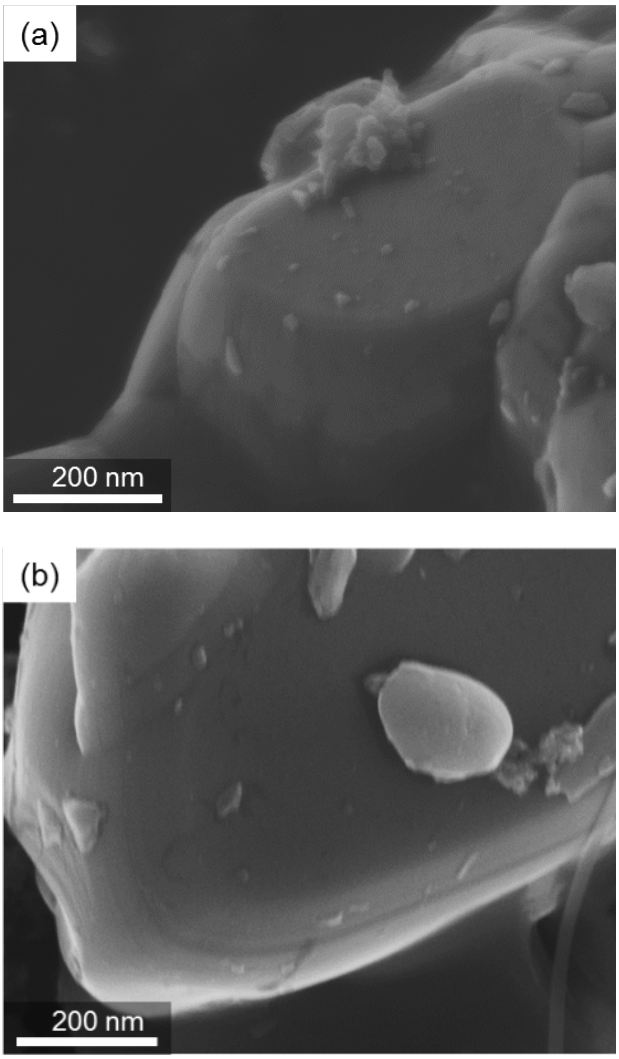

Figure 28:SEM images of LCO (a) before and (b) after cycling in 1M $LiNO_3$ for 1,500 cycles.

In order to distinguish ionic versus electronic resistance growth mostly responsible for capacity fading, cells pre-cycled at room temperature in 1M $LiNO_3$ and 0.5M Li_2SO_4 electrolytes to 40-50% of the initial capacity were then heated to a higher temperature of 60^{o}C and additionally cycled another 10 times (Figure 29). A change in the cell capacity would provide an indication of the kind of resistance in these cells. If the cell resistance was ionic in nature (e.g. due to higher ionic resistance of the surface layer on LCO, Figure

21), an increase in temperature would increase the capacity of the cells since ionic resistance decreases at higher temperatures. On the other hand, if the resistance growth was mostly electronic (e.g. due to higher electronic resistance of such a layer), higher temperature tests would only result in similar or lower cell capacity because electronic resistance is not significantly impacted by temperature (while higher temperature may, in principle, induce further growth of the surface layer). In our case, we noticed a significant increase in the capacity at higher temperatures, indicating that the cell resistance was mostly ionic in nature. An increase in capacity with temperature was seen in both cells (with 0.5M Li_2SO_4 and the 1M $LiNO_3$ electrolytes). However, cell stability in 0.5M Li_2SO_4 at 60^{o}C was noticeably better, consistent with its better stability at room temperature.

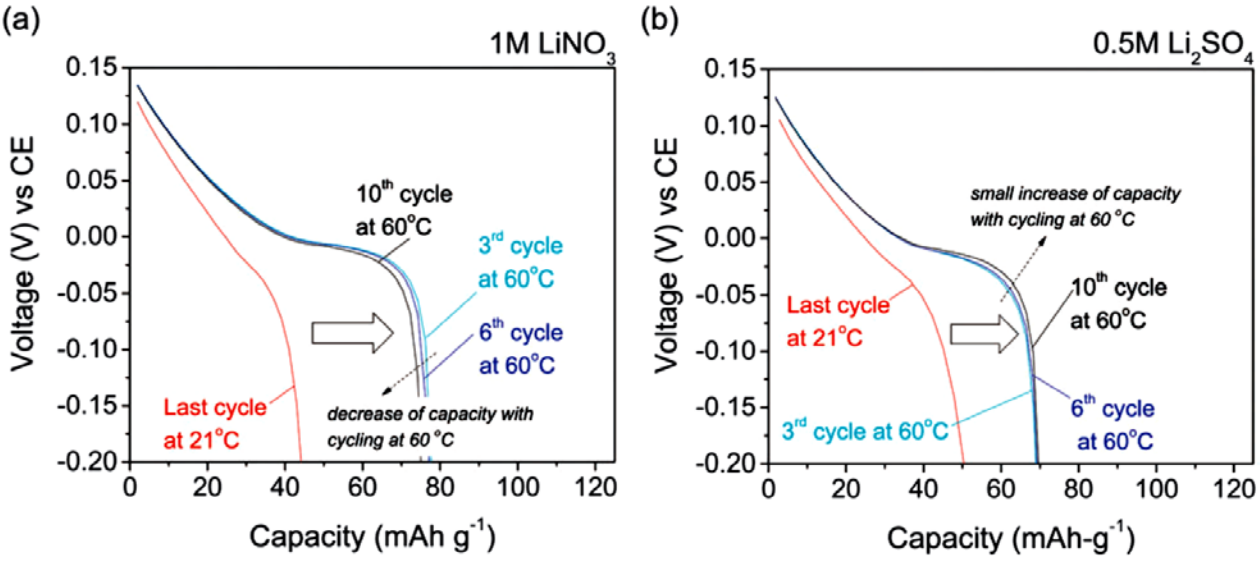

Figure 29: Discharge profiles of the degraded LCO pre-cycled at room temperature before and after temperature increase to 60 °C in (a) 1M $LiNO_3$ and (b) 0.5M Li_2SO_4.

Based on the above described observations of loss of discharge capacity in aqueous electrolytes of various concentrations (Figure 18, Figure 19), correlated rise in impedance

(Figure 20, Figure 21), and formation of a surface layer (Figure 22) rich in Co(II)O (Figure 23, Figure 24, Figure 25), below we weigh possible explanations for the loss of discharge capacity and the benefits of higher salt concentrations. Firstly, multiple observations suggest that diminishing discharge capacity predominantly results from the formation and continuous growth of an ionically-resistive layer due to side reactions of LCO with aqueous electrolytes. Larger diameter impedance arcs in the Nyquist plots (Figure 20) (e.g. larger ionic resistances due to surface layer formation) correlate well with more diminished capacity. Increase in polarization with cycle number observed in the voltage profiles (Figure 19) demonstrate similar trends. A large rise in capacity observed in degraded cells after increasing the temperature from ambient temperature to 60^{o}C suggests that capacity can be largely gained back by overcoming an ionic resistance. A clear correlation between thicker surface layer formation (Figure 21, TEM and Figure 25, XPS) in most degraded cells is consistent with the expectation that the thickness of the surface layer should be proportional to the ionic resistance it creates (assuming compositional differences in the surface layer do not hugely impact the resistance for Li^{+} motion of this surface layer). Increasing salt concentration in aqueous solutions effectively reduces the concentration of water molecules in electrolytes, which are proposed to be mostly responsible for the Co(II)O growth on the LCO surface.

Secondly, dissolution of active material into the electrolyte could also plausibly lead to capacity loss (as in previously studied LFP cathodes[13]), either directly due to the loss of active material or due to reduced inter-particle electrical connectivity. However, since a significant change in the morphology of particles was not observed via SEM studies of the particles before and after electrochemical cycling, since the electrolyte color did not change after cycling (hexaqua-cobalt (II) ions are pink) and since a significant loss of

capacity could be reversed at higher temperatures (Figure 29), we believe that the significant dissolution of LCO is very unlikely to be a dominant degradation mechanism.

3.7. Conclusions

The performance of LCO was systematically investigated in aqueous electrolytes using two low-cost salts of lithium at different salt concentrations. High capacity utilization and rather stable performance was observed in most cells. Higher electrolyte concentration as well as the use of Li_2SO_4 over $LiNO_3$ favored more stable performance. The use of concentrated Li_2SO_4 electrolyte allowed us to achieve a remarkable LCO stability with less than 13% degradation after 1,500 cycles.

By measuring changes in the cell polarization, conducting EIS studies and increasing temperature of the cells after degradation, we identified that the growth of the ionic resistance is the dominant degradation phenomenon. Further studies linked the formation of the layer on the surface of LCO particles to the observed impedance growth. High resolution TEM studies revealed the disordered nature of such a layer. A thicker layer was observed in more degraded cells. Analysis of the O:Co ratio and Co binding energy by XPS studies revealed that this surface layer is composed of ionically resistive Co(II) oxide. Higher degree of conversion of Co(III) ions on the surface to Co(II)ions was found to correlate well with larger impedance growth and more significant cell degradation. Increasing salt concentration in aqueous solutions effectively reduced the concentration of water molecules in electrolytes, which are proposed to be mostly responsible for the CoO growth on the LCO surface. XRD studies suggested that the change in LCO structure

and composition was purely a surface phenomenon and that the bulk of the material remained unchanged.

Chapter 4: Performance of LCO in aqueous electrolytes at low temperatures

4.1. Understanding the Exceptional Performance of Lithium-ion Battery Cathodes in Aqueous Electrolytes at Sub-Zero Temperatures

4.2. Abstract

LIBs with aqueous electrolytes can be excellent candidates for battery applications at low temperatures. In contrast to a common misconception, ALIBs can operate at several tens of degrees below the freezing point of water when high concentration electrolyte solutions are utilized. Furthermore, we report here that the performance of intercalation cathodes in aqueous electrolytes is quite remarkable and superior to that in organic electrolytes at very low temperatures down to about -40°C. We extensively studied the performance of water-based electrolyte solutions based on three low-cost inorganic salts ($LiNO_3$, Li_2SO_4, and LiCl) and that of the corresponding aqueous battery systems to understand the rate-limiting step in the performance at sub-zero temperatures. We found that the charge transfer resistance is the largest impedance contributor at low temperatures, until the complete solidification of the aqueous electrolytes takes place. However, layered cathodes in aqueous electrolytes do not exhibit significant increase in the charge-transfer resistance and reduction in the accessible capacity during charging until the temperature is closely approaching the freezing point, in sharp contrast to their behavior in organic electrolytes. This different behavior explains the dramatically superior performance of LIB cathodes in water-based electrolytes at lower temperatures.

4.3. Introduction

Over the past decade, there has been a growing interest in the scientific and industrial communities in developing water-based lithium-ion and sodium-ion batteries. The aqueous electrolyte chemistry provides better safety and lower cost to the alkali metal - ion technology[13,20,22,34,145]. One perceived disadvantage of ALIBs however, could be the lower temperature range of operation for aqueous electrolytes. At standard conditions, pure water freezes at 0°C. But several applications of LIBs, especially in the sub-zero range, could require them to function at much lower temperatures of -20°C to -30°C[66,146]. And although there have been several studies on organic electrolytes to understand their low temperature performance,[68–71,73,76,147,148] aqueous electrolytes have often been thought to be inoperable much below the freezing point of water. In this context, it is important to understand the temperature range for water-based electrolytes, especially at the lower temperatures.

Typically, conventional LIBs are said to be able to operate down to -20°C[71]. Several research groups have extensively looked into the performance and rate-limiting metrics of organic electrolyte LIBs at sub-zero temperatures. To our knowledge, no similar study has been done to understand the low temperature performance of lithium-ion electrodes in aqueous electrolytes. In this research, we aim to understand these lower limits for water-based systems. Using saturated solutions of lithium salts ($LiNO_3$, Li_2SO_4 and LiCl), we were able to achieve very high capacity of conventional intercalation cathodes and stable performance in these electrolytes at temperatures as low as -40°C to -45°C.

Thermodynamically, pure water freezes at 0°C. However, the freezing point of water can be depressed by the addition of solutes and other additives. These properties have been studied for dilute solutions under the umbrella term colligative properties[77–79,149]. Colligative properties are intrinsic properties of a solution that depend on the ratio of solute to solvent particles. Mostly, colligative properties have focused on dilute solutions (where Raoult's law is applicable) to reduce the freezing point of water by a few degrees centigrade. However, by using concentrated or saturated solutions of salt in water, it is possible to depress its freezing point by several tens of degrees below the thermodynamic value.

In its simplest form, the depression in freezing point can be represented by the formula

$$\Delta T_f = T_{water} - T_{soln} = K_f . m$$

where, ΔT_f = depression in freezing point,

T_{water} = thermodynamic freezing point of water = 0^{o}C,

T_{soln} = freezing point of solution, K_f = freezing point depression constant (=1.86 deg C-kg/mol for water) and

m = molality of solution. For example, the freezing point for a 1molal LiCl solution would be -3.72^{o}C (since there are 2 molal of ions from Li^+ and Cl^- ions).

Expanding on this property, it should be possible to use concentrated aqueous solutions to depress the freezing point even further so that aqueous electrolytes can be cycled at temperatures much below 0^{o}C.

In this chapter, we report the low temperature performance of three low-cost and commonly used aqueous electrolytes: LiCl, Li_2SO_4 and $LiNO_3$. We show that it is possible

to cycle conventional cathodes (in our exemplary studies[34] – LCO) in saturated solutions of such electrolytes at temperatures as low as -45°C. The system was studied from the perspective of the electrode as well as the electrolyte to understand the rate-limiting step in low temperature performance. These results were compared to the performance of organic electrolytes at similar temperatures. Finally, the effect of solution pH on the performance of electrodes was also studied at low temperatures. We expect the results of our study to be universally applicable to many other electrode chemistries and to other aqueous alkali metal ion batteries, including Na-ion and K-ion batteries, to name a few.

4.4. Experimental section

The details of the beaker cell setup is explained in the previous paper on LCO[34]. Lithium cobalt oxide (Sigma-Aldrich) was mixed with pure black as the conductive additive and PVDF as the binder in the ratio 0.7: 0.15: 0.15 and cast on titanium foil. A similar setup as before, with a symmetric cell of $LiCoO_2$ - $Li_{0.75}CoO_2$ and a GF/B grade Whatman Glass microfiber as a separator was used to study the temperature effect. A Tenney Chamber was used to accurately control the temperature of the cells from 0^{o}C down to -45^{o}C.

SEM images were taken on a Hitachi SU8230 electron microscope at an operating voltage of 2 kV. XRD measurements were taken on a Panalytical X'Pert Pro Alpha-1 instrument. A Cu K-α source was used at an accelerating voltage of 45 kV and a current of 40 mA.

For the organic cells, LCO (along with PB and PVDF, 70%:15%:15%) was cast on an aluminum foil. The symmetric cell was constructed in an in-house lab setup that could be dismantled and re-assembled (similar to a Swagelock 3E cell).

***Electrochemical measurements**:* Constant current charge-discharge experiments were performed using a 25% delithiated counter electrode, which also served as the reference electrode in the setup (the counter electrode was delithiated separately by 25% of its total capacity by mass, using a constant current and a titanium foil counter electrode). The WE was cycled between +0.1 V to 0.2 V vs. the CE. These tests were conducted using an Arbin Testing System (Arbin Instruments, USA).

For the organic cells, half cells of LCO were used for capacity measurements. The cells used the same glass fiber separator used in aqueous electrolytes to maintain uniformity in the setup. These cells were cycled at room temperature for 3 cycles at a 0.05C-rate to ensure a good formation of SEI. The cells were then charged at a 0.05C-rate and discharged at a 0.2C-rate to allow for better charging at lower temperatures.

EIS measurements were taken at different temperatures using symmetric cells for both aqueous and organic electrolytes. In both cases, the symmetric cells were cycled 15 times before measuring impedance. In the case of organic cells, the larger CE was delithiated using a Li foil before cycling against the WE. EIS measurements were taken using the Gamry Reference 600 Potentiostat between 1Mz to 0.01Hz. EIS models were fit using the Simplex method in the Gamry Echem Analyst software. The AutoFit function was used with 300 allowed iterations. The goodness of fit was usually in the order of 10^{-4} to 10^{-6} showing the model to be an accurate fit for all data points.

EIS measurements for the electrolyte conductivity measurements were taken between two 1 cm^2 titanium flags separated by different known distances (1.1 cm, 2.1 cm, 4 cm and 5.2 cm) using the Gamry Potentiostat. The impedance measurements were taken between 1MHz to 0.5Hz.

4.5. Results and discussion

In the previous chapter and in a published manuscript, we had reported the stable performance of LCO for over 1,000 cycles in saturated electrolytes[34]. This chapter, therefore, draws from our previous work and focuses on studying the performance of LCO in aqueous salt solutions at lower temperatures. In order to minimize the impact of the counter electrode on the electrochemical behavior of LCO, we use a symmetric cell setup, where both electrodes comprised LCO.

Figure 30 shows the SEM micrographs showing morphology and size of the LCO particles and the cast electrodes, as well as the XRD of LCO used in this study. The LCO particles are in the micron-size range with a particle diameter in the range of 5-20 micron. The electrodes were prepared by casting this LCO powder on a titanium foil along with pure black carbon conductive additive and a PVDF binder (in the weight ratio of 0.7: 0.15: 0.15).

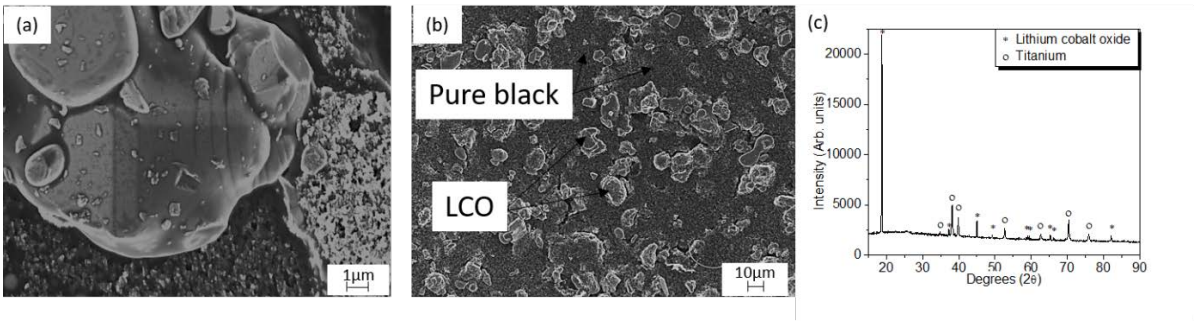

Figure 30: (a), (b) SEM of micron sized LCO and pure black used in symmetric cells, (c) XRD confirming LCO peaks

To understand the low temperature performance of this material, a symmetric cell using an LCO working electrode (WE) $LiCoO_2$ was paired with a larger partially delithiated LCO counter electrode (CE) $Li_{0.75}CoO_2$. Note that the CE had 8-10 times higher mass loading to ensure a nearly fixed potential for the CE while cycling the WE. The cycling performance of this system was analyzed in different saturated electrolytes.

The performance of LCO in Li_2SO_4 and $LiNO_3$ electrolytes and the effect of concentration have been studied in detail in the previous section at room temperature. Here we introduce a new salt, lithium chloride (LiCl), since it has a higher solubility in water at room temperature than Li_2SO_4 and $LiNO_3$. As colligative properties are dependent on the molality of the solution, a higher concentration solute could provide a larger freezing point depression.

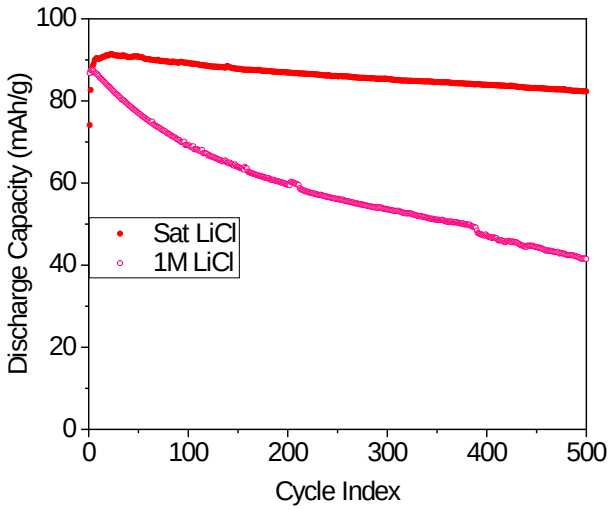

Figure 31: Discharge-capacity plots for LCO in saturated and 1M LiCl electrolyte. A similar trend is seen as with Li_2SO_4 with higher salt concentrations increasing LCO stability

Figure 31 illustrates the cycling behavior of LCO over 500 cycles in aqueous LiCl electrolyte at the high (sat LiCl ~16m at RT) and low (1M) concentrations. A similar trend is seen for LCO cycling in LiCl as with Li_2SO_4 and $LiNO_3$ electrolytes investigated in the previous section. Higher salt concentration increased the cycling stability of LCO. With the added advantage of high solubility of LiCl in water, saturated LiCl was used as an additional electrolyte to test for the depression of freezing point possible.

Figure 32 shows the constant current charge-discharge (CD) performance of LCO WE at 0.2C-rate (for both charge and discharge) in the three saturated electrolytes (LiCl, Li_2SO_4 and $LiNO_3$) at different temperatures. Saturated aqueous electrolytes, by nature of the high concentration of solute species, can support the performance of LCO down to temperatures as low as -30°C to -45°C. The degree of freezing point depression is highly dependent on the electrolyte species as well as its concentration. Saturated LiCl (~16m concentration at RT), for example, does not freeze down to -45°C or -50°C. LCO cycled in this electrolyte retained up to 72% of the room temperature capacity even at -40°C. On the other hand, saturated $LiNO_3$ (~9m at RT) freezes somewhere between -20°C to -30°C and saturated Li_2SO_4 (~3.5m at RT) between -30°C to -35°C. Clearly, a larger concentration of solute particles (cations + anions) in solution can provide a larger decrease in the freezing point of the solution (more on this later) and support better rate performance of intercalation cathodes.

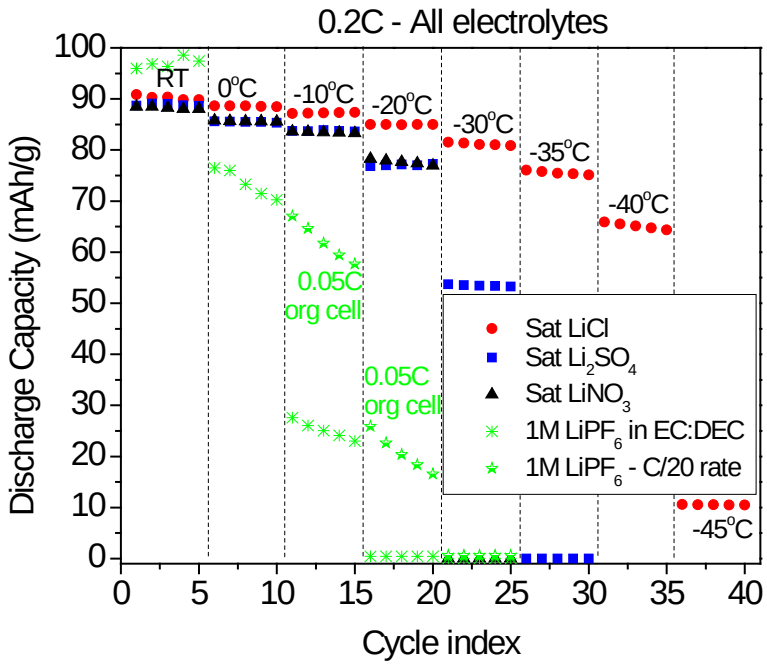

Figure 32: Cycling of LCO at 0.2C rate in sat. LiCl, sat. $LiNO_3$ & sat. Li_2SO_4 at different temperatures. In the case of LiCl electrolyte, LCO retains nearly 72% of its room temperature capacity down to -40°C. At or near the freezing temperature of the electrolyte a drastic loss in capacity is seen in all electrolytes. The performance of LCO organic electrolyte has also been shown for comparison.

As a comparison, the charge-discharge performance of the identical LCO WE in cells with organic electrolyte is also shown at 0.2C-rate. A half-cell of LCO with 1M $LiPF_6$ in 1:1 EC:DEC (standard simple commercial electrolyte from Sigma-Aldrich) was used in this study. Interestingly, these cells showed a much larger drop in capacity even at -10°C when discharged at 0.2C. The cells were also cycled at a 0.05C (C/20) rate at lower temperatures and were able to demonstrate some (although a very low) capacity at -20°C.

Several papers have reported on the low temperature performance of LCO, where the cells retain a large percentage of their room temperature discharge capacity even at sub-zero temperatures[66,68–71,73,76,146–148]. But it is important to note that in these papers the cells were always charged at room temperature and only discharged at the lower temperatures[74,146]. In almost all cases, only a single discharge cycle is depicted at a particular low temperature, to illustrate the material performance.

The reason for such a strange CD protocol previously utilized is that LCO (and other electrodes of similar structure) in organic electrolytes has a much larger charge-transfer resistance for charging than for discharging, particularly at low temperatures[146,147,150]. In other words, cells with organic electrolytes are much harder to charge at lower temperatures than to discharge. These papers also only report the discharge capacity of the cell for a single cycle since otherwise the cells would have to be charged once again at room temperature. Zhang et al.[20,29] have also reported that only a very small fraction of the room temperature capacity (10-12%) could be attained when the cells were charged and discharged at -20°C. But nearly 94% of the room temperature discharge capacity was attained when the cell was charged at room temperature and then discharged at lower temperatures. In several cases, the discharge capacity was also reported at slower 0.067C- to 0.05C-rates (C/15 to C/20) to compensate for slow low temperature discharge kinetics[66,148].

It is thus well established that the lower limits of charge-discharge for most cathodes in organic electrolytes is closer to -10°C or -20°C [72,146]. In our studies, organic LCO cells were charged at a much slower 0.05C-rate while the discharge capacity was recorded at a 0.2C-rate. At a 0.2C-rate the cells were unable to show measurable capacity below -

10°C. When the discharge current density was reduced to 0.05C, the cells retained some capacity at -20°C, but dropped to zero at -30°C.

Quite remarkably, aqueous electrolytes do not face such an issue at low temperatures. All cells with aqueous electrolytes were charged at the same C-rate as discharge. Aqueous electrolytes have a much lower R_{ct} (discussed in the following paragraphs) and hence are inherently better candidates for many low temperature applications of lithium-ion batteries.

Figure 33 compares the performance of LCO at different temperatures recorded at different C-rates in all three aqueous electrolytes. Three C-rates were used in this study: a high C-rate at 1C, a medium at 0.5C and a lower C-rate at 0.2C. The current density of cycling plays an important role in the performance of the cells. As can be seen in all cases, there is a significant difference in the performance of LCO at 1C compared to 0.2C, especially at lower temperatures. As expected, the drop in capacity with lowering temperature is larger at higher C-rates. LCO in sat. Li_2SO_4, for example, shows very low capacity at -30°C at 1C, whereas at 0.2C, it is still retains a large fraction of its room temperature capacity. Beyond -35^{o}C though, the Li_2SO_4 freezes over and can no longer sustain any performance. Clearly, unlike organic electrolytes, the aqueous electrolytes can thus demonstrate some meaningful LCO capacity up to the freezing point of the electrolyte.

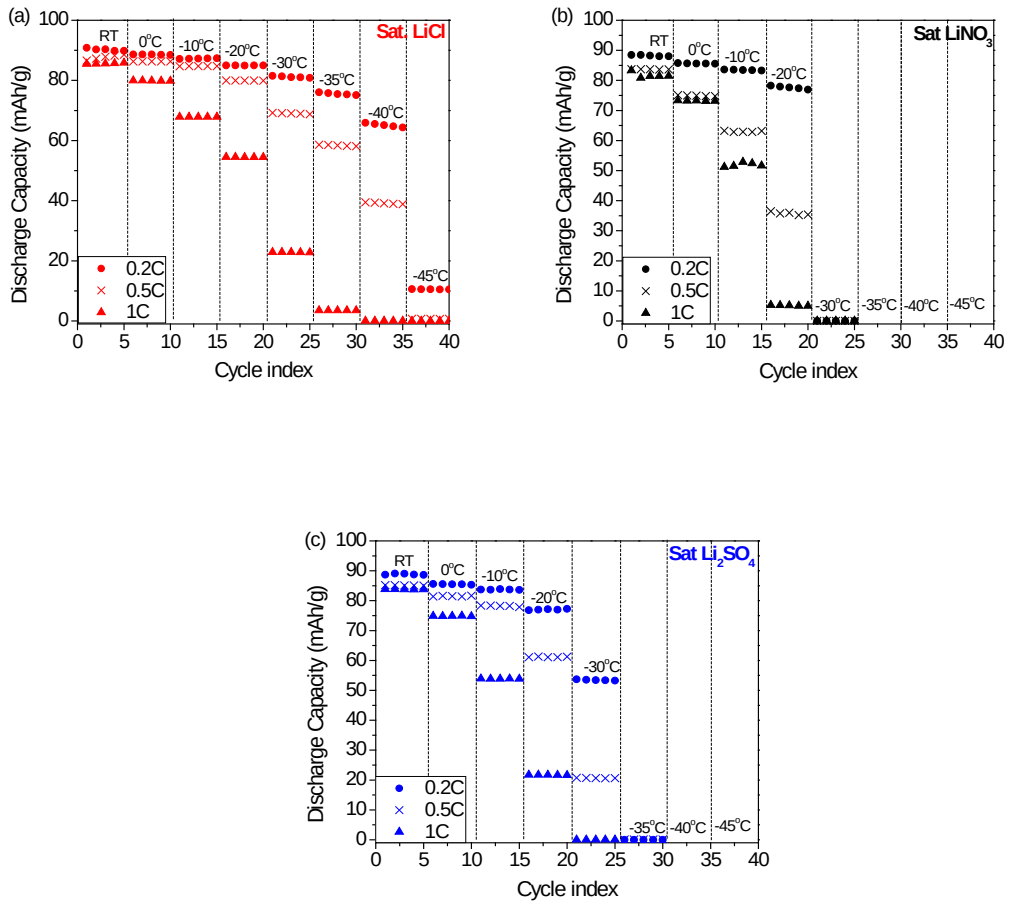

Figure 33: Cycling of LCO at different C-rates [0.2C, 0.5C and 1C] in (a) Sat. LiCl (b) Sat. $LiNO_3$ & (c) Sat. Li_2SO_4

The voltage-capacity plots for LCO cycled in sat. LiCl at 0.2C-rate were compared at different temperatures (Figure 34a). With a decrease in temperature, there is a significant increase in the polarization of the electrode material, as evidenced by the increase in the voltage hysteresis between the charge-discharge curves and the corresponding decrease in electrode capacity. The voltage hysteresis at each temperature was calculated as the difference in potential between the charge and discharge curves at half the capacity obtained at that temperature [shown by a double-sided arrow in Figure 34a]. These values

are plotted against the temperature in Figure 34b. It can be seen that there is a significant increase in the polarization of the cells closer to the freezing point of the electrolyte.

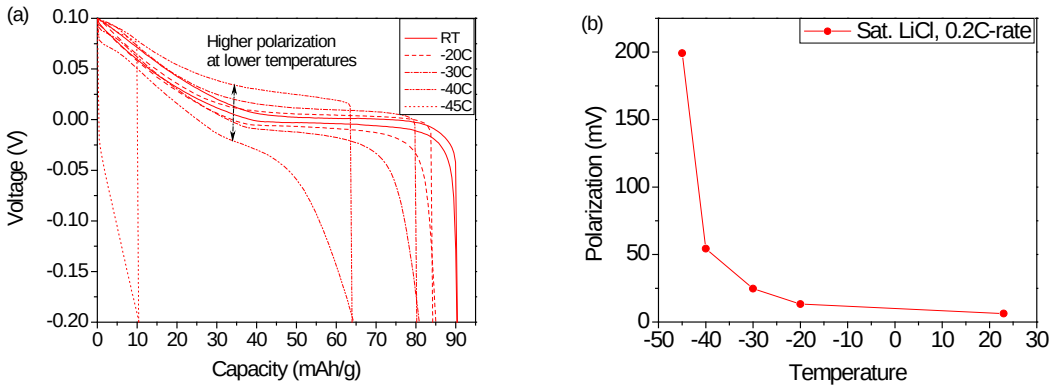

Figure 34: (a) Voltage capacity plots for a symmetric cell of LCO in sat. LiCl at different temperatures. An increase in polarization is seen as the temperature is lowered, (b) Extent of polarization plotted as a function of temperature (oC). The polarization is calculated as the difference in the charge and discharge potentials at half the maximum capacity obtained at that temperature [double-sided arrow shown in (a)]

To understand the origin of this polarization (voltage hysteresis), the impedances of LCO symmetric cells were measured at these temperatures. Figure 35 shows the EIS measurements for LCO in sat. LiCl and sat. Li_2SO_4 at all temperatures. These cells were cycled for 15 cycles at 0.2C before measuring impedance to get a better understanding of the performance of a cycled cell rather than of the fresh electrodes. In all cases, with a decrease in temperature, the EIS measurements show a large increase in the diameter of the semi-circle. This semi-circle reflects the value of the charge transfer resistance (R_{ct}) and is visible at the lower frequencies of the EIS measurements.

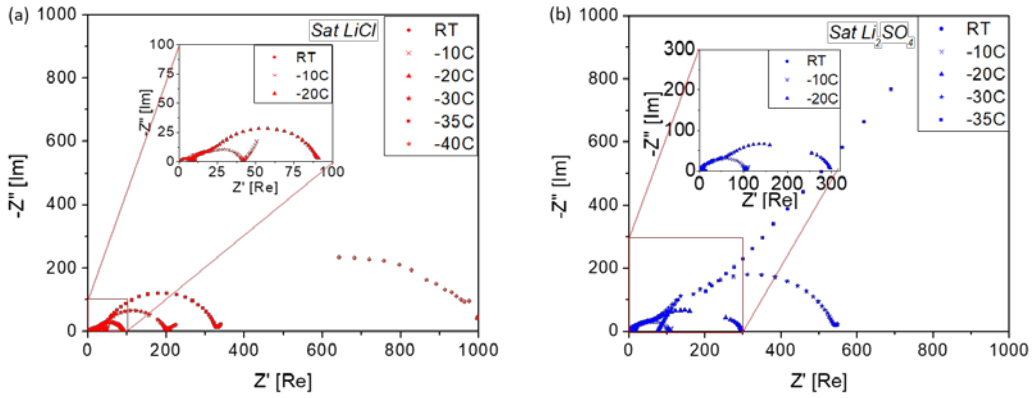

Figure 35: EIS data for a symmetric LCO cell in (a) Sat. LiCl and (b) Sat Li_2SO_4. The diameter of the semi-circle increases with decreasing temperature. Below the freezing point (around -35°C for sat Li_2SO_4), the diameter of the semicircle increases by almost an order of magnitude (incomplete semi-circle shown in picture to accommodate data)

Figure 36 compares the EIS measurements for LCO in all three electrolytes at room temperature (23°C), -20°C, -30°C and -40°C. The EIS for symmetric LCO cells with organic electrolyte (1M $LiPF_6$ in 1:1 EC:DEC electrolyte) is also shown for comparison. These symmetric cells were also cycled for 15 cycles before the EIS measurements were taken. One interesting feature is the appearance of a second semi-circle in the Nyquist plots at lower temperatures. This smaller semi-circle at the higher frequencies can be attributed to the surface layer of cobalt oxide on the LCO particles in aqueous electrolytes (see Ramanujapuram et al.[34] for more details). This surface layer is very thin (less than a few nm in size) and does not contribute much to the impedance at room temperature (the capacitance and resistance of this layer is so small it is practically buried in the larger semicircle at room temperature). But as the temperature is lowered, its effect is more pronounced, and a new smaller semi-circle appears in all the cases.

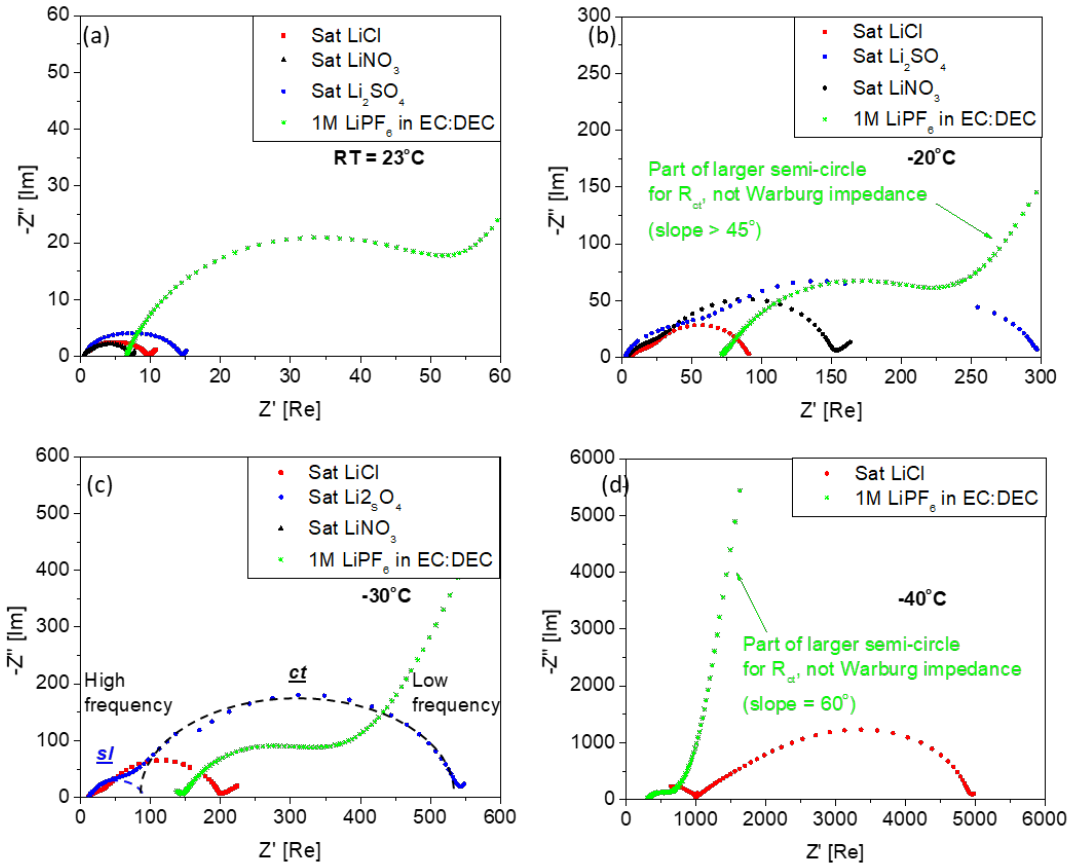

Figure 36: Comparison of EIS data at (a) RT (b) -20°C (c) -30°C and (d) -40°C for LCO symmetric cells in sat. LiCl, sat. $LiNO_3$, sat. Li_2SO_4 and 1M $LiPF_6$ in 1:1 EC:DEC. Figure (c) has an inset showing the surface layer and the charge transfer resistance components

When we compare performance of cells with organic and aqueous electrolytes we see that even at room temperature the bulk electrolyte resistance is substantially larger for cells with the organic electrolyte than that for all the aqueous cells. As the temperature is decreased, the electrolyte and surface layer resistances increase further. The largest difference can be seen in the values of $R_{ct,}$ which show orders of magnitude difference at

different temperatures. The increase in R_{ct} is more drastic in the case of the cells with organic electrolytes, which is why we see a dramatic decrease in performance below -10°C.

Figure 37 compares the different components of resistance in the system for the cells with aqueous and organic electrolytes. Figure 37a shows the EIS model used to fit the data. Figure 37b-d compare the electrolyte, surface layer and charge transfer resistances at all temperatures. In the case of aqueous electrolytes, with sat. LiCl as an example, this increase is less dramatic down to -35°C. At -40°C we see sharp rise in all three resistances as the sat. LiCl nears its freezing point. When the electrolyte freezes completely, the R_{ct} value increases by several orders of magnitude since the frozen electrolyte now behaves as a dielectric material. This increase in bulk electrolyte resistance correlates well with the drop in the performance of the LCO seen in different electrolytes. Clearly, the largest increase is seen in the charge-transfer resistance as the temperature is decreased. In comparison, the increase in electrolyte resistance is less significant.

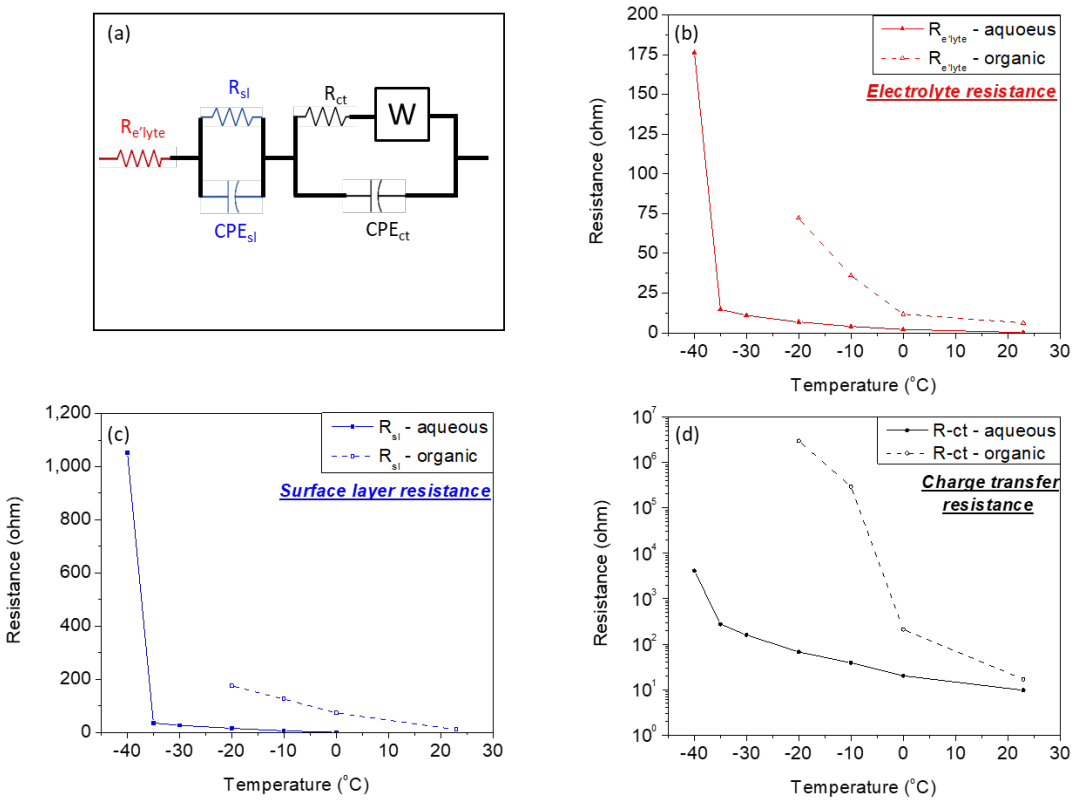

Figure 37: (a) Equivalent circuit used to model the aqueous LCO system (b), (c), (d) Comparison of resistances from electrolyte, surface layer and charge transfer as a function of temperature for the aqueous and organic electrolyte systems

The role of the bulk electrolyte resistance was also extensively studied through EIS. For each electrolyte, at a particular temperature, the resistivity was measured as a function of distance between two titanium flags of 1 cm^2 area each. EIS measurements for the electrolyte were taken at various distances as shown in Figure 38a (in this particular example for sat. LiCl at -10°C).

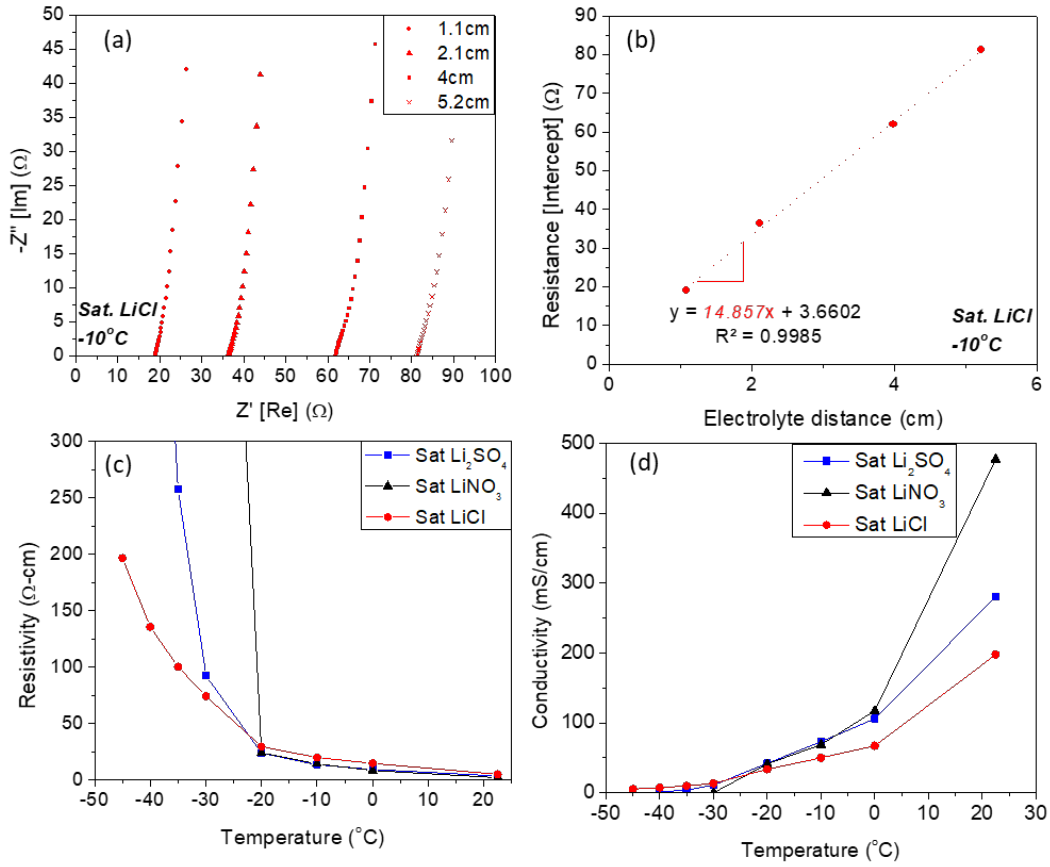

Figure 38: (a) EIS data for Sat LiCl electrolyte at -10°C between two Ti flags of 1 cm² at different distances (b) Graph of the intercept obtained in (a) vs. distance. The slope of the fitted line was used as the d.c. resistivity (Ω-cm) of the electrolyte (c) Resistivity vs. temperature data for all three electrolytes (d) Conductivity of the electrolyte as a function of temperature. As seen, there is a decrease in electrolyte conductivity with decreasing temperature. The conductivity is almost zero at and below the freezing point of each electrolyte

The intercept of the impedance curve with the x-axis can be considered as the sum of the bulk resistance from the electrolyte as well as the electrical resistance of the wires and

other external components. To eliminate all external resistances, the x-intercept of impedance was plotted as a function of the distance as shown in Figure 38b. The slope of this line then provides the resistivity of the electrolyte per unit length, which was plotted as a function of temperature as shown in Figure 38c. Such a test was then repeated for each electrolyte at each temperature. This process ensured all external resistances were discarded and a value of impedance, attributable purely to the electrolyte resistance, was obtained. The high regression (R^2) values close to 1 for all the slopes indicate the high degree of accuracy for these measurements.

The specific conductance of the electrolyte (Figure 38d) was then calculated as the inverse of this specific resistance (since the flags had an area of 1 cm^2 and the resistance is per unit length). Aqueous electrolytes thus have a conductance of the order of 10^{-1} S/cm, which is two to three orders of magnitude higher than for organic electrolytes at similar tempratures[69,146].

A sharp increase in the resistance of the electrolyte can be seen near its freezing point. Once frozen, the impedance value was very high and this was used as an independent indication that the solution had frozen completely (resistance values were out of the scale and not shown on the EIS plots). The Nyquist plots below freezing also did not show an intercept at y=0 as it occurred at a higher frequency than the instrument's capability.

The very low ionic conductivity values for frozen and near-frozen electrolytes correlate well with the drop in performance of LCO at such temperatures. For example, sat. $LiNO_3$ freezes at -30°C and shows no capacity for LCO at this temperature. Similarly, saturated Li_2SO_4 freezes around -35°C. Interestingly, saturated LiCl is still not completely frozen

even at -45°C (measurable resistance value in figure 7(c)) and correspondingly does show some performance for LCO at 0.2C-rate as seen in figure 2.

This drop in cell performance at lower temperatures may be related to: (i) the reduced mobility of the lithium ions in the solution and, at the same time, to (ii) the reduced concentration of lithium ions as well as (iii) the formation of salt precipitates from these saturated electrolytes that exhibit lower solubility at lower temperatures. Such precipitates may block electrolyte access to active particles. The drop in bulk electrolyte conductivity may also be related to all three phenomena because some precipitates may form on the surface of the titanium flags.

If we applied the depression in freezing point formula directly (which is only applicable to dilute solutions where the Raoult's law holds true), the saturated $LiNO_3$ should be expected to freeze at much lower temperatures than seen in our data. Theoretically, sat. $LiNO_3$ starts off at a concentration of ~9 molal at room temperature, which from the formula, should depress the freezing point down to -33°C. But, with a decrease in temperature, the saturation limit for $LiNO_3$ in water is also reduced. This resulted in the precipitation of excess salt. The precipitation reduced the molality of the salt solution, which in turn reduces its freezing point. Therefore sat. $LiNO_3$ completely freezes between -20°C and -30°C. Overall, the increase in electrolyte resistance is the largest close to the freezing point of the electrolyte, wherein the LCO completely loses its capacity even at low C-rates.

The effect of pH on the low temperature performance of LCO was also investigated. Sat. LiCl was used as a candidate electrolyte whose pH was reduced using HCl and increased with LiOH. Sat. LiCl has a native pH of 4.92. This was decreased to a pH of 1 and

increased to pH 14. It was found that in the highly basic solution, the LCO showed no capacity at all. Upon dismantling the cell, a brown precipitate of cobalt (III) hydroxide was observed on the separator. The Pourbaix diagram for Co shows that formation of $Co(OH)_3$ is stable at high pH when a high voltage is applied. The basic pH was thus not investigated further. LCO was also cycled in sat LiCl at a pH of 1 and its performance and EIS characteristics were studied as before, shown in Figure 39. It was found that the pH-adjusted solution showed worse performance for LCO than the plain solution of sat. LiCl. LCO showed no performance below -35°C in the pH 1 LiCl even at 0.2C. One of the reasons for substantially inferior performance of LCO at low pH is the reduced concentration of the LiCl salt in the high pH solution. With the addition of hydrochloric acid, a large precipitation of LiCl was seen even at room temperature. Due to the common-ion effect, the addition of the chloride ion increases its concentration beyond the solubility product of [Li]×[Cl] that leads to its precipitation. The loss of ions from the solution reduces the overall colligative property of the system.

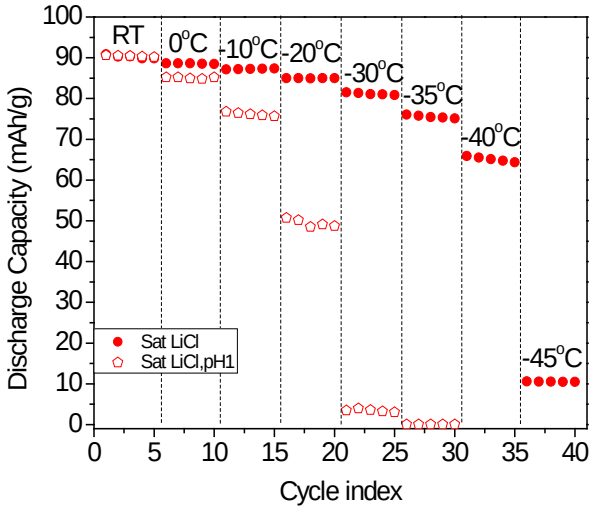

Figure 39: Cycling of LCO at 0.2C rate in sat. LiCl and sat LiCl (pH 1)

Figure 40 compares the EIS of LCO in sat. LiCl with that of the pH1 solution. The EIS results confirm the precipitation phenomenon. A higher charge transfer resistance is observed for the low pH solution compared to the pure LiCl even at the higher temperatures such as -20°C.

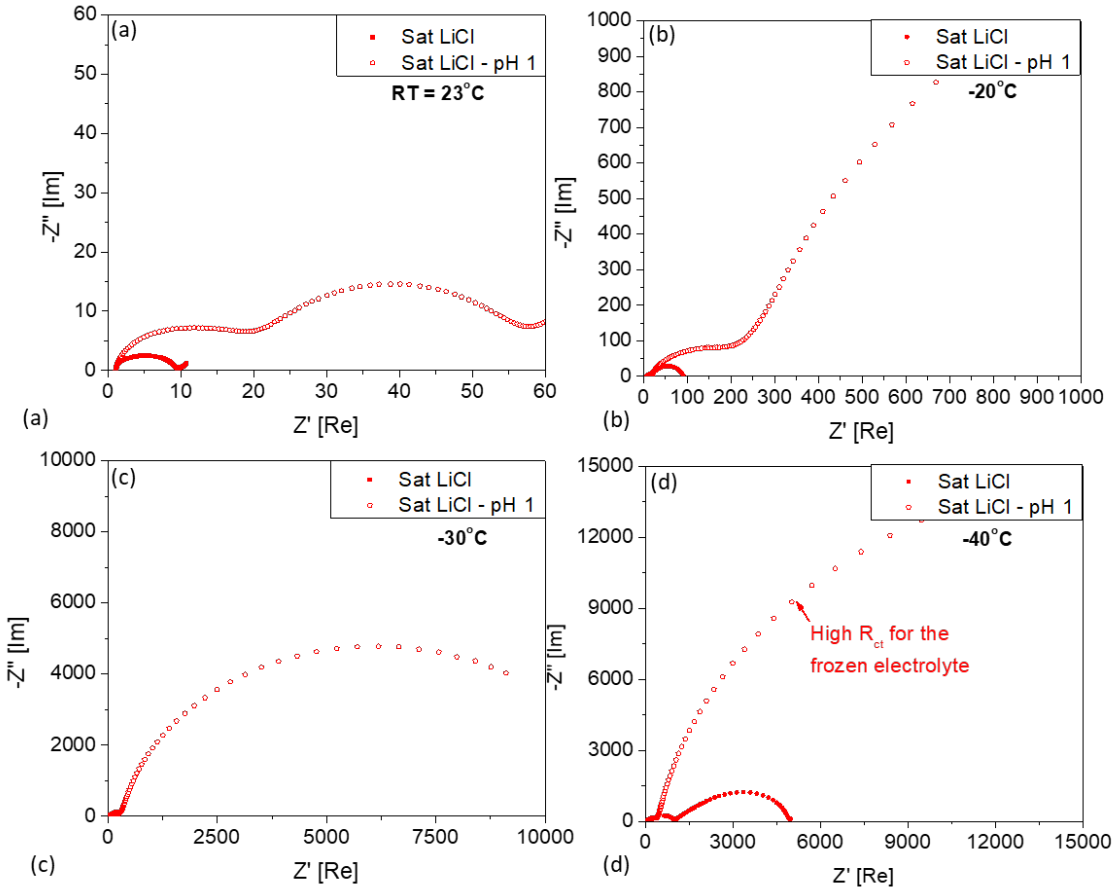

Figure 40: Comparison of EIS data at (a) RT (b) -20°C (c) -30°C and (d) -40°C for LCO symmetric cells in sat. LiCl at different pH

4.6. Conclusion

The low temperature performance of different aqueous electrolytes has been studied using a symmetric cell comprising LCO cathodes. It was shown that LCO in the saturated aqueous electrolytes can retain a significant percent of their room temperature capacity even at temperatures of -30°C to -40°C when cycled at a 0.2C rate. In the case of sat. LiCl, LCO retained nearly 72% of its room temperature capacity at -40°C and 12% at -45°C. Extensive EIS measurements were conducted to understand the effect of temperature on cell performance. It was found that both the bulk electrolyte resistance and the charge transfer resistance increased drastically when the temperature was approaching the electrolyte freezing point, which was the main cause of the reduced capacity in these cells. However, when compared to the LCO performance in traditional organic electrolytes, aqueous electrolytes showed dramatically better low temperature performance. For example, LCO cycled at a moderate 0.2C rate did not show any capacity below -20°C in organic electrolytes due to its very high charge transfer resistance during charging at low temperatures. Aqueous electrolytes on the other hand, offer lower charge transfer resistances and therefore can be charged and discharged at much higher rates at lower temperatures. In addition to low cost, improved safety and higher conductivity of aqueous electrolytes, our results demonstrate yet another unexpected advantage of aqueous lithium ion battery systems.

The effect of pH on the low temperature performance of aqueous electrolytes was also studied. It was found that LCO showed no performance in high pH (pH=14) solutions. In low pH (pH=1) solutions, the performance of LCO at lower temperatures was worse than

for pure sat. LiCl. This can be attributed to the reduced solubility and increased precipitation of LiCl due to the common ion effect.

Scope for future work

Aqueous electrolytes are an exciting new field of research that could have great potential in the future as a low-cost alternative to the lithium-ion technology. There are several exciting aspects of this research that could be explored further to advance this field. Some of these ideas include

1. Understanding the degradation mechanisms of various other intercalation cathodes and identifying similarities or differences in their degradation mechanisms compared to that of LCO
2. Understanding the effect of electrolyte pH and studying the degradation mechanisms of LCO and other cathode materials in acidic and basic solutions
3. Aqueous electrolytes could also be beneficial for cycling high voltage anodes such as lithium nickel manganese oxide (LNMO, 4.5V vs Li/Li^+) and lithium cobalt phosphate (LCP, 5.2V vs Li/Li^+). Our preliminary results showed that aqueous electrolytes do not decompose at higher potentials especially with high salt concentration solutions. These electrode materials usually decompose organic electrolytes at these high cathode potentials. Aqueous electrolytes may prove beneficial in such cases.
4. Study the effect of particle size on the performance and rate capability of LCO in aqueous electrolytes. A high rate of 1C has been used in most this research, but the effect of particle size and the thereby achievable high current rates has not been explored. Using nano-particles could prove very useful in utilizing the high C-rates that should be possible due to the higher ionic conductivity of aqueous electrolytes.

5. Study the performance of LCO at higher temperatures such as 60-80°C using similar or alternative aqueous electrolytes. The high safety achievable with aqueous electrolytes coupled with the colligative properties utilized in this research could prove to be useful at higher temperatures as well
6. The effect of additives on the temperature range of aqueous electrolytes was also not investigated in detail. Our preliminary results showed that adding an anti-freeze like propylene glycol reduced the solubility of LiCl salt and hence did not sustain as low temperatures as pure sat. LiCl. But the effect of other additives (including organic solvents and organic salts) was not explored in detail. It is possible that other additives or other electrolyte salts could allow higher concentration aqueous electrolytes (the water-in-bisalt paper could be one example) that could perform at even lower temperatures than -45°C.

List of publications authored (2013-2018)

- ***Degradation and stabilization of lithium cobalt oxide in aqueous electrolytes***

  Anirudh Ramanujapuram, Daniel Gordon, Alexandre Magasinski, Brian Ward, Naoki Nitta, Cindy Huang, Gleb Yushin

  Energy & Environmental Science 9 (5), pg 1841-1848, 2016

- ***Enhancing Cycle Stability of Lithium Iron Phosphate in Aqueous Electrolytes by Increasing Electrolyte Molarity***

  Daniel Gordon, Michelle Yu Wu, Anirudh Ramanujapuram, James Benson, Jung Tae Lee, Alexandre Magasinski, Naoki Nitta, Cindy Huang, Gleb Yushin

  Advanced Energy Materials 6 (2), pg 1501805, 2016

- ***Toward in-situ protected sulfur cathodes by using lithium bromide and pre-charge***

  Feixiang Wu, Sören Thieme, Anirudh Ramanujapuram, Enbo Zhao, Christine Weller, Holger Althues, Stefan Kaskel, Oleg Borodin, Gleb Yushin

  Nano Energy 40 (6), pg 170-179, 2017

- ***Influence of Protons on the Lithium Transport Mechanism in Antiperovskite Solid Electrolytes from Molecular Dynamics Simulations***

  Oleg Borodin, Marco Olguin, Ah-Young Song, Yiran Xiao, Kostiantyn Turcheniuk, Anirudh Ramanujapuram, Jim Benson, Alexandre Magasinski, Lamartine Meda, Gleb Yushin

  The Electrochemical Society, Meeting Abstracts 4, pg 410, 2017

- ***Mixed Metal Difluorides as High Capacity Conversion-Type Cathodes: Impact of Composition on Stability and Performance***

  Daniel Gordon, Qiao Huang, Alexandre Magasinski, Anirudh Ramanujapuram, Nasr Bensalah, Gleb Yushin

Advanced Energy Materials, 2018 (Online Version of Record before inclusion in an issue 1800213 doi: 10.1002/aenm.201800213)

- ***Protons Enhance Conductivities in Lithium Halide Hydroxide/Lithium Oxyhalide Solid Electrolytes by Forming Rotating Hydroxy Groups***

  Ah-Young Song, Yiran Xiao, Kostiantyn Turcheniuk, Punith Upadhya, Anirudh Ramanujapuram, Jim Benson, Alexandre Magasinski, Marco Olguin, Lamartine Meda, Oleg Borodin, Gleb Yushin

  Advanced Energy Materials 8 (3), pg. 1700971, 2018

- ***Understanding the Exceptional Performance of Lithium-ion Battery Cathodes in Aqueous Electrolytes at Sub-Zero Temperatures***

  Anirudh Ramanujapuram, Gleb Yushin

  Submitted, In review, 2018

References

1. http://www.marketresearch.com/product/sample-8323376.pdf.
2. http://www.rechargebatteries.org/wp-content/uploads/2015/01/Avicenne-market-review-Nive-2014.pdf.
3. Fergus, J. W. Recent developments in cathode materials for lithium ion batteries. *J. Power Sources* **195,** 939–954 (2010).
4. Whittingham, M. S. Lithium Batteries and Cathode Materials. *Chem. Rev.* **104,** 4271–4302 (2004).
5. Yuan, L.-X. *et al.* Development and challenges of LiFePO 4 cathode material for lithium-ion batteries. *Energy Environ. Sci.* **4,** 269–284 (2011).
6. Whittingham, M. S. Electrical Energy Storage and Intercalation Chemistry. *Science* **192,** 1126–1127 (1976).
7. Jansen, A. N. *et al.* Development of a high-power lithium-ion battery. *J. Power Sources* **81–82,** 902–905 (1999).
8. Cheng, Y. *et al.* Facile Synthesis of Chevrel Phase Nanocubes and Their Applications for Multivalent Energy Storage. *Chem. Mater.* **26,** 4904–4907 (2014).
9. Lithium insertion in different TiO2 modifications - ScienceDirect. Available at: https://www.sciencedirect.com/science/article/pii/0167273888903529. (Accessed: 8th March 2018)
10. Nitta, N. & Yushin, G. High-Capacity Anode Materials for Lithium-Ion Batteries: Choice of Elements and Structures for Active Particles. *Part. Part. Syst. Charact.* **31,** 317–336 (2014).
11. Croguennec, L. & Palacin, M. R. Recent Achievements on Inorganic Electrode Materials for Lithium-Ion Batteries. *J. Am. Chem. Soc.* **137,** 3140–3156 (2015).
12. Dahn, J. R., Fuller, E. W., Obrovac, M. & von Sacken, U. Thermal stability of LixCoO2, LixNiO2 and λ-MnO2 and consequences for the safety of Li-ion cells. *Solid State Ion.* **69,** 265–270 (1994).

13. Gordon, D. *et al.* Enhancing Cycle Stability of Lithium Iron Phosphate in Aqueous Electrolytes by Increasing Electrolyte Molarity. *Adv. Energy Mater.* **6,** n/a-n/a (2016).

14. http://blog.flexelbattery.com/blog/how-to-choose-the-right-battery-electrolyte-for-your-application-available-electrolyte-types-part-1.

15. Tarascon, J.-M., Gozdz, A. S., Schmutz, C., Shokoohi, F. & Warren, P. C. Performance of Bellcore's plastic rechargeable Li-ion batteries. *Solid State Ion.* **86–88,** 49–54 (1996).

16. *Handbook of electrochemistry*. (Elsevier, 2007).

17. Li, W. & Dahn, J. R. Lithium-Ion Cells with Aqueous Electrolytes. *J. Electrochem. Soc.* **142,** 1742–1746 (1995).

18. An Aqueous Rechargeable Lithium Battery with Good Cycling Performance - Wang - 2006 - Angewandte Chemie - Wiley Online Library. Available at: http://onlinelibrary.wiley.com/doi/10.1002/ange.200603699/full. (Accessed: 8th March 2018)

19. Wang, G. J. *et al.* Characteristics of an aqueous rechargeable lithium battery (ARLB). *Electrochimica Acta* **52,** 4911–4915 (2007).

20. Wang, Y., Yi, J. & Xia, Y. Recent Progress in Aqueous Lithium-Ion Batteries. *Adv. Energy Mater.* **2,** 830–840 (2012).

21. Wang, X., Hou, Y., Zhu, Y., Wu, Y. & Holze, R. An Aqueous Rechargeable Lithium Battery Using Coated Li Metal as Anode. *Sci. Rep.* **3,** 1401 (2013).

22. Suo, L. *et al.* "Water-in-salt" electrolyte enables high-voltage aqueous lithium-ion chemistries. *Science* **350,** 938–943 (2015).

23. Wang, F. *et al.* Stabilizing high voltage LiCoO 2 cathode in aqueous electrolyte with interphase-forming additive. *Energy Environ. Sci.* **9,** 3666–3673 (2016).

24. Suo, L. *et al.* Advanced High-Voltage Aqueous Lithium-Ion Battery Enabled by "Water-in-Bisalt" Electrolyte. *Angew. Chem. Int. Ed.* **55,** 7136–7141 (2016).

25. Yang, C. *et al.* 4.0 V Aqueous Li-Ion Batteries. *Joule* **1,** 122–132 (2017).

26. Tang, W. *et al.* Nano-LiCoO2 as cathode material of large capacity and high rate capability for aqueous rechargeable lithium batteries. *Electrochem. Commun.* **12,** 1524–1526 (2010).

27. Tian, S. *et al.* IMPROVING ELECTROCHEMICAL PERFORMANCE OF LiCoO2 BY TiO2 COATING AS CATHODE FOR AQUEOUS RECHARGEABLE LITHIUM BATTERIES. *Funct. Mater. Lett.* **06,** 1350016 (2013).

28. Qu, Q. *et al.* Porous LiMn 2 O 4 as cathode material with high power and excellent cycling for aqueous rechargeable lithium batteries. *Energy Environ. Sci.* **4,** 3985–3990 (2011).

29. Luo, J.-Y., Cui, W.-J., He, P. & Xia, Y.-Y. Raising the cycling stability of aqueous lithium-ion batteries by eliminating oxygen in the electrolyte. *Nat. Chem.* **2,** 760–765 (2010).

30. Gu, W. & Yushin, G. Review of nanostructured carbon materials for electrochemical capacitor applications: advantages and limitations of activated carbon, carbide-derived carbon, zeolite-templated carbon, carbon aerogels, carbon nanotubes, onion-like carbon, and graphene. *Wiley Interdiscip. Rev. Energy Environ.* **3,** 424–473 (2014).

31. Goodenough, J. B. & Park, K.-S. The Li-Ion Rechargeable Battery: A Perspective. *J. Am. Chem. Soc.* **135,** 1167–1176 (2013).

32. Tron, A., Jo, Y. N., Oh, S. H., Park, Y. D. & Mun, J. Surface Modification of the LiFePO4 Cathode for the Aqueous Rechargeable Lithium Ion Battery. *ACS Appl. Mater. Interfaces* **9,** 12391–12399 (2017).

33. Ruffo, R., Wessells, C., Huggins, R. A. & Cui, Y. Electrochemical behavior of LiCoO2 as aqueous lithium-ion battery electrodes. *Electrochem. Commun.* **11,** 247–249 (2009).

34. Ramanujapuram, A. *et al.* Degradation and stabilization of lithium cobalt oxide in aqueous electrolytes. *Energy Environ. Sci.* **9,** 1841–1848 (2016).

35. Ruffo, R., La Mantia, F., Wessells, C., Huggins, R. A. & Cui, Y. Electrochemical characterization of LiCoO2 as rechargeable electrode in aqueous LiNO3 electrolyte. *Solid State Ion.* **192,** 289–292 (2011).

36. Liu, S., Ye, S. H., Li, C. Z., Pan, G. L. & Gao, X. P. Rechargeable Aqueous Lithium-Ion Battery of TiO2/LiMn2O4 with a High Voltage. *J. Electrochem. Soc.* **158,** A1490–A1497 (2011).

37. Li, W., McKinnon, W. R. & Dahn, J. R. Lithium Intercalation from Aqueous Solutions. *J. Electrochem. Soc.* **141,** 2310–2316 (1994).

38. Zhang, S., Li, Y., Wu, C., Zheng, F. & Xie, Y. Novel Flowerlike Metastable Vanadium Dioxide (B) Micronanostructures: Facile Synthesis and Application in Aqueous Lithium Ion Batteries. *J. Phys. Chem. C* **113,** 15058–15067 (2009).

39. He, Z. *et al.* Boosting the performance of LiTi2(PO4)3/C anode for aqueous lithium ion battery by Sn doping on Ti sites. *J. Alloys Compd.* **731,** 32–38 (2018).

40. Luo J.-Y. & Xia Y.-Y. Aqueous Lithium-ion Battery LiTi2(PO4)3/LiMn2O4 with High Power and Energy Densities as well as Superior Cycling Stability**. *Adv. Funct. Mater.* **17,** 3877–3884 (2007).

41. Wang, H. *et al.* Rational design and synthesis of LiTi 2 (PO 4) 3−x F x anode materials for high-performance aqueous lithium ion batteries. *J. Mater. Chem. A* **5,** 593–599 (2017).

42. Wu, W. *et al.* High Performance TiP2O7 Based Intercalation Negative Electrode for Aqueous Lithium-Ion Batteries via a Facile Synthetic Route. *J. Electrochem. Soc.* **162,** A1921–A1926 (2015).

43. Wang, H., Huang, K., Zeng, Y., Yang, S. & Chen, L. Electrochemical properties of TiP2O7 and LiTi2(PO4)3 as anode material for lithium ion battery with aqueous solution electrolyte. *Electrochimica Acta* **52,** 3280–3285 (2007).

44. Crompton, T. R. *Battery reference book*. (Newnes, 2000).

45. Cheng, F. Y., Chen, J., Gou, X. L. & Shen, P. W. High-Power Alkaline Zn–MnO2 Batteries Using γ-MnO2 Nanowires/Nanotubes and Electrolytic Zinc Powder. *Adv. Mater.* **17,** 2753–2756 (2005).

46. Bode, H. Lead-acid batteries. (1977).

47. Jung, J. Lead-Acid Battery. in *Electrochemical Technologies for Energy Storage and Conversion* (eds. Liu, R.-S., Zhang, L., Sun, X., Liu, H. & Zhang, J.) 111–174 (Wiley-VCH Verlag GmbH & Co. KGaA, 2011). doi:10.1002/9783527639496.ch4

48. Blum, W. & Vinal, G. W. The Definition of Polarization, Overvoltage and Decomposition Potential. *Trans. Electrochem. Soc.* **66,** 359–367 (1934).

49. Girishkumar, G., McCloskey, B., Luntz, A. C., Swanson, S. & Wilcke, W. Lithium−Air Battery: Promise and Challenges. *J. Phys. Chem. Lett.* **1,** 2193–2203 (2010).

50. Zhang, T. *et al.* A novel high energy density rechargeable lithium /air battery. *Chem. Commun.* **46,** 1661–1663 (2010).

51. Zhang, T. & Zhou, H. A reversible long-life lithium–air battery in ambient air. *Nat. Commun.* **4,** 1817 (2013).

52. Cheng, X.-B. *et al.* A Review of Solid Electrolyte Interphases on Lithium Metal Anode. *Adv. Sci.* **3,** n/a-n/a (2016).

53. Verma, P., Maire, P. & Novák, P. A review of the features and analyses of the solid electrolyte interphase in Li-ion batteries. *Electrochimica Acta* **55,** 6332–6341 (2010).

54. Winter, M. The Solid Electrolyte Interphase – The Most Important and the Least Understood Solid Electrolyte in Rechargeable Li Batteries. *Z. Für Phys. Chem.* **223,** 1395–1406 (2009).

55. Christensen, J. & Newman, J. A Mathematical Model for the Lithium-Ion Negative Electrode Solid Electrolyte Interphase. *J. Electrochem. Soc.* **151,** A1977–A1988 (2004).

56. Aquion Energy. *Crunchbase* Available at: https://www.crunchbase.com/organization/aquion-energy. (Accessed: 21st March 2018)

57. Aluminum E-pH (Pourbaix) diagram. Available at: https://corrosion-doctors.org/Corrosion-Thermodynamics/Potential-pH-diagram-aluminum.htm. (Accessed: 9th March 2018)

58. Zhang, S. S. & Jow, T. R. Aluminum corrosion in electrolyte of Li-ion battery. *J. Power Sources* **109,** 458–464 (2002).

59. Krämer, E., Passerini, S. & Winter, M. Dependency of Aluminum Collector Corrosion in Lithium Ion Batteries on the Electrolyte Solvent. *ECS Electrochem. Lett.* **1,** C9–C11 (2012).

60. Krause, L. J. *et al.* Corrosion of aluminum at high voltages in non-aqueous electrolytes containing perfluoroalkylsulfonyl imides; new lithium salts for lithium-ion cells. *J. Power Sources* **68,** 320–325 (1997).

61. Yang, H., Kwon, K., Devine, T. M. & Evans, J. W. Aluminum Corrosion in Lithium Batteries An Investigation Using the Electrochemical Quartz Crystal Microbalance. *J. Electrochem. Soc.* **147,** 4399–4407 (2000).

62. NPTEL H2 evolution.

63. Bockris, J. O. & Srinivasan, S. Elucidation of the mechanism of electrolytic hydrogen evolution by the use of H-T separation factors. *Electrochimica Acta* **9,** 31–44 (1964).

64. Nørskov, J. K. *et al.* Trends in the Exchange Current for Hydrogen Evolution. *J. Electrochem. Soc.* **152,** J23–J26 (2005).

65. Yin, Y.-X., Xin, S., Guo, Y.-G. & Wan, L.-J. Lithium–Sulfur Batteries: Electrochemistry, Materials, and Prospects. *Angew. Chem. Int. Ed.* **52,** 13186–13200 (2013).

66. Huang, C.-K., Sakamoto, J. S., Wolfenstine, J. & Surampudi, S. The Limits of Low-Temperature Performance of Li-Ion Cells. *J. Electrochem. Soc.* **147,** 2893–2896 (2000).

67. Zhang, S. S., Xu, K. & Jow, T. R. The low temperature performance of Li-ion batteries. *J. Power Sources* **115,** 137–140 (2003).

68. Aris, A. M. & Shabani, B. An Experimental Study of a Lithium Ion Cell Operation at Low Temperature Conditions. *Energy Procedia* **110,** 128–135 (2017).

69. Chen, K. *et al.* Evaluation of the low temperature performance of lithium manganese oxide/lithium titanate lithium-ion batteries for start/stop applications. *J. Power Sources* **278,** 411–419 (2015).

70. Fan, J. On the discharge capability and its limiting factors of commercial 18650 Li-ion cell at low temperatures. *J. Power Sources* **117,** 170–178 (2003).

71. Lin, H. –. *et al.* Low-Temperature Behavior of Li-Ion Cells. *Electrochem. Solid-State Lett.* **4,** A71–A73 (2001).

72. Nobili, F., Mancini, M., Dsoke, S., Tossici, R. & Marassi, R. Low-temperature behavior of graphite–tin composite anodes for Li-ion batteries. *J. Power Sources* **195,** 7090–7097 (2010).

73. Senyshyn, A., Mühlbauer, M. J., Dolotko, O. & Ehrenberg, H. Low-temperature performance of Li-ion batteries: The behavior of lithiated graphite. *J. Power Sources* **282,** 235–240 (2015).

74. Smart, M. C. *et al.* Improved low-temperature performance of lithium-ion cells with quaternary carbonate-based electrolytes. *J. Power Sources* **119–121,** 349–358 (2003).

75. Zhang, S. S., Xu, K. & Jow, T. R. Electrochemical impedance study on the low temperature of Li-ion batteries. *Electrochimica Acta* **49,** 1057–1061 (2004).

76. Zhu, G. *et al.* Materials insights into low-temperature performances of lithium-ion batteries. *J. Power Sources* **300,** 29–40 (2015).

77. Alexandrowicz, Z. & Katchalsky, A. Colligative properties of polyelectrolyte solutions in excess of salt. *J. Polym. Sci. A* **1,** 3231–3260 (1963).

78. Andrews, F. C. Colligative Properties of Simple Solutions. *Science* **194,** 567–571 (1976).

79. Hammel, H. T. Colligative Properties of a Solution. *Science* **192,** 748–756 (1976).

80. Kissinger, P. T. & Heineman, W. R. Cyclic voltammetry. *J. Chem. Educ.* **60,** 702 (1983).

81. Nicholson, R. S. Theory and Application of Cyclic Voltammetry for Measurement of Electrode Reaction Kinetics. *Anal. Chem.* **37,** 1351–1355 (1965).

82. Heinze, J. Cyclic Voltammetry—"Electrochemical Spectroscopy". New Analytical Methods (25). *Angew. Chem. Int. Ed. Engl.* **23,** 831–847 (1984).

83. Mabbott, G. A. An introduction to cyclic voltammetry. *J. Chem. Educ.* **60,** 697 (1983).

84. Bard, A. J. & Faulkner, L. R. *Electrochemical methods: fundamentals and applications*. (Wiley, 2001).

85. Laviron, E. Adsorption, autoinhibition and autocatalysis in polarography and in linear potential sweep voltammetry. *J. Electroanal. Chem. Interfacial Electrochem.* **52,** 355–393 (1974).

86. Amatore, C. & Saveant, J. M. Ece and disproportionation: Part V. Stationary state general solution application to linear sweep voltammetry. *J. Electroanal. Chem. Interfacial Electrochem.* **85,** 27–46 (1977).

87. Laviron, E. The use of linear potential sweep voltammetry and of a.c. voltammetry for the study of the surface electrochemical reaction of strongly adsorbed systems and of redox modified electrodes. *J. Electroanal. Chem. Interfacial Electrochem.* **100,** 263–270 (1979).

88. Sharpe, T. F. Low-Rate Cathodic Linear Sweep Voltammetry (LSV) Studies on Anodized Lead. *J. Electrochem. Soc.* **122,** 845–851 (1975).

89. López-Hirata, V. M. & Arce-Estrada, E. M. Characterization of Co□Cu mechanical alloys by linear sweep voltammetry. *Electrochimica Acta* **42,** 61–65 (1997).

90. Lenglet, M., Kartouni, K. & Delahaye, D. Characterization of copper oxidation by linear potential sweep voltammetry and UV-Visible-NIR diffuse reflectance spectroscopy. *J. Appl. Electrochem.* **21,** 697–702 (1991).

91. Brett, C. M. A. On the electrochemical behaviour of aluminium in acidic chloride solution. *Corros. Sci.* **33,** 203–210 (1992).

92. Tal M. Nahir, Rose A. Clark, & Edmond F. Bowden. Linear-Sweep Voltammetry of Irreversible Electron Transfer in Surface-Confined Species Using the Marcus Theory. *Anal. Chem.* **66,** 2595–2598 (1998).

93. Chang, B.-Y. & Park, S.-M. Electrochemical Impedance Spectroscopy. *Annu. Rev. Anal. Chem.* **3,** 207–229 (2010).

94. Ivers-Tiffée E., Weber A. & Schichlein H. Electrochemical impedance spectroscopy. *Handb. Fuel Cells* (2010). doi:10.1002/9780470974001.f203019

95. Retter, U. & Lohse, H. Electrochemical Impedance Spectroscopy. in *Electroanalytical Methods* 159–177 (Springer, Berlin, Heidelberg, 2010). doi:10.1007/978-3-642-02915-8_8

96. Jüttner, K. Electrochemical impedance spectroscopy (EIS) of corrosion processes on inhomogeneous surfaces. *Electrochimica Acta* **35,** 1501–1508 (1990).

97. Rodrigues, S., Munichandraiah, N. & Shukla, A. K. AC impedance and state-of-charge analysis of a sealed lithium-ion rechargeable battery. *J. Solid State Electrochem.* **3,** 397–405 (1999).

98. Rodrigues, S., Munichandraiah, N. & Shukla, A. K. A review of state-of-charge indication of batteries by means of a.c. impedance measurements. *J. Power Sources* **87,** 12–20 (2000).

99. Jang, J. & Yoo, J. Equivalent Circuit Evaluation Method of Lithium Polymer Battery Using Bode Plot and Numerical Analysis. *IEEE Trans. Energy Convers.* **26,** 290–298 (2011).

100. Andre, D. *et al.* Characterization of high-power lithium-ion batteries by electrochemical impedance spectroscopy. I. Experimental investigation. *J. Power Sources* **196,** 5334–5341 (2011).

101. Deng, Z. *et al.* Electrochemical Impedance Spectroscopy Study of a Lithium/Sulfur Battery: Modeling and Analysis of Capacity Fading. *J. Electrochem. Soc.* **160,** A553–A558 (2013).

102. Itagaki, M. *et al.* In situ electrochemical impedance spectroscopy to investigate negative electrode of lithium-ion rechargeable batteries. *J. Power Sources* **135,** 255–261 (2004).

103. Itagaki, M. *et al.* LiCoO2 electrode/electrolyte interface of Li-ion rechargeable batteries investigated by in situ electrochemical impedance spectroscopy. *J. Power Sources* **148,** 78–84 (2005).

104. Hang, T. *et al.* Electrochemical impedance spectroscopy analysis for lithium-ion battery using Li4Ti5O12 anode. *J. Power Sources* **222,** 442–447 (2013).

105. Do, D. V., Forgez, C., Benkara, K. E. K. & Friedrich, G. Impedance Observer for a Li-Ion Battery Using Kalman Filter. *IEEE Trans. Veh. Technol.* **58,** 3930–3937 (2009).

106. Siegbahn, K. Electron spectroscopy for atoms, molecules, and condensed matter. *Rev. Mod. Phys.* **54,** 709–728 (1982).

107. Pluel, D. & Simon, F. X-Ray Photoelectron Spectroscopy. In: Stamm M. (eds) Polymer Surfaces and Interfaces. *Springer* 71–89 (2008). doi:10.1007/978-3-540-73865-7_4

108. Chusuei, C. C. & Goodman, D. W. *Encyclopedia of Physical Science and Technology*. **17,** (Academic Press, 2002).

109. Hollander, J. M. & Jolly, W. L. X-ray photoelectron spectroscopy. *Acc. Chem. Res.* **3,** 193–200 (1970).

110. *Surface science techniques*. (Pergamon, 1994).

111. Winograd, N. & Gaarenstroom, S. W. X-Ray Photoelectron Spectroscopy. in *Physical Methods in Modern Chemical Analysis* **2,** 115–169 (Academic Press).

112. XPS Instrumentation. Available at: http://www.casaxps.com/help_manual/XPSInformation/XPSInstr.htm. (Accessed: 8th March 2018)

113. *Practical Scanning Electron Microscopy*. (Springer US, 1975). doi:10.1007/978-1-4613-4422-3

114. Ludwig Reimer. *Scanning Electron Microscopy: Physics of Image Formation and Microanalysis*. **45,** (Springer US).

115. Pease, R. F. W. & Nixon, W. C. High resolution scanning electron microscopy. *J. Sci. Instrum.* **42,** 81 (1965).

116. Bogner, A., Jouneau, P.-H., Thollet, G., Basset, D. & Gauthier, C. A history of scanning electron microscopy developments: Towards “wet-STEM” imaging. *Micron* **38,** 390–401 (2007).

117. Schmolze, D. B., Standley, C., Fogarty, K. E. & Fischer, A. H. Advances in Microscopy Techniques. *Arch. Pathol. Lab. Med.* **135,** 255–263 (2011).

118. Kelly P. M., Jostsons A., Blake R. G. & Napier J. G. The determination of foil thickness by scanning transmission electron microscopy. *Phys. Status Solidi A* **31,** 771–780 (2006).

119. Williams, D. B. & Carter, C. B. The Transmission Electron Microscope. in *Transmission Electron Microscopy* 3–17 (Springer, Boston, MA, 1996). doi:10.1007/978-1-4757-2519-3_1

120. Burghardt Robert C. & Droleskey Robert. Transmission Electron Microscopy. *Curr. Protoc. Microbiol.* **3,** 2B.1.1-2B.1.39 (2006).

121. Fultz, B. & Howe, J. *Transmission Electron Microscopy and Diffractometry of Materials*. (Springer Berlin Heidelberg, 2013). doi:10.1007/978-3-642-29761-8

122. Beards, D. G. *A cross-sectional, simplified diagram of a transmission electron microscope.* (2009).

123. Shinba, Y., Konno, T. J., Ishikawa, K., Hiraga, K. & Sagawa, M. Transmission electron microscopy study on Nd-rich phase and grain boundary structure of Nd–Fe–B sintered magnets. *J. Appl. Phys.* **97,** 053504 (2005).

124. Horita, Z. *et al.* An investigation of grain boundaries in submicrometer-grained Al-Mg solid solution alloys using high-resolution electron microscopy. *J. Mater. Res.* **11,** 1880–1890 (1996).

125. Liu, Y. *et al.* In Situ Transmission Electron Microscopy Observation of Pulverization of Aluminum Nanowires and Evolution of the Thin Surface Al2O3 Layers during Lithiation–Delithiation Cycles. *Nano Lett.* **11,** 4188–4194 (2011).

126. Fallon, P. J. & Brown, L. M. Analysis of chemical-vapour-deposited diamond grain boundaries using transmission electron microscopy and parallel electron energy loss spectroscopy in a scanning transmission electron microscope. *Diam. Relat. Mater.* **2,** 1004–1011 (1993).

127. McDowell Matthew T. *et al.* Studying the Kinetics of Crystalline Silicon Nanoparticle Lithiation with In Situ Transmission Electron Microscopy. *Adv. Mater.* **24,** 6034–6041 (2012).

128. Wang, C.-M. *et al.* In Situ Transmission Electron Microscopy Observation of Microstructure and Phase Evolution in a SnO2 Nanowire during Lithium Intercalation. *Nano Lett.* **11,** 1874–1880 (2011).

129. Egerton, R. F. *Electron Energy-Loss Spectroscopy in the Electron Microscope*. (Springer US, 2011). doi:10.1007/978-1-4419-9583-4

130. Dorset, D. L. X-ray Diffraction: A Practical Approach. *Microsc. Microanal.* **4,** 513–515 (1998).

131. Moore, D. M. & Reynolds, R. C. *X-ray diffraction and the identification and analysis of clay minerals*. (Oxford University Press, 1997).

132. Snyder, R. L. X-Ray Diffraction. in *Materials Science and Technology* (eds. Cahn, R. W., Haasen, P. & Kramer, E. J.) (Wiley-VCH Verlag GmbH & Co. KGaA, 2006). doi:10.1002/9783527603978.mst0013

133. Warren, B. E. *X-ray diffraction*. (Dover Publications, 1990).

134. Zachariasen, W. H. A general theory of X-ray diffraction in crystals. *Acta Crystallogr.* **23,** 558–564 (1967).

135. Diffraction Theory. in *Introduction to X-ray Powder Diffractometry* 47–95 (John Wiley & Sons, Inc., 2012). doi:10.1002/9781118520994.ch3

136. Christensen, K. O., Chen, D., Lødeng, R. & Holmen, A. Effect of supports and Ni crystal size on carbon formation and sintering during steam methane reforming. *Appl. Catal. Gen.* **314,** 9–22 (2006).

137. Zhou, X.-D. & Huebner, W. Size-induced lattice relaxation in CeO2 nanoparticles. *Appl. Phys. Lett.* **79,** 3512–3514 (2001).

138. Li, Z. Y. *et al.* Chemical composition, crystal size and lattice structural changes after incorporation of strontium into biomimetic apatite. *Biomaterials* **28,** 1452–1460 (2007).

139. Monshi, A., Foroughi, M. R. & Monshi, M. R. Modified Scherrer Equation to Estimate More Accurately Nano-Crystallite Size Using XRD. *World J. Nano Sci. Eng.* **02,** 154–160 (2012).

140. Jauncey, G. E. M. The Scattering of X-Rays and Bragg's Law. *Proc. Natl. Acad. Sci.* **10,** 57–60 (1924).

141. Mizushima, K., Jones, P. C., Wiseman, P. J. & Goodenough, J. B. LixCoO2 (0. *Mater. Res. Bull.* **15,** 783–789 (1980).

142. Nitta, N., Wu, F., Lee, J. T. & Yushin, G. Li-ion battery materials: present and future. *Mater. Today* **18,** 252–264 (2015).

143. Wang, G. *et al.* An Aqueous Rechargeable Lithium Battery with Good Cycling Performance. *Angew. Chem.* **119,** 299–301 (2007).

144. Wessells, C., Ruffo, R., Huggins, R. A. & Cui, Y. Investigations of the Electrochemical Stability of Aqueous Electrolytes for Lithium Battery Applications. *Electrochem. Solid-State Lett.* **13,** A59–A61 (2010).

145. Liang, Y. *et al.* Universal quinone electrodes for long cycle life aqueous rechargeable batteries. *Nat. Mater.* **16,** 841–848 (2017).

146. Zhang, S. S., Xu, K. & Jow, T. R. The low temperature performance of Li-ion batteries. *J. Power Sources* **115,** 137–140 (2003).

147. Zhang, S. S., Xu, K. & Jow, T. R. Electrochemical impedance study on the low temperature of Li-ion batteries. *Electrochimica Acta* **49,** 1057–1061 (2004).

148. Zhang, S. S., Xu, K. & Jow, T. R. Low temperature performance of graphite electrode in Li-ion cells. *Electrochimica Acta* **48,** 241–246 (2002).

149. Franks, F. The Properties of Aqueous Solutions at Subzero Temperatures. in *Water and Aqueous Solutions at Subzero Temperatures* 215–338 (Springer, Boston, MA, 1982). doi:10.1007/978-1-4757-6952-4_3

150. Zhang, S. S., Xu, K., Allen, J. L. & Jow, T. R. Effect of propylene carbonate on the low temperature performance of Li-ion cells. *J. Power Sources* **110,** 216–221 (2002).

Appendix A: Permissions for re-use of copyright materials

Figure 2

JOHN WILEY AND SONS LICENSE
TERMS AND CONDITIONS May 18, 2018

This Agreement between Georgia Institute of Technology -- Anirudh Ramanujapuram ("You") and John Wiley and Sons ("John Wiley and Sons") consists of your license details and the terms and conditions provided by John Wiley and Sons and Copyright Clearance Center.

License Number 4352051434903
License date May 18, 2018
Licensed Content Publisher John Wiley and Sons
Licensed Content Publication WILEY INTERDISCIPLINARY REVIEWS: ENERGY AND ENVIRONMENT
Licensed Content Title Review of nanostructured carbon materials for electrochemical capacitor applications: advantages and limitations of activated carbon, carbide-derived carbon, zeolite-templated carbon, carbon aerogels, carbon nanotubes, onion-like carbon, and graphene
Licensed Content Author Wentian Gu, Gleb Yushin
Licensed Content Date Dec 6, 2013
Licensed Content Volume 3
Licensed Content Issue 5
Licensed Content Pages 50
Type of use Dissertation/Thesis
Requestor type University/Academic
Format Print and electronic
Portion Figure/table
Number of figures/tables 1
Original Wiley figure/table number(s) Figure 1(a)
Will you be translating? No
Title of your thesis / dissertation Electrochemical Behavior of Lithium Cobalt Oxide in Aqueous Electrolytes
Expected completion date Aug 2018
Expected size (number of pages) 122
Requestor Location Georgia Institute of Technology
771 Ferst Dr. NW
ATLANTA, GA 30332
United States
Attn: Anirudh Ramanujapuram
Publisher Tax ID EU826007151
Total 0.00 USD

Figure 4

SPRINGER NATURE LICENSE
TERMS AND CONDITIONS May 18, 2018

This Agreement between Georgia Institute of Technology -- Anirudh Ramanujapuram ("You") and Springer Nature ("Springer Nature") consists of your license details and the terms and conditions provided by Springer Nature and Copyright Clearance Center.

License Number 4352060235984
License date May 18, 2018
Licensed Content
Publisher
Springer Nature
Licensed Content
Publication
Nature Chemistry
Licensed Content Title Raising the cycling stability of aqueous lithiumion batteries by eliminating oxygen in the electrolyte
Licensed Content Author JiaYan Luo, WangJun Cui, Ping He, YongYao Xia
Licensed Content Date Aug 8, 2010
Licensed Content Volume 2
Licensed Content Issue 9
Type of Use Thesis/Dissertation
Requestor type academic/university or research institute
Format print and electronic
Portion figures/tables/illustrations
Number of figures/tables/illustrations 1
Highres required no
Will you be translating? no
Circulation/distribution <501
Author of this Springer Nature content no
Title Electrochemical Behavior of Lithium Cobalt Oxide in Aqueous Electrolytes
Instructor name Gleb Yushin
Institution name Georgia Institute of Technology
Expected presentation date Aug 2018
Portions Figure 1 | The intercalation potential of some electrode materials that could possibly be used for aqueous lithium ion batteries
Requestor Location Georgia Institute of Technology
771 Ferst Dr. NW
ATLANTA, GA 30332
United States
Attn: Anirudh Ramanujapuram
Billing Type Invoice
Billing Address Georgia Institute of Technology
771 Ferst Dr. NW
ATLANTA, GA 30332
United States
Attn: Anirudh Ramanujapuram
Total 0.00 USD